Nordic nuclear safety research

NKS-343
ISBN 978-87-7893-425-3

Coolability analyses of heap-shaped debris bed

Eveliina Takasuo
Veikko Taivassalo
Tuomo Kinnunen
Taru Lehtikuusi

VTT Technical Research Centre of Finland

July 2015

Abstract

This report describes the experimental and analytical debris bed coolability studies conducted during 2014 at VTT. The main focus is on the coolability of a heap-shaped debris bed (truncated cone) which has been examined by dryout power measurements with the COOLOCE facility and by two-phase flow simulations. The work is divided to three parts. In the first part, the coolability experiments with the truncated cone, COOLOCE-13 and -13R, are described. The second part presents the testing and validation calculations of the new 2014 version of the MEWA 2D code applied to assess debris coolability. The third part consists of the modelling of the truncated cone experiment by using the new MEWA version and the CFD code Fluent. The experimental results suggest that the heap-like shape of the debris bed is favourable to coolability. The dryout heat flux is comparable to that of the fully conical bed and the other test beds with multi-dimensional flooding. The dryout power predicted by MEWA is within 20% of the experimental results. The effects of the numerical solution options have been examined in the Fluent simulations.

Key words

severe accident, debris bed, coolability, multi-dimensional flooding, numerical simulation, CFD

NKS-343
ISBN 978-87-7893-425-3
Electronic report, July 2015
NKS Secretariat
P.O. Box 49
DK - 4000 Roskilde, Denmark
Phone +45 4677 4041
www.nks.org
e-mail nks@nks.org

Acknowledgements

NKS conveys its gratitude to all organizations and persons who by means of financial support or contributions in kind have made the work presented in this report possible.

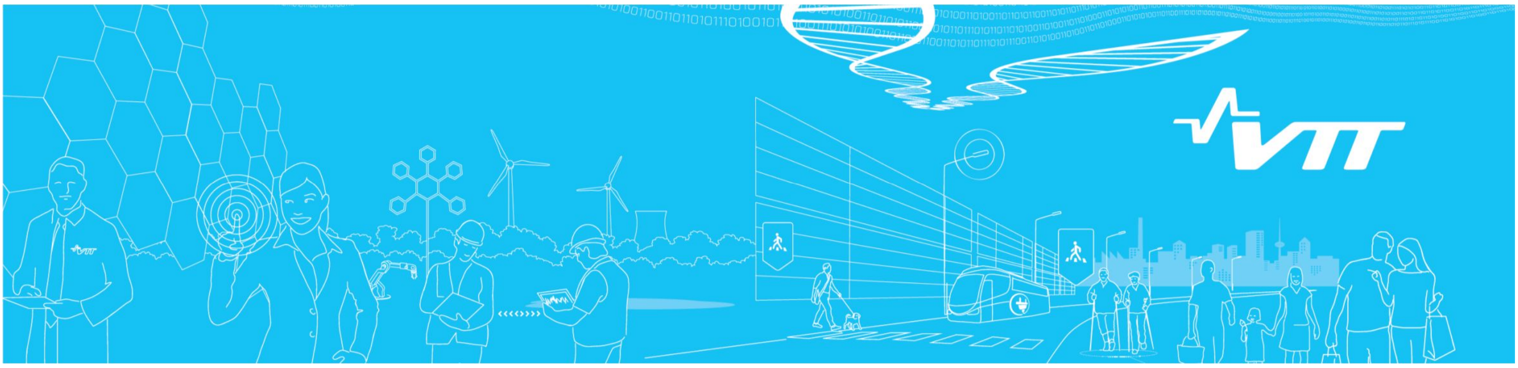

RESEARCH REPORT

VTT-R-00367-15

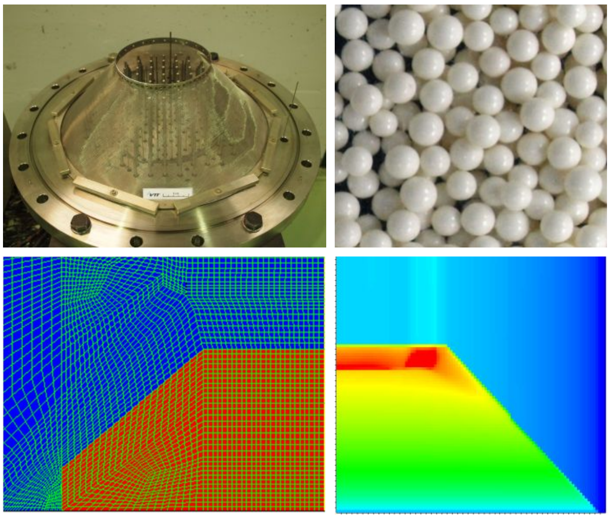

SAFIR2014/COOLOCE-E

Coolability analyses of heap-shaped debris bed

Authors: Eveliina Takasuo, Veikko Taivassalo, Tuomo Kinnunen, Taru Lehtikuusi

Confidentiality: Public

Report's title	
Coolability analyses of heap-shaped debris bed	
Customer, contact person, address	**Order reference**
SAFIR2014 National Research Programme on Nuclear Power Plant Safety	3/2012SAF
Project name	**Project number/Short name**
Core debris coolability and environmental consequence analysis	81658 / COOLOCE-E
Author(s)	**Pages**
Eveliina Takasuo, Veikko Taivassalo, Tuomo Kinnunen, Taru Lehtikuusi	55 p. + 1 appendix
Keywords	**Report identification code**
nuclear energy, severe accidents, COOLOCE experiments, MEWA code, Fluent code, debris bed, two-phase flow, numerical simulation	VTT-R-00367-15

Summary

This report describes the experimental and analytical debris bed coolability studies conducted during the final year of the SAFIR2014 research programme on nuclear power plant safety. The main focus is on the coolability of a heap-shaped debris bed (truncated cone) which has been examined by dryout power measurements with the COOLOCE facility and by two-phase flow simulations.

The work is divided to three parts. In the first part, the coolability experiments with the truncated cone, COOLOCE-13 and -13R, are described. The second part presents the testing and validation calculations of the new 2014 version of the MEWA 2D code applied to assess debris coolability. This includes comparisons to the previous version in use at VTT. The third part consists of the modelling of the truncated cone experiment by using the new MEWA version and the CFD code Fluent.

The experimental results suggest that the heap-like shape of the debris bed is favourable to coolability. The dryout heat flux is comparable to that of the fully conical bed and the other test beds with multi-dimensional flooding. The dryout power predicted by MEWA is within 20% of the experimental results. The effects of the numerical solution options have been examined in the Fluent simulations.

Confidentiality	Public

Espoo 28.1.2015

Written by	Reviewed by	Accepted by
Eveliina Takasuo Senior Scientist	Tuomo Sevón Senior Scientist	Timo Vanttola Head of Research Area

VTT's contact address

PO Box 1000, 02044-VTT, Finland

Distribution (customer and VTT)

SAFIR2014 Reference Group 5
Stuttgart University, IKE: Michael Buck, Georg Pohlner
Royal Institute of Technology (KTH): Pavel Kudinov, Weimin Ma
VTT: Timo Vanttola, Jari Hämäläinen, Vesa Suolanen

Contents

1. Introduction

The coolability of porous debris beds consisting of solidified corium has been investigated in the SAFIR2014 programme on nuclear power plant safety. The studies consist of analytical work by simulation codes and experimental measurements of dryout power in different debris bed geometries (with simulant materials) using the COOLOCE test facility.

In 2014 the dryout power was measured for a test bed with a heap-like shape, i.e. truncated cone, in the COOLOCE-13 and -13R experiments. The experiments were a continuation to a test programme in which already five other debris bed geometries had been investigated [1-6]. All the previous COOLOCE experiments have been modelled using the MEWA 2D severe accident simulation code developed by the IKE institute at Stuttgart University [7-11]. The code is also applied to model the COOLOCE-13 experiment.

The aim of the simulations is to assess the capabilities of the code to predict dryout power for the different debris bed geometries and, specifically, the coolant flooding modes that depend on the geometry. Most of the models applied in the MEWA code are well-known fluid flow and heat transfer models for porous media based on the Ergun's equation [12]. A new version of the MEWA code was taken into use at VTT in March 2014. Prior to the application of the code to the COOLOCE-13 experiment, testing and validation calculations of the new code version were conducted by running the same simulation cases with both the new and old versions.

At VTT porous media models similar to those of MEWA have been adopted for use in connection with 2D or 3D CFD codes [9, 13]. These models are currently implemented into the Ansys Fluent CFD code as user defined functions. The COOLOCE-13 experiment with the truncated cone has been modelled by Fluent with this in-house implementation of the debris bed coolability models.

In this report both MEWA and Fluent simulations of the truncated cone debris bed are presented. The simulation results are compared to each other, and the experimentally measured dryout power is compared to the power predicted by the simulations. In addition, the effects of the solver options such as time step and discretization scheme are examined. This gives an idea of how sensitive the solution is to the numerical models and parameters which can be selected by the code user.

The report is divided in sections as follows: First, the experimental set-up and results of the COOLOCE-13 and -13R experiments are described. Then, the physical models behind the simulation codes are briefly presented, followed by the validation calculations of the MEWA version of 2014 against the older version in use at VTT. The final (and largest) part consists of the simulations of the truncated cone experiment with MEWA and Fluent.

2. COOLOCE-13 and -13R experiments

The experimental set-up and the results of the COOLOCE-13 experiment and the confirmatory experiment COOLOCE-13R are described in this Chapter. The experiment is a continuation to a test programme in which five different debris bed geometries have been examined previously. The COOLOCE test bed geometries are summarized in Figure 1. The details of the experiments can be found in the earlier COOLOCE reports [1-6].

The geometries represent the possible differences in the spatial distributions of the debris particles in the containment (lower drywell) of a Nordic type BWR. In this type of reactor cooling of the debris in a deep water pool in the flooded lower drywell has been adopted as a measure for severe accident management.

The main objectives of the experiments were to (1) compare the coolability of a top-flooded cylindrical debris bed to that of the other geometries and (2) to produce data for simulation code validation. The geometry of the debris bed is important because it determines which type of flooding mode is possible for the infiltration of water into the pores of the bed. The flooding mode may have a crucial role in determining the coolability (heat removal capacity) of the debris bed.

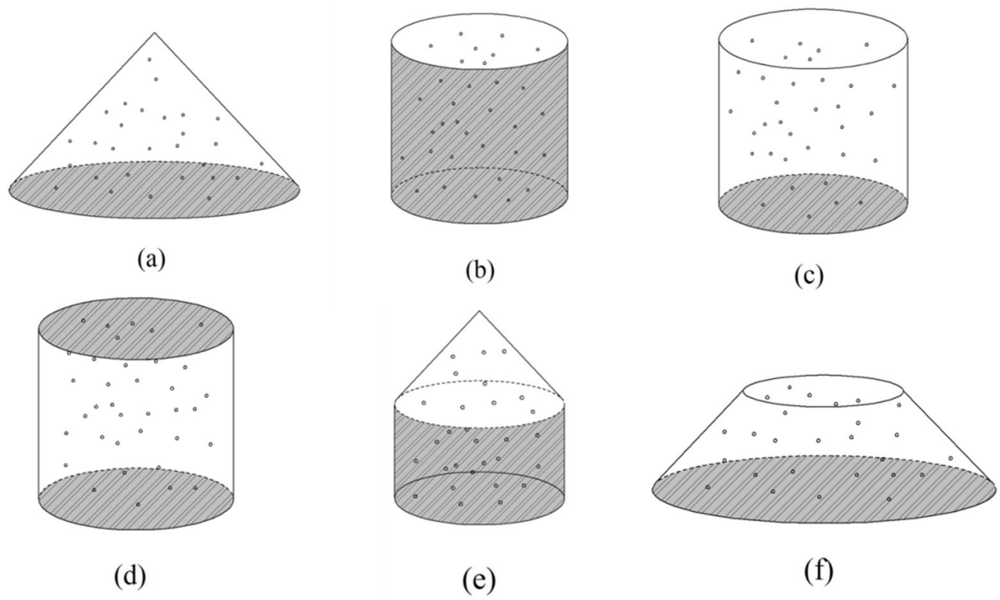

Figure 1. The debris bed geometries for which dryout power has been measured in the COOLOCE experiments: (a) conical, (b) top-flooded cylinder, (c) fully flooded cylinder, (d) cylinder with lateral flooding only, (e) cone on a cylindrical base and (f) truncated cone.

2.1 Experimental set-up

The main components of the COOLOCE test facility are the pressure vessel which houses the test particle bed, the feed water and steam removal systems and instrumentation. The custom-designed pressure vessel has a volume of 270 dm^3 and design pressure of 8 bar. The schematic of the arrangement is presented in Figure 2.

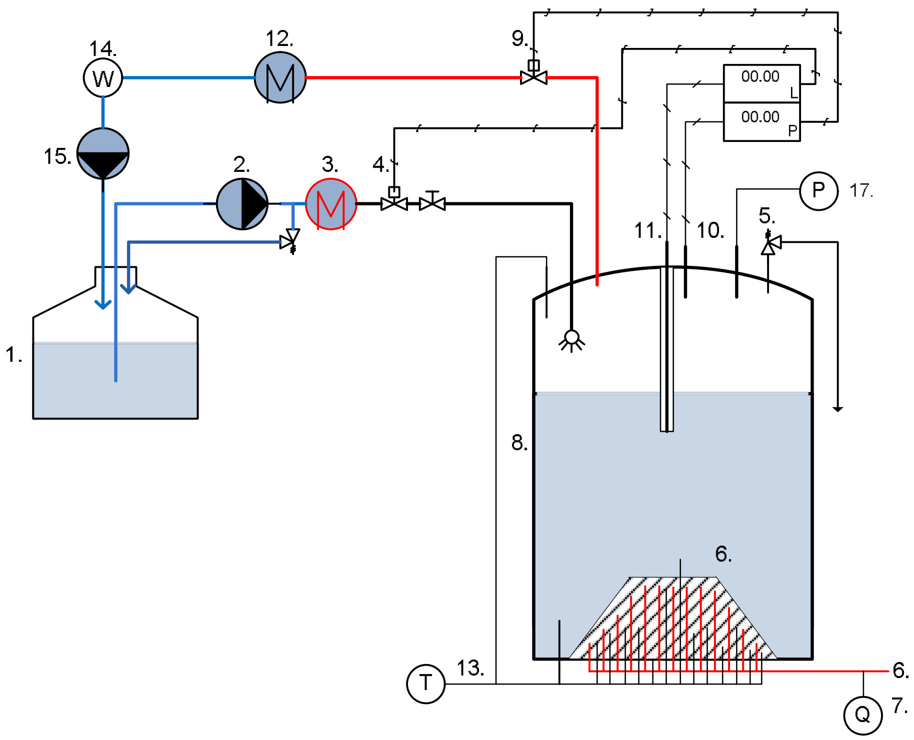

1) Feed water tank
2) Feed water pump
3) Feed water pre-heater
4) Feed water control valve
5) Safety valve
6) Resistance heaters of the test bed
7) Power input and measurement
8) Pressure vessel
9) Steam line control valve (pressure control)
10) Pressure measurement (control)
11) Water level measurement (feed water control)
12) Condenser
13) Test bed temperature measurements
14) Bench scale for condensate mass measurement
15) Water recycling pump
16) Test bed (conical with truncated top)
17) Pressure measurement

Figure 2. Schematic of the COOLOCE facility.

The thirteenth experiment in the COOLOCE programme investigated the dryout power in a truncated cone. This is similar to the conical geometry which was investigated in COOLOCE-1-2 and -6-7 except the cone was truncated at the height of 160 mm to approximate a heap-like geometry. The volume of this test bed is approximately 15.1 dm^3 which is 85% of the fully conical bed with 17.6 dm^3 volume. The height of the original conical geometry is 270 mm, meaning that the height of the truncated cone is 59% of the fully conical geometry. A design sketch of the truncated test bed and the final heating arrangement installed on the bottom plate of the pressure vessel are shown in Figure 3.

The test bed is heated with vertically oriented cartridge heaters based on electrical resistance which, in the flat part of the geometry, are uniform in length (125 mm with 120 mm heated length). The heater diameter is 6.3 mm and the nominal heating power is about 4.5 W/mm. The unheated layer of particles on the top is then 400 mm thick. The thermocouples that are used to detect dryout are arranged in a similar manner as in the conical bed experiment with the exception that the TCs within the radius of the flat part are lowered (because the test bed height is lower).

A long multi-point TC is installed near the centre of the bed (seen in the photograph of Figure 3). This TC has ten sensor points between 0-220 mm. The three topmost sensors monitor the temperature in the pool above the test bed. In addition to the TCs in the bed, five of the heaters are equipped with internal TCs which can be used to monitor the temperature of the sheath of the heater. These TC are axially in the middle of the heater, at about 65 mm from the bottom of the test bed. The heater and thermocouple locations on the bottom plate of the pressure vessel are shown in the maps of Appendix A.

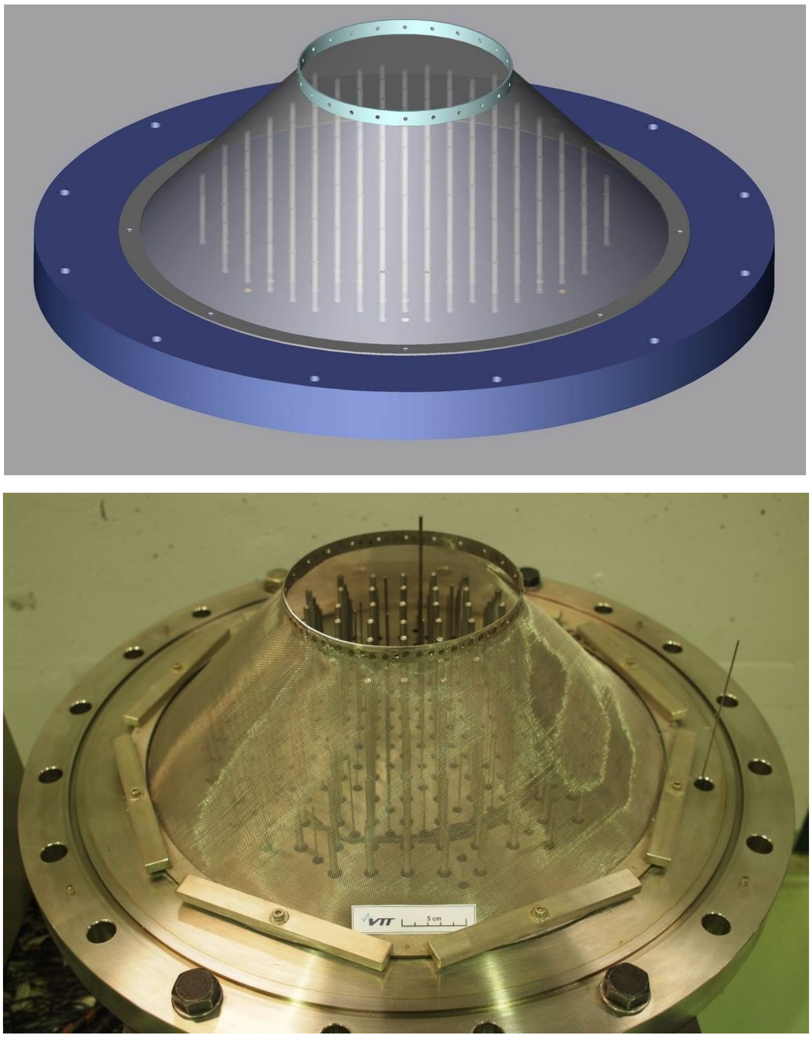

Figure 3. Design sketch of the COOLOCE-13 test bed with heaters (top) and the final heating and thermocouple arrangement (bottom).

The small zirconia/silica beads which have been used in all the geometry comparison experiments were used as the simulant material. The size distribution of the ceramic beads is shown in Figure 4. The surface area weighted average diameter of the particles is 0.95 mm.

The test bed porosity is calculated as the particle volume divided by the volume of the space that can be filled with particles:

$$\varepsilon = 1 - \frac{m_{part} / \rho_{part}}{V_{tot} - V_{heater,TC}}$$

The volume of the heaters and thermocouples (which is 2.8% of the volume of the geometry) is subtracted from the total volume because the presence of these comparatively large structures would reduce the porosity and this would not be hydrodynamically well-grounded (especially when the structures are vertically oriented).

Porosity measured based on the mass of particles and the test bed dimensions, and calculated as above, was 39-40% for the conical and the cylindrical test beds (Figure 1(a)-(d)) and 37.5% for the cone on a base test bed (Figure 1(e)). The same method yielded a porosity of 35.4% for the truncated cone. This value is so low for a random packing of spherical particles that it is likely erroneous e.g. due to the deformation of the wire net. Thus, it is suggested that the “typical” porosity estimated in the previous experiments, 38-40%, is applied in connection with the simulation models.

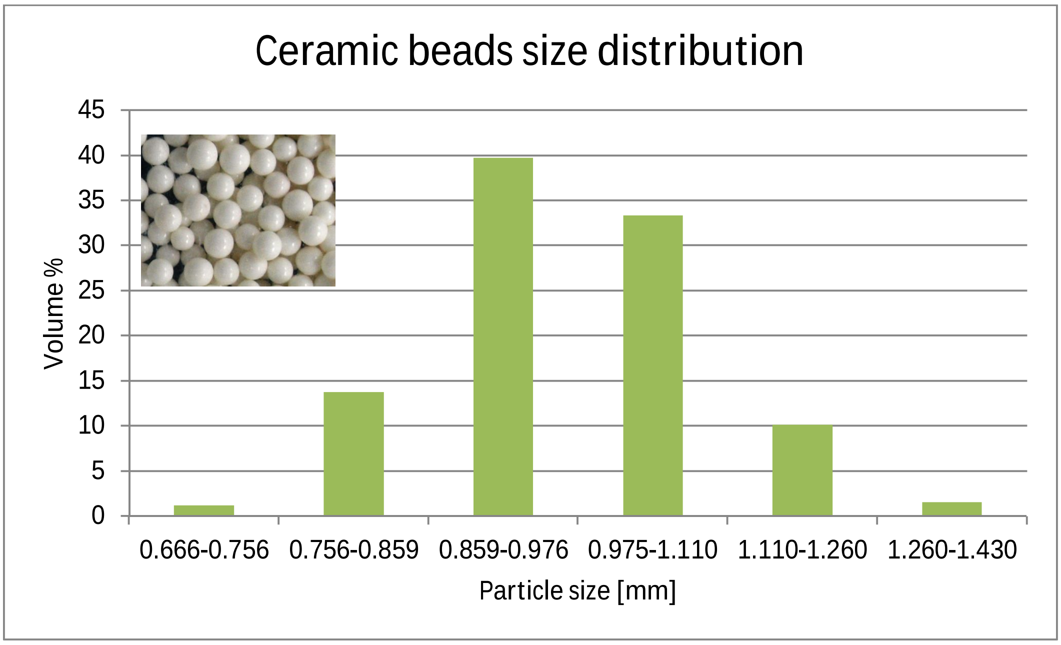

Figure 4. Size distribution of the ceramic beads used in the COOLOCE experiments measured with laser diffraction analysis (sample of the beads shown on top left corner).

2.2 Experimental results of COOLOCE-13

The COOLOCE-13 experiment was started as usual with a warm-up phase during which steady-state boiling was developed. After the warm-up phase, the initial power increases were selected as 5 kW. The idea was – after the observation of dryout – to decrease the power back to the value of the previous coolable state and conduct a more accurate pin-pointing of the dryout power by 1 kW increases until dryout was re-observed. This approach was selected based on the poor predictability of the dryout power before the test (typical to new set-ups) and to avoid the excessive duration of the test which would have resulted if the dryout search would have been conducted altogether with small power steps. The minimum waiting time between the power increases was the “standard” 20 minutes.

The progress of the experiment is illustrated in Figure 5 - Figure 8. Figure 5 shows the power curve and the temperature evolutions of sensors 211-108, 111-315 and T69. In the test bed, dryout was observed only in one sensor, 211-108 at 11 cm from the test bed bottom, whose temperature increased to 150°C immediately after the increase of power to 43.8 kW, at the time of 111 min in Figure 5. The maximum coolable power is the step before this, 40.0 kW. The dryout was followed by a failure of the central heaters which caused the power to fall first to around 39 kW and then to 35 kW. Due to the heater failure, test run was terminated at 126 min. A close-up of the curves in Figure 5 showing the final phase of the experiment (100-135s) is presented Figure 6.

The internal thermocouple in the heater numbered T69 indicated a clear temperature increase already at 25 kW after which the temperature increase followed the power increases: a stepwise increase was seen at the time of power increase, and between the power increases (constant power) a mild, almost linear increase was seen. The maximum temperature of T69 was 355°C, just before the heater failed. In fact, the data from all the heaters equipped with thermocouples showed similar behaviour. This is shown in Figure 7 which shows the temperature evolution of all the heater thermocouples, namely T67-T107.

The drop in the heater temperature back to saturation temperature indicates that the heater in question does not generate power. Thus, it is seen in Figure 7 that only T67 did continue to function until the end of the experiment at 126 min. The other central heaters failed before this due to overheating. The heater failures occurred significantly faster than in the other COOLOCE experiments (several work days vs. two hours) which can be explained by the excessive power load of the heaters in this experiment. Because the heaters are shorter than those in the fully conical or cylindrical beds, the power per heater length (and power per unit of test bed volume) has to be greater.

The process variables which are pressure and water level in the test vessel and the feed water temperature are illustrated in Figure 8. The pressure increased from atmospheric to over 1.4 bar during the test run, meaning that the pressure control was not completely successful. This is because of the increased flow resistance in the steam line with the large steam flow rate which is a result of the large power required for dryout. At the minimum dryout power (43.8 kW) the average pressure was 1.40 bar and at the maximum coolable power (40.0 kW) it was 1.37 bar.

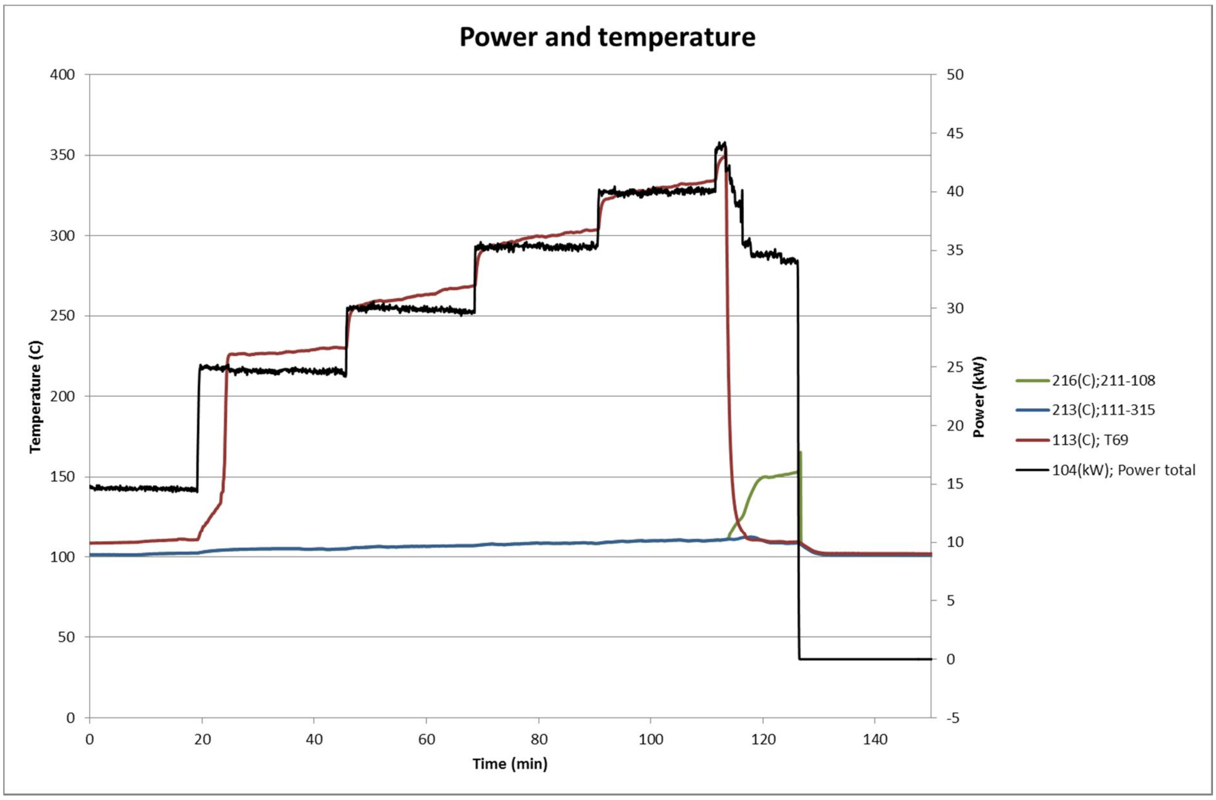

Figure 5. Power and temperature in the COOLOCE-13 experiment.

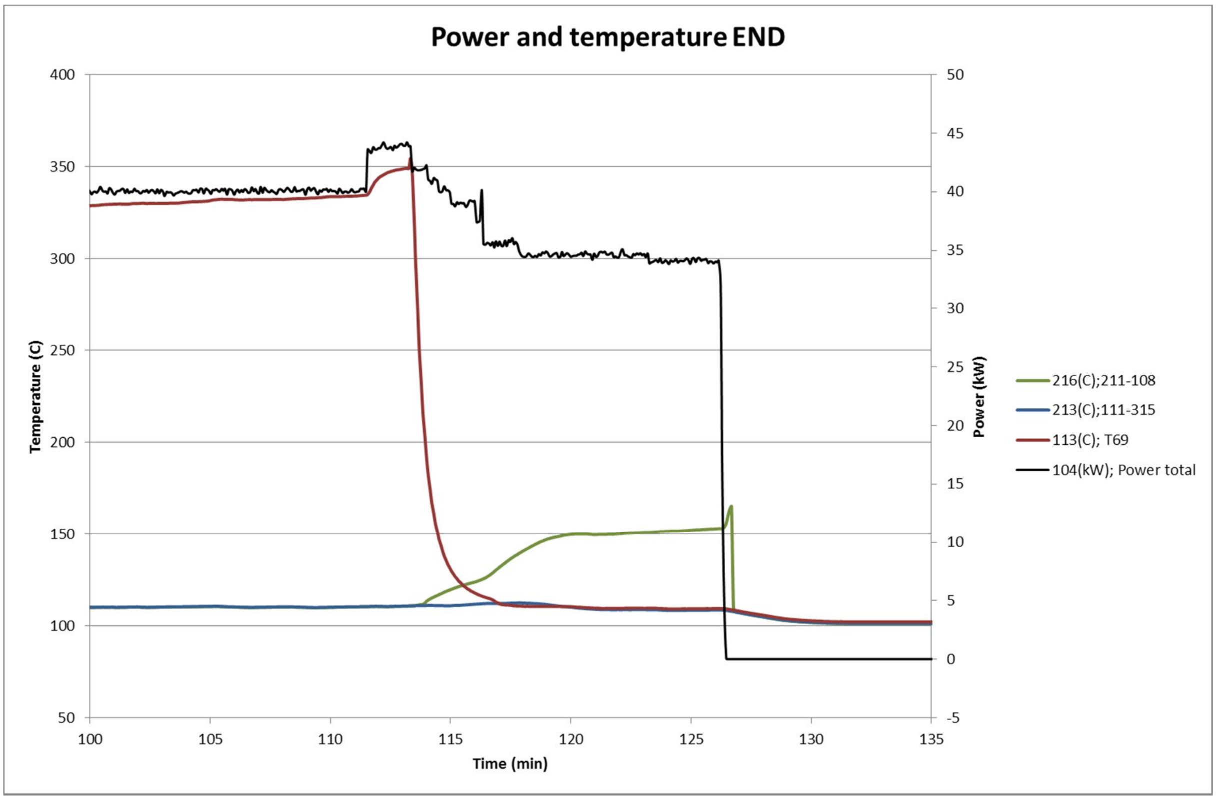

Figure 6. Power and temperature in the COOLOCE-13 experiment (close-up of the dryout phase).

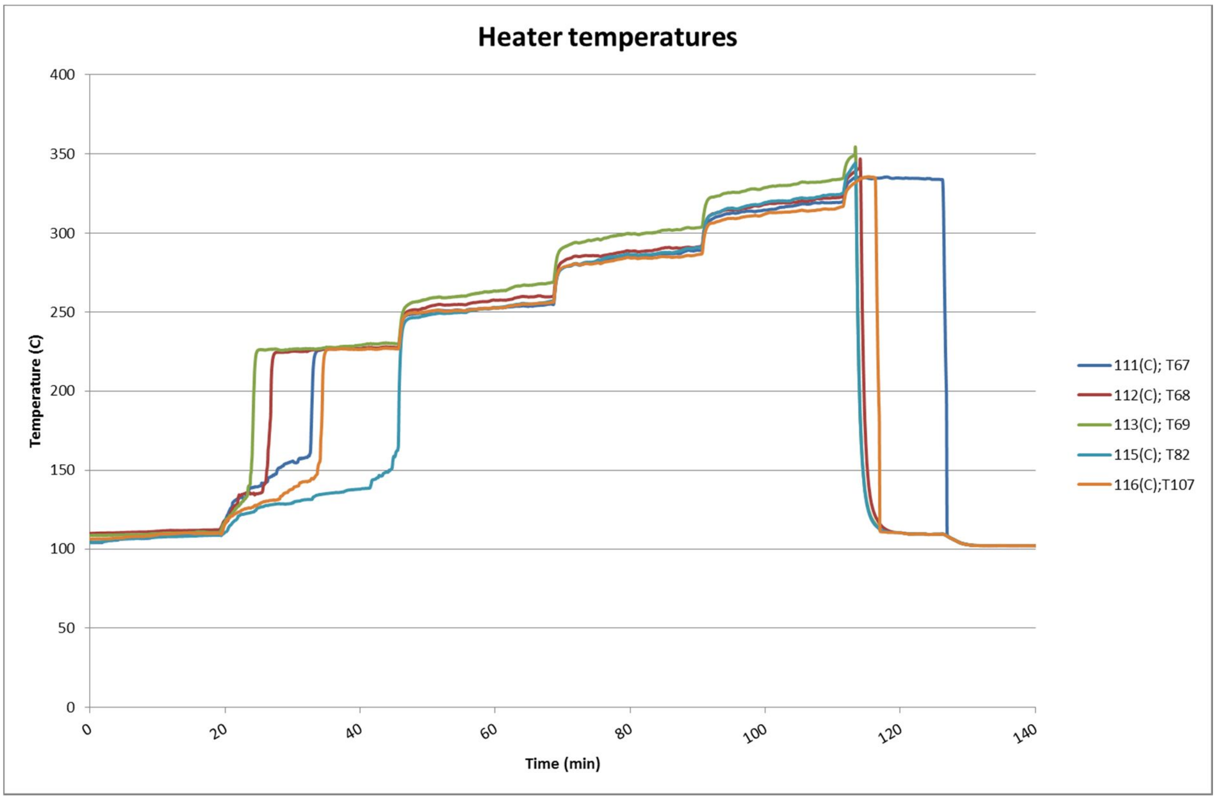

Figure 7. Heater temperatures in the COOLOCE-13 experiments. The height of the sensors is 65 mm.

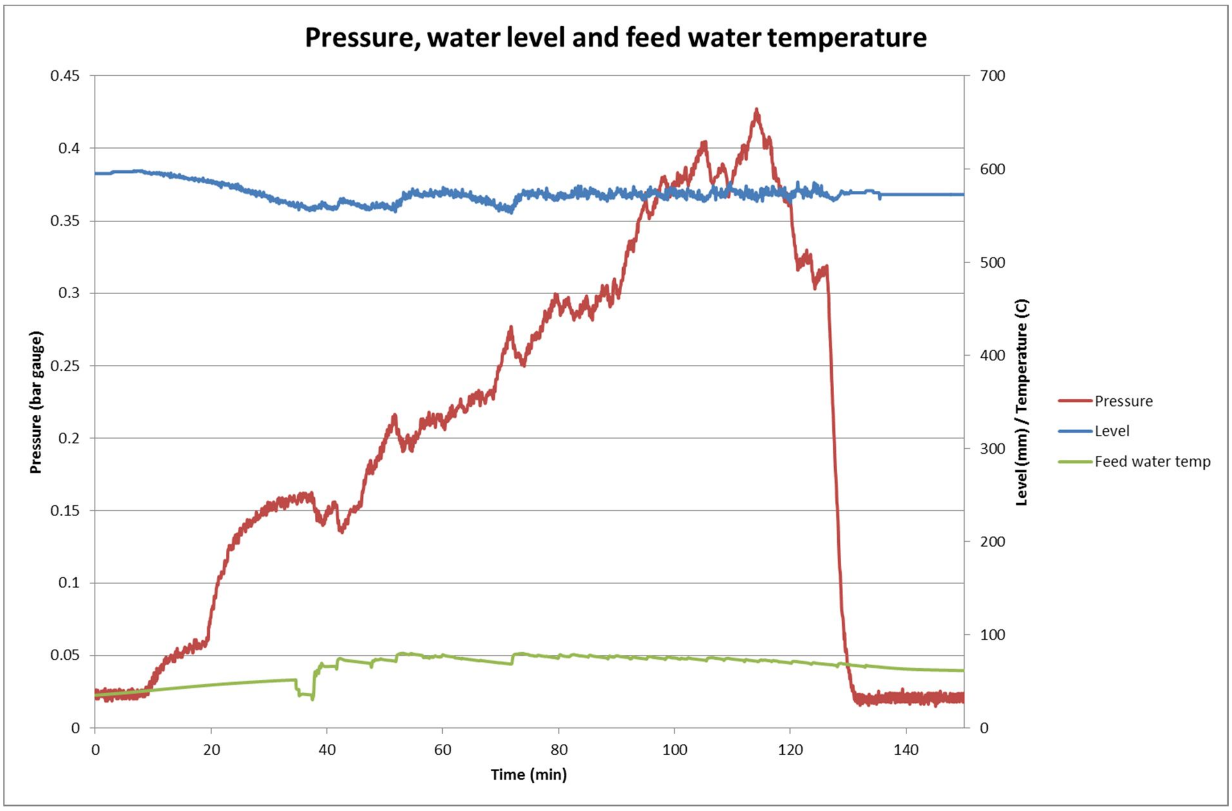

Figure 8. Process variables (pressure, water level and feed water temperature) in the COOLOCE-13 experiment.

2.3 Experimental results of COOLOCE-13R

The COOLOCE-13 experiment was repeated due to the problems encountered with the heaters, pressure control and the relatively poor accuracy of the dryout measurement (4 kW difference between the maximum coolable and minimum dryout power instead of 2 kW). The test procedure was modified by starting the experiment with initially greater power to lessen the time of the heaters exposure to high temperatures and by removing the pressure control valve attached to the steam line. The latter modification prevents the pressurization of the test vessel but lessens the increase of pressure from the atmospheric level by removing the flow resistance caused by the valve. This way a better result for the dryout power was obtained.

The progress of the COOLOCE-13R experiment is illustrated in Figure 9 - Figure 12. The power and temperature evolutions during the experiment are shown in Figure 9. In this figure two occasions of dryout are seen: at 35 and 80 minutes into the experiments. The first dryout was obtained with 5 kW steps after which the power was temporarily shut down, quenching the existing dryout, and the dryout search was repeated with 2 kW steps. This resulted in dryout at **39.2 kW** (average of the power step) with the pressure being 1.25 bar (also average of the power step). The maximum coolable power was **36.9 kW** and the average pressure for which this was measured was 1.22 bar.

The sensors 112-135 and 113-45 located at 12 and 13 cm height from the test bed bottom indicated dryout. These sensors are next to each other near the heater which is located in the centre point of the circular arrangement (see Appendix A). This suggests that the dryout is located almost exactly at the tops of the heaters in vertical direction but below the unheated particle layer. After the incipient dryout, the experiment was continued by conducting two more 1 kW power steps in post-dryout conditions. (Because no future experiments were foreseen with this geometry, it was decided acceptable to risk the heater failure after the incipient dryout had been reliably measured). During these steps (40 kW and 41 kW) the temperature in the test bed increased to the maximum of 185°C but no spreading of the dryout to other sensors was seen.

The waiting time with power exceeding the minimum was not very long but it seems that at least the power of 39.2 kW will result in stabilized conditions in which the temperature is only about 10°C greater than the saturation temperature. A more drastic increase is witnessed with the 41 kW power which does not seem to stabilize. However, some of the central heaters failed at 103 minutes, leaving only 5 minutes of measurement time for this power, and soon after the experiment had to be finished.

In general, the temperatures measured with the heater sensors behaved similarly as in the first test run by increasing stepwise along with the power increases. The heater temperatures are illustrated in Figure 11. In most of the previous experiments the heater temperature behaviour was different and, in many cases, the temperatures remained near saturation until the formation of dryout in test bed sensors. A possible explanation is the large power load in the experiment. The dryout power is comparable to those in the other experiments with pressures above atmospheric but it is produced with shorter heaters. This means that the surface power of the heaters is very high.

The process variables of the COOLOCE-13R are shown in Figure 12. Also in this test run the pressure is somewhat increased from the atmospheric pressure, and the pressure curve coarsely follows the power control (and the resulting steam generation rate). The smaller pressure probably helped to achieve dryout with lower power compared to the first test run.

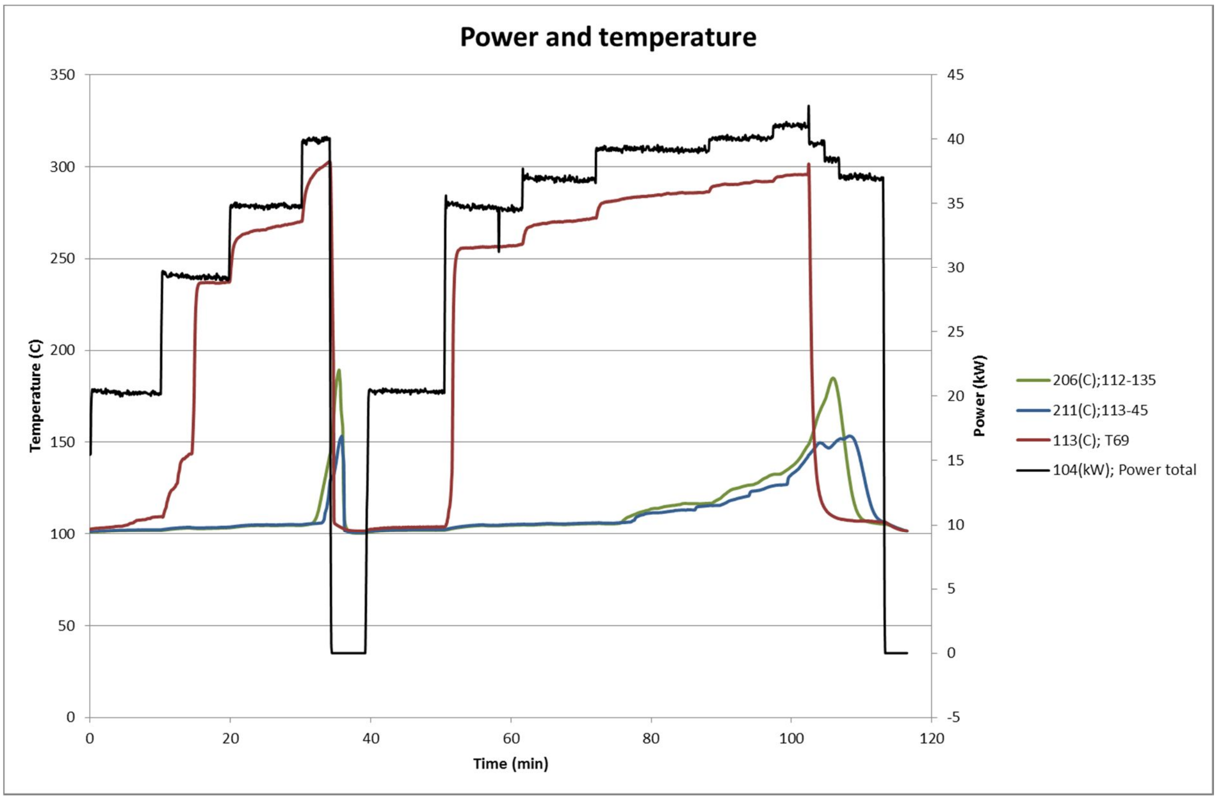

Figure 9. Power and temperature evolutions in the COOLOCE-13R experiment.

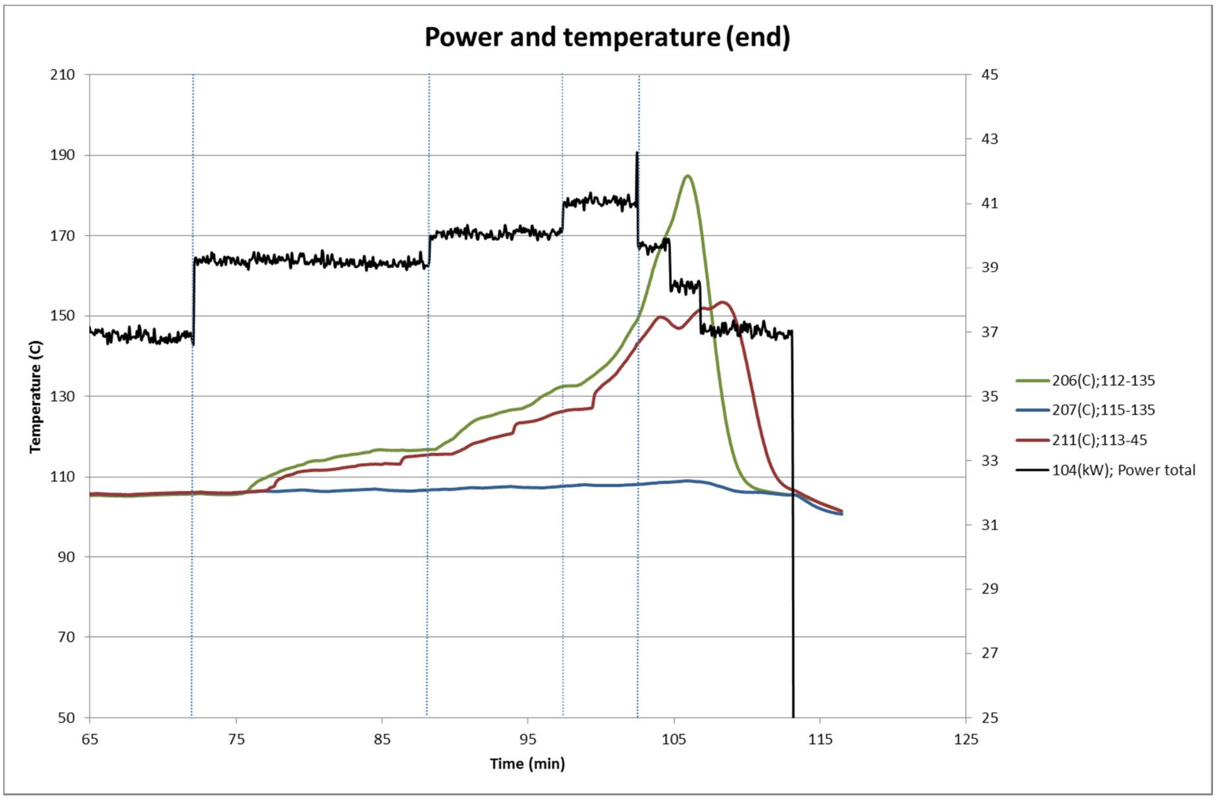

Figure 10. Power and temperature in the COOLOCE-13R experiment (the dryout and post-dryout power steps).

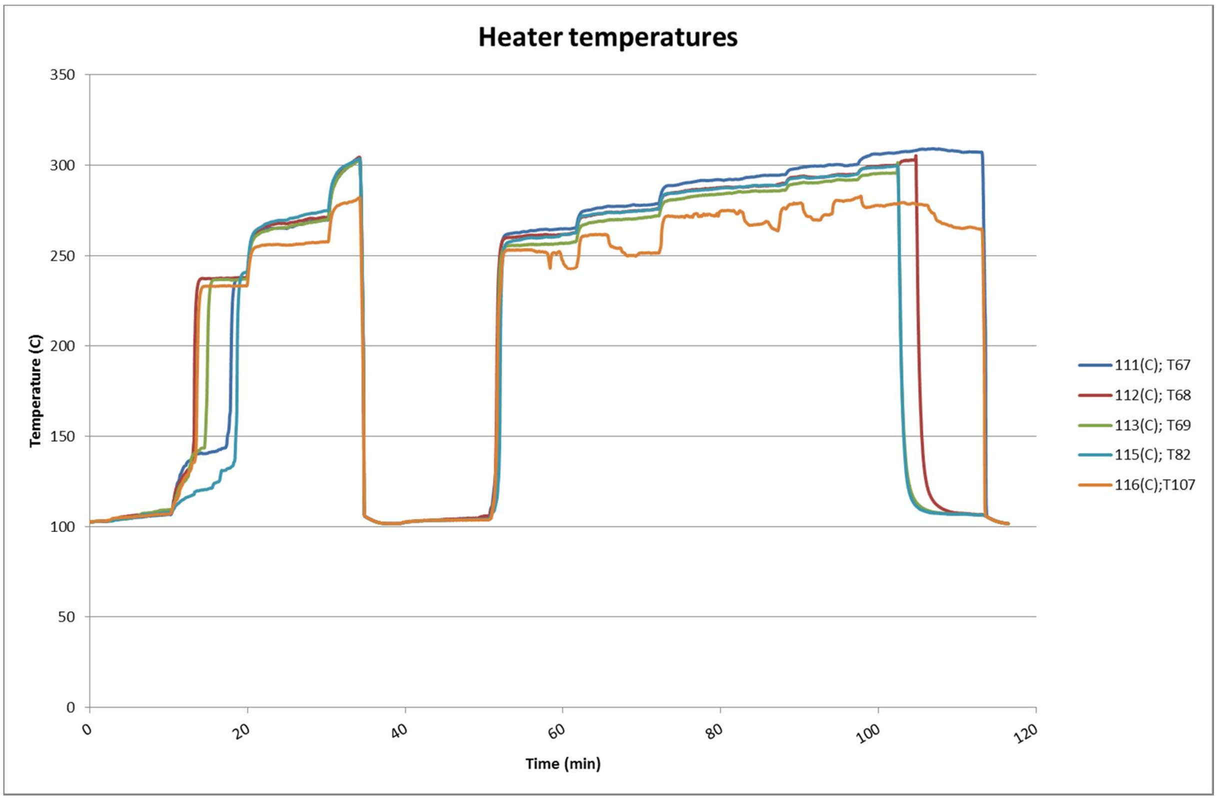

Figure 11. Heater temperatures in the COOLOCE-13R experiment.

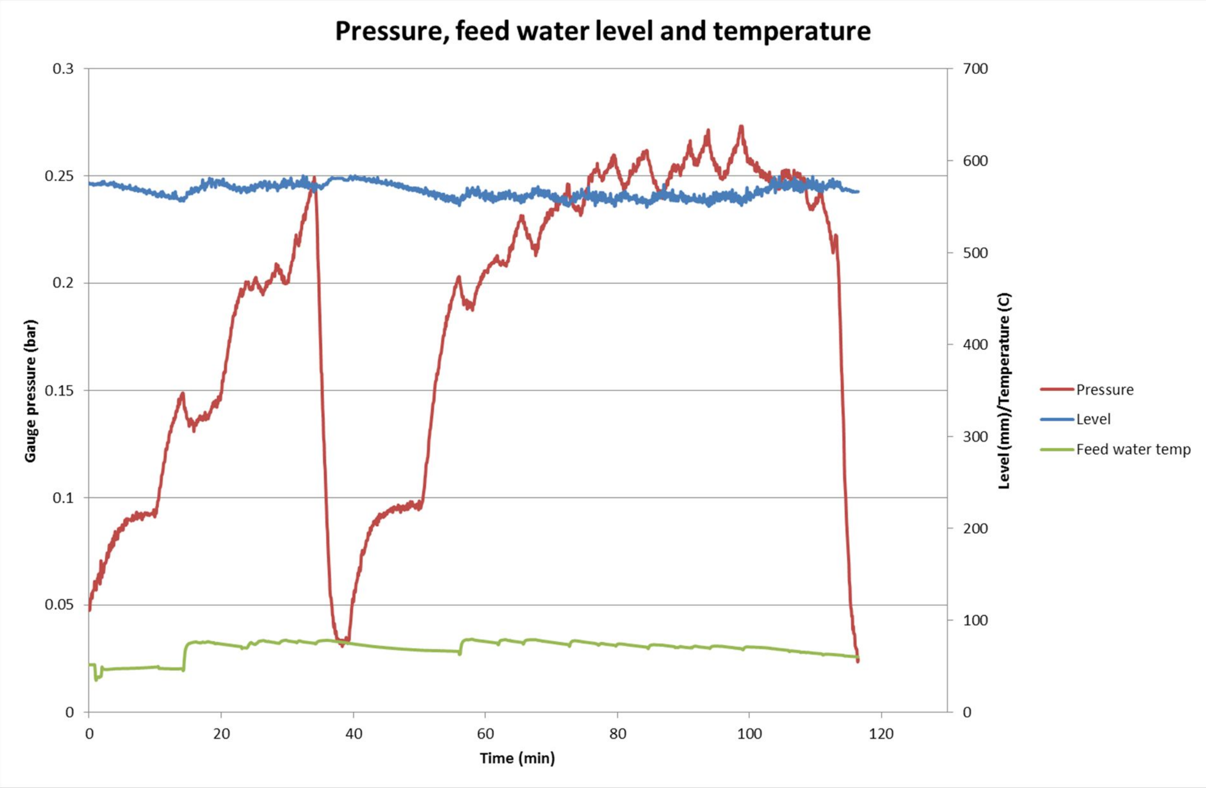

Figure 12. Process variables (pressure, water level and feed water temperature) in the COOLOCE-13R experiment.

2.4 Analysis

The dryout power was measured twice for the truncated cone test bed geometry in the COOLOCE-13 and -13R test runs. There was some difference (11%) in the measured dryout powers of 43.5 kW and 39.2 kW. A part of the difference can be explained by the slightly greater pressure in the first test run. The latter value is considered to be more reliable because the temperature increase was more pronounced and the dryout zone larger (seen by two sensors). Also, the requirement of conservatism does not allow ignoring the measurement in which the dryout power was lower.

The power of 39.2 kW corresponds to the power density of about 2600 kW/m^3. The dryout heat flux at the top boundary is then 416 kW/m^2. This is calculated by multiplying the power density with the height of the bed. Compared to the results of other test bed geometries at 1 bar, the total power and the power density are very large. The fully conical bed showed dryout at about 1470 kW/m^3 at 1.1 bar (total power was 26.0 kW).

The better coolability of the truncated cone is related to the lower height of the geometry: Dryout is reached when the accumulated mass flux (or volume flux) of upwards flowing steam is great enough to replace water. In a homogenously heated debris bed, or in an experimental set-up which approximates homogenous heating, the mass flux increases with increasing height. Then, for the 16 cm truncated cone, the distance “available” for the steam flux increase is less than for the 27 cm conical test bed, and the total power and power density must increase in order to produce dryout.

Note that, here, it is assumed that the other debris bed properties that influence the dryout power are the same in the beds that are compared. Indeed, the heat flux at the test bed top boundary at the dryout power for the truncated cone and the full cone are within 5% of each other: 416 kW/m^2 in COOLOCE-13R and 397 kW/m^2 in COOLOCE-6. This suggests that the coolability difference between the fully conical bed and the truncated cone depends mainly on the debris bed height. A similar assessment has been done for the fully conical bed and the cylindrical bed with top flooding.

In the COOLOCE experiments, dryout power was measured for all six test bed geometries (see Figure 1) at the atmospheric pressure or close to that (1.1-1.3 bar), depending on the accuracy of the pressure control. The dryout heat fluxes at the top boundary of the test beds in these tests are shown in Figure 13. The largest heat fluxes were obtained for the cone on a cylindrical base, the fully flooded cylinder and the fully conical bed, and also for the truncated cone. Common to these geometries is that some form of multi-dimensional infiltration of water is present: water can flood the bed through lateral surfaces to replace steam which exits upwards through the top of the bed.

Lower dryout heat flux is seen for the top-flooded cylinder and the cylinder with lateral flooding only. In the case of top-flooded cylinder, this is explained by the fact that the two phases have to flow in counter-current mode: water can infiltrate only though the top surface against the upwards flowing steam. In the case of the laterally flooded cylinder which has a solid top plate, both water and steam have to infiltrate and exit though the open lateral surface. The top plate forces the steam to escape through the side of the bed, instead of the top surface, which makes the top part below the plate vulnerable to dryout.

Even though these two flooding modes seem in principle different, according to the experimental results the modes are equally efficient (or inefficient) in removing the heat generated by the test bed because the dryout heat fluxes are rather close to each other: 300 kW/m^2 for the laterally flooded cylinder and 270 kW/m^2 for the top-flooded cylinder. Compared to these values, the dryout heat flux measured for the cone is 33-47% greater and, for the fully flooded cylinder, 56-73% greater.

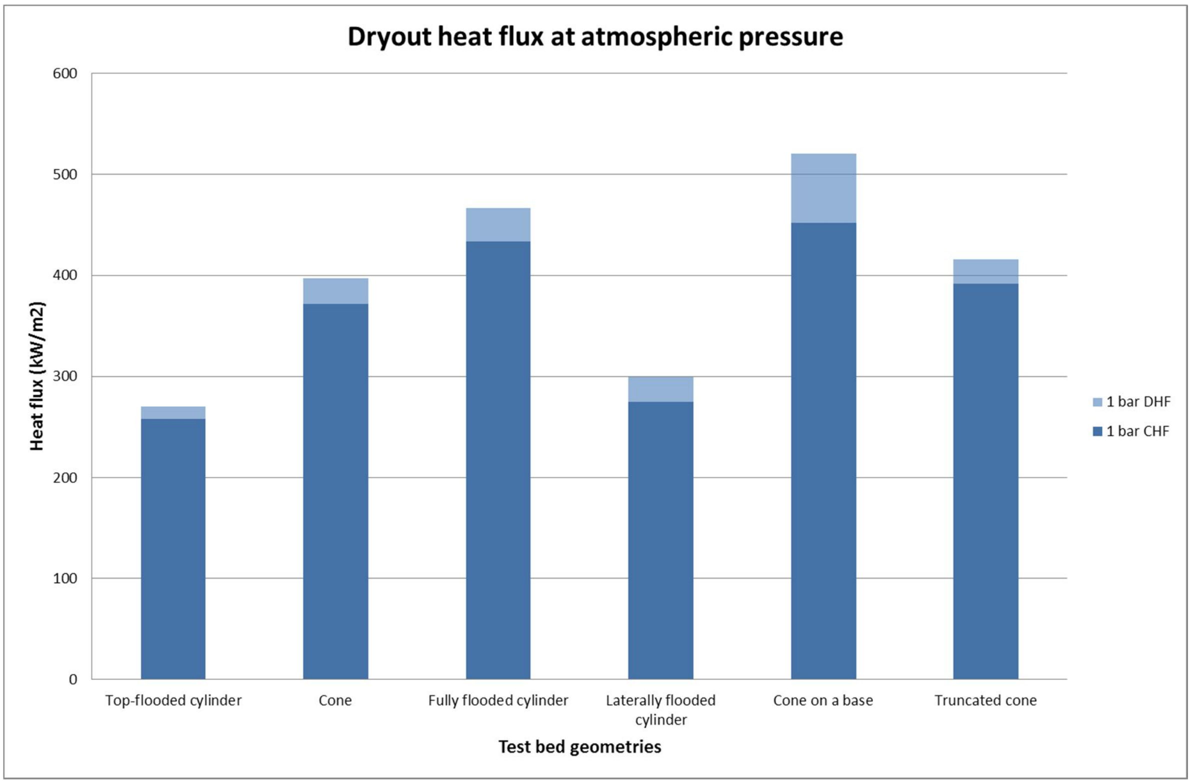

Figure 13. Dryout heat flux at the top boundary of the debris bed in the COOLOCE experiments. The light blue zone is the error margin of the measurement (difference between the maximum coolable heat flux CHF and minimum dryout heat flux DHF).

The dryout location in COOLOCE-13R was in the upper part of the test bed, 11-13 cm from the test bed bottom (3-5 cm from the top surface) and near the centre in radial direction. Note that the heaters reach to the height of 12.5 cm from the bottom, and not all the way to the surface of the test bed at 16 cm. The dryout location in the experiment is illustrated in Figure 14. For comparison, the dryout locations measured in the other COOLOCE geometries are shown in Figure 15. The locations in the illustrations are approximate (heaters and thermocouples are not included) and based directly on the locations of the thermocouples which indicated dryout in the test beds. The details can be found in the earlier COOLOCE reports [1-6].

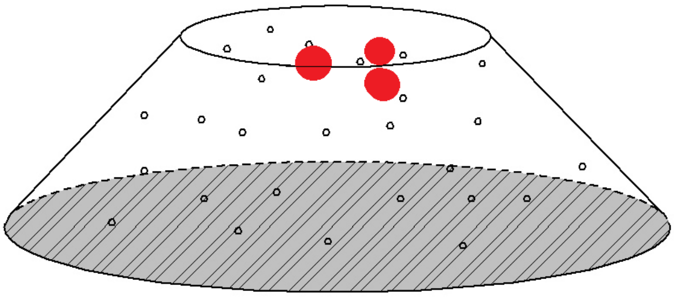

Figure 14. Dryout location for the truncated cone according to the COOLOCE-13 and -13R experiments.

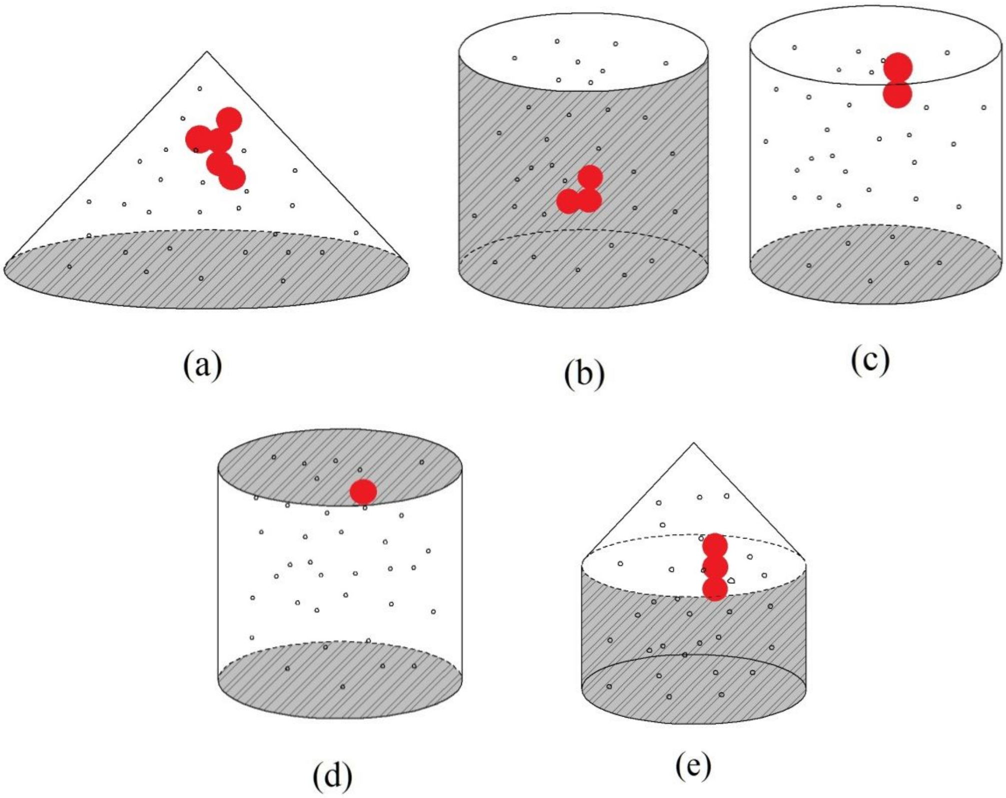

Figure 15. Dryout locations measured in the different COOLOCE experiments: (a) conical test bed, (b) cylindrical test bed with top flooding, (c) fully flooded test bed, (d) cylinder with lateral flooding only and (e) cone on a cylindrical base.

2.5 Summary of the experiment

In the COOLOCE-13 experiment dryout power was measured for a heap-like debris bed (truncated cone). The total power required for dryout was high compared to the other test beds but this is explained by the height (or depth) of the test bed which was lower in this experiment than in the previous experiments. Comparison of the heat fluxes at the top boundary in the different test beds reveals that the coolability, even when "corrected" with the effect of the height, is comparatively high, about the same than that of the fully conical bed and the fully flooded cylinder with open sidewall.

3. Simulation models

The debris bed coolability simulations are performed using MEWA and Fluent. MEWA is a 2D two-phase solver developed specifically for debris coolability and severe accident analyses by the IKE Institute at Stuttgart University [7, 8]. Fluent is a widely used commercial CFD software package by Ansys Inc [14,15]. Next, the modelling principles and the physical models applied in these codes are concisely presented.

3.1 Conservation equations

The multi-dimensional modelling of the debris bed dryout behaviour is based on solving the two-phase flow conservation equations, namely, the mass, momentum and energy conservation for the gas and liquid phases. The closure models for the frictional forces and heat transfer are well-known models found in the literature. The general form of the conservation equations is given below. The mass conservation is

$$\frac{\partial}{\partial t}(\varepsilon\alpha_i\rho_i) + \nabla\cdot(\varepsilon\alpha_i\rho_i\vec{v}_i) = \Gamma \qquad (1)$$

where ε is porosity (-), α_i is the volume fraction of the phase i ($i=g$, $i=l$), ρ_i is the phase density (kg/m^3), $\vec{v}_i$ is phase velocity (m/s) and Γ is the source term due to evaporation (kg/m^3/s). The momentum equation is

$$\frac{\partial}{\partial t}(\varepsilon\alpha_i\rho_i\vec{v}_i) + \nabla\cdot(\varepsilon\alpha_i\rho_i\vec{v}_i\vec{v}_i) = -\varepsilon\alpha_i\nabla p_i + \varepsilon\alpha_i\rho_i\vec{g} + \nabla\cdot(\varepsilon\alpha_i\vec{\tau_i}) + \vec{F}_{s,i} + \vec{F}_i \qquad (2)$$

where p_i is pressure (Pa), $\vec{\tau_i}$ is the viscous stress tensor (N/m^2), $\vec{F}_{s,i}$ is the drag force between the solid particles and the fluid phase i (N/m^3) and $\vec{F}_i$ is the interfacial drag (gas-liquid drag) on the phase i (N/m^3). The energy conservation equation for the fluid phases is

$$\frac{\partial}{\partial t}(\varepsilon\alpha_i\rho_i h_i) + \nabla\cdot(\varepsilon\alpha_i\rho_i\vec{v}_i h_i) = \nabla\cdot\left(\lambda_{eff,i}\nabla T_i\right) + Q_{s,i} + Q_{evap,i} \qquad (3)$$

where h_i is the specific enthalpy of phase i (J/kg) , T_i is the phase temperature (K), $Q_{s,i}$ is the heat flux from the solid phase to the fluid (W/m^3) and $Q_{evap,i}$ is the heat flux by evaporation (W/m^3). The effective thermal conductivity $\lambda_{eff,i}$ (W/m/K) is calculated from the phase thermal conductivity, $\lambda_{eff,i} = \lambda_i \varepsilon \alpha_i$. In addition, energy conservation is solved for the solid phase:

$$\frac{\partial}{\partial t}((1-\varepsilon)\rho_s h_s) = \nabla \cdot (\lambda_{eff,s} \nabla T_s) + Q_{s,decay} - Q_{s,sat} - Q_{s,g} - Q_{s,l} \tag{4}$$

where $Q_{s,decay}$ is the internal heat source of the material (decay heat or test facility heaters), $Q_{s,sat}$, is the heat flux directed to evaporation and $Q_{s,g}$ and $Q_{s,l}$ are the heat fluxes from the solid particles directly to the fluid phases ($Q_{s,l}$ is important mainly in dryout conditions and $Q_{s,l}$ if the liquid phase is subcooled). For the effective thermal conductivity of the porous medium $\lambda_{eff,s}$, a separate model that accounts for convection and radiation is applied [16,17].

3.2 Drag force models

In the MEWA 2D code, a simplified form of the momentum equations is used in which viscous stress term is not taken into account. For the drag forces between the solid and the fluid phases $\vec{F}_{s,i}$ in Eq. (2), let us write $\vec{F}_{s,l}$ for the liquid-solid drag and and $\vec{F}_{s,g}$ for the liquid-gas drag, and $\alpha = \alpha_g$ for the void fraction. The drag forces are expressed as functions of superficial phase velocity $\vec{j_i}$ by using the concepts of permeability *K* and passability *η*, and relative permeability $K_r$and relative passability η_r:

$$\overrightarrow{F_{s,l}} = \varepsilon(1-\alpha)\left(\frac{\mu_L}{KK_{rl}}\vec{j_l} + \frac{\rho_L}{\eta\eta_{rl}}|\vec{j_l}|\vec{j_l}\right) \tag{5}$$

$$\overrightarrow{F_{s,g}} = \varepsilon\alpha\left(\frac{\mu_g}{KK_{rg}}\overrightarrow{j_g} + \frac{\rho_g}{\eta\eta_{rg}}|\overrightarrow{j_g}|\overrightarrow{j_g}\right) \tag{6}$$

The relation between the physical and superficial velocities is

$$\vec{j_l} = \varepsilon(1-\alpha)\vec{v}_l \tag{7}$$

$$\overrightarrow{j_g} = \varepsilon\alpha\vec{v}_g \tag{8}$$

Permeability and passability describe the capability of porous medium to transmit fluid. They are expressed according to Ergun [12] as

$$K = \frac{\varepsilon^3 d^2}{150(1-\varepsilon)^2} \tag{9}$$

$$\eta = \frac{\varepsilon^3 d}{1.75(1-\varepsilon)} \tag{10}$$

The presence of the other fluid phase in the two-phase flow is taken account by using relative permeability K_r (-) and relative passability η_r (-) which are functions of the void fraction

$$K_{rl} = (1-\alpha)^n, K_{rg} = \alpha^n \tag{11}$$

$$\eta_{rl} = (1-\alpha)^m, \eta_{rg} = \alpha^m \tag{12}$$

The powers of relative permeability and passability depend on the author (and the respective experiments). For the relative permeability, *n = 3* is typically used. For the relative passability, Lipinski [18] suggested *m = 3*. Reed [19] suggested *m=5* which yields a somewhat increased friction and was later used also by Lipinski [20]. Later, Hu and Theofanous [21] proposed *m=6*. These three models that differ from each other only in the relative passability are the "classical" models used to predict the formation of dryout with no consideration of the gas-liquid drag. As the empirical models aim to describe the total pressure loss, the gas-liquid drag is implicitly included in the models.

In the models that account for the interfacial drag term $\vec{F_i}$, there are two alternative approaches. Schulenberg & Müller [22] proposed an empirical correlation for the interfacial drag based on pressure measurements. Tung and Dhir [23] developed a more detailed model in which the drag coefficients are calculated according to flow regimes which were determined based on visual observations. The Tung and Dhir model was later modified by Schmidt [24] and Rahman [8] to increase the capability of the model to predict dryout heat flux in both top and bottom flooding conditions. The detailed description of the models with interfacial drag (as well as the other models applied in MEWA) can be found in Rahman [8].

3.3 Heat transfer models

Initially and in pre-dryout conditions in the simulations, the solid particles, liquid and gas are practically in thermal equilibrium at saturation temperature. Heat is transferred from the debris mainly by phase change of water to steam. The heat transfer from the solid particles to steam becomes important in near-dryout conditions and especially after dryout has been reached and the temperature of the solid starts to increase. The boiling rate is calculated by dividing the heat flux from the solid with the latent heat of evaporation:

$$\Gamma = \frac{Q_{s,sat}}{\Delta H_{evap}} \tag{13}$$

To calculate the boiling heat transfer coefficient, the Rohsenow correlation [25] is applied for nucleate pool boiling regime and the Lienhard correlation [26] for the film boiling regime (with transition zone calculated by an interpolation function). Heat transfer from solid to steam is assumed to occur when the solid temperature is above saturation temperature and the gas fraction is 0.7 or greater. The heat flux from solid to gas is

$$Q_{s,g} = a_{s,g} h_{s,g} (T_s - T_g) \tag{14}$$

The interfacial area density is obtained from porosity and the particle diameter D_p:

$$a_{s,g} = \frac{6 \cdot (1 - \varepsilon)}{D_p} F(\alpha) \tag{15}$$

$$F(\alpha) = \begin{cases} 0 & \text{if} \quad \alpha < 0.7 \\ \dfrac{\alpha - 0.7}{0.3} & \text{if} \quad \alpha \geq 0.7 \end{cases} \tag{16}$$

The heat transfer coefficient from solid to steam is

$$h_{s,g} = \frac{Nu_{s,g} \lambda_g}{D_p} \tag{17}$$

The Nusselt number is calculated according to the Ranz-Marshall correlation [27]:

$$Nu_{s,g} = 2 + 0.6 \sqrt{Re_g} \cdot \sqrt[3]{Pr_g} \tag{18}$$

where the Reynolds number is

$$Re_g = \frac{|\vec{v}_g \rho_g D_p|}{\eta_g} \tag{19}$$

In MEWA, this correlation is applied in the form that omits the Prandtl number term, shortening the correlation to

$$Nu_{s,g} = 2 + 0.6\sqrt{Re_g} \tag{20}$$

The MEWA documentation does not give explanation to the omission but, apparently, it is because the cubic root of the Prandtl number is very close to 1.0 due to the low thermal conductivity of the steam phase.

3.4 Physical models and implementation in FLUENT

There are two commonly applied CFD formulations to describe fluid flows in a porous medium, the physical (pore, interstitial) velocity formulation and the superficial velocity formulation. Both approaches are available in Fluent [14]. The conservation equations based on the physical velocity formulation are computationally more difficult to solve, if the porosity varies significantly or the medium is hydrodynamically anisotropic.

3.4.1 Physical velocity formulation

In the physical velocity formulation, the velocity in the balance equations is representing the actual velocity in the pores of the porous medium. Since in the porous medium approximation all quantities are representing average values over a representative elementary volume, the physical velocity is thus an average of the velocity in pores.

In multiphase CFD codes, the physical velocity based balance equations for porous media are similar to Eqs. (1) – (3) [14]. Computationally obtained results are reliable as long as the porous medium is homogenous and the flow is largely controlled by the friction forces. Applicability of Eqs. (1) – (3) is not obvious, when the porosity varies. In principle, specific interface models are needed for porosity steps. In practical applications, the influences of the porosity steps are, however, usually ignored. Furthermore, conservation equations similar to Eqs. (1) – (3) can and are used for free-flow zones (ε = 1). In these applications, several terms are ignored in the derivation (i.e. the pressure fluctuation term) and some of them might be important.

One term missing in the momentum equation (Eq.(2)) is the momentum exchange between the phases due to the mass exchange term Γ in the continuity equation, Eq. (1). This term was implemented in the CFD simulations as follows

$$\overrightarrow{F_{\Gamma,g}} = -\overrightarrow{F_{\Gamma,l}} = \max(\Gamma, 0)\,\vec{v}_l - \max(-\Gamma, 0)\,\vec{v}_g \tag{21}$$

The momentum exchange resulting from the mass exchange is small in particle beds. The term might have some importance in the free-flow pool outside the bed. The MEWA formulation for the momentum equation ignores the shear stress term $\nabla \cdot (\varepsilon \alpha_i \vec{\tau_i})$. For isotropic and incompressible Newtonian fluids (i.e. for most common fluids), the shear stress can be calculated from

$$\vec{\tau_i} = \mu_i\left(\nabla \vec{v}_i + (\nabla \vec{v}_i)^{\mathrm{T}}\right) \tag{22}$$

In CFD tools, the frictional force $\overrightarrow{F_{s,\iota}}$ (Eq. (2)) is commonly expressed as follows [14]

$$\overrightarrow{F_{s,\iota}} = -\varepsilon^2 \alpha_i \mu_i D_i \overrightarrow{v_\iota} - \frac{1}{2}\varepsilon^3 \alpha_i \rho_i C_{2,i} |\overrightarrow{v_\iota}| \overrightarrow{v_\iota} \tag{23}$$

In the Fluent code, the coefficients D_i and $C_{2,i}$ are determined to obtain the same frictional forces $\overrightarrow{F_{s,l}}$ and $\overrightarrow{F_{s,g}}$ as in the MEWA code (Eqs. (5) and (6)). For all zones modelled as porous regions, the same models for the interfacial drag term $\vec{F_i}$ were used as in the MEWA simulations. For open free-flow zones, the model of Schiller and Naumann [28] was employed in order to obtain a correct slip velocity.

Considering heat transfer, coding of the source terms in Eqs. (3) and (4) and the effective thermal conductivities in the MEWA code was analyzed and followed closely in the Fluent implementation. The solid temperature is calculated utilizing a user-defined scalar transport equation to solve the balance equation Eqs. (4).

3.4.2 Superficial velocity formulation

In the superficial velocity formulation of the conservation equations, the velocity *v* in the conservation equations is replaced by the superficial (Darcy) velocity *j* defined as

$$j = \frac{Q}{A} \tag{24}$$

where *Q* is volume flow rate through the surface with the area *A*. Solving of the balance equations is easier as the superficial velocity does not change with the porosity. On the other hand, the acceleration and deceleration of the fluid at porosity steps and the corresponding pressure decreases and increases are ignored. As numerically significantly more stable, most of the porous media simulations are performed based on the superficial velocity approach. In a highly resistive porous medium, the convection and viscous terms (no turbulence) could be ignored and the momentum equation simplifies further and the pressure could be computed directly from a potential-flow formulation.

For multiphase flows, Fluent applies somewhat differently defined superficial velocity

$$j_{i,Fl} = \frac{Q_i}{\alpha_i A} \tag{25}$$

The conservation equations can thus be written as follows

$$\frac{\partial}{\partial t}(\alpha_i \rho_i) + \nabla \cdot \left(\alpha_i \rho_i \vec{j}_{i,Fl}\right) = \Gamma \tag{26}$$

$$\frac{\partial}{\partial t}\left(\alpha_i \rho_i \vec{j}_{i,Fl}\right) + \nabla \cdot \left(\alpha_i \rho_i \vec{j}_{i,Fl} \vec{j}_{i,Fl}\right) = -\alpha_i \nabla p_i + \alpha_i \rho_i \vec{g} + \nabla \cdot (\alpha_i \vec{\tau_\iota}) + \frac{\vec{F}_{s,i}}{\varepsilon} + \frac{\vec{F_i}}{\varepsilon} + \frac{\overrightarrow{F_{\Gamma,\iota}}}{\varepsilon} \tag{27}$$

$$\frac{\partial}{\partial t}(\alpha_i \rho_i h_i) + \nabla \cdot \left(\alpha_i \rho_i \vec{j}_{i,Fl} h_i\right) = \nabla \cdot \left(\lambda_{eff,i} \nabla T_i\right) + Q_{s,i} + Q_{evap,i} \tag{28}$$

The friction force terms are thus

$$\frac{\vec{F}_{s,i}}{\varepsilon} = -\alpha_i \mu_i D_i \overrightarrow{J_{i,Fl}} - \frac{1}{2}\alpha_i \rho_i C_{2,i} \left|\overrightarrow{J_{i,Fl}}\right| \overrightarrow{J_{i,Fl}} \tag{29}$$

The coefficients D_i and $C_{2,i}$ are determined as in the physical velocity formulation. The pore velocity is used when calculating the interfacial drag force. The heat transfer models are the same as in the physical velocity formulation.

3.4.3 Turbulence modelling

Eqs. (1.) – (3) and (26) – (28) are commonly applied to turbulent multiphase flows in porous media and free-flow zones by adding an extra shear term $\nabla \cdot \left(\varepsilon \alpha_i \overline{\overline{\tau_{T,i}}}\right)$ in the momentum equations. The calculation of the turbulent stress $\overline{\overline{\tau_{T,i}}}$ is commonly based on turbulence models. In Fluent

$$\overline{\overline{\tau_{T,i}}} = \mu_{T,i}\left(\nabla \vec{v}_i + (\nabla \vec{v}_i)^{T}\right) - \frac{2}{3}\left(\rho_i k_i + \mu_{T,i} \nabla \cdot \vec{v}_i\right)\mathbf{I} \tag{30}$$

where $\mu_{T,i,}$ is the turbulent viscosity, k_i the turbulent kinetic energy and $\mathbf{I}$ the identity tensor. The turbulent viscosity $\mu_{T,i,}$ and turbulent kinetic energy k_i are provided by the turbulence model.

In this study the *k*-ε mixture turbulence model was used. For porous media, the turbulence model would need some modifications but, for instance, the Fluent models do not have any corrections for porous media application. On the other hand, in highly resistive porous media like beds with small particles and under weak forces, flow is largely laminar. Therefore, in this study flows in the porous zones were assumed laminar and turbulence was modelled only in free-flow zones, i.e. in the water pool outside the bed.

In the *k*-ε mixture turbulence model, the turbulence kinetic energy and turbulence dissipation rate are solved for the mixture of the phases.

$$\frac{\partial(\rho_m k)}{\partial t} + \nabla \cdot (\rho_m \vec{v}_m k) = \nabla \cdot \left[\frac{\mu_{T,m}}{\sigma_k} \nabla k\right] + G_k - \rho_m \epsilon \tag{31}$$

$$\frac{\partial(\rho_m \epsilon)}{\partial t} + \nabla \cdot (\rho_m \vec{v}_m \epsilon) = \nabla \cdot \left[\frac{\mu_{T,m}}{\sigma_\epsilon} \nabla \epsilon\right] + \frac{\epsilon}{k}(C_{1\epsilon} G_k - C_{2\epsilon} \rho_m \epsilon) \tag{32}$$

where ϵ is the turbulent dissipation rate, C_1 and C_2 are model constants and ρ_m and $\vec{v}_m$ the mixture density and velocity. In our case

$$\rho_m = \alpha_l \rho_l + \alpha_g \rho_g \tag{33}$$

$$\vec{v}_m = \frac{\alpha_l \rho_l \vec{v}_l + \alpha_g \rho_g \vec{v}_g}{\rho_m} \tag{34}$$

The mixture turbulent viscosity is calculated from

$$\mu_{T,m} = C_\mu \rho_m \frac{k^2}{\epsilon} \tag{35}$$

where C_μ=0.09. The production term $G_k$is computed from

$$G_k = \mu_{\mathrm{T},m}\left(\nabla\vec{v}_m + (\nabla\vec{v}_m)^{\mathrm{T}}\right) : \nabla\vec{v}_m \tag{36}$$

The *k-ϵ* mixture turbulence model is suitable when flow is stratified, the density ratio is close to 1 or phases separate [15]. The *k-ϵ* mixture turbulence model is also considered applicable and commonly used in bubble flows.

4. MEWA2014 test calculations

This chapter documents the testing and validation of the MEWA simulation code version that was distributed to VTT by the University of Stuttgart in March 2014. The validation has been done against the previous version in use at VTT (distribution in 2008). The new version is referred as MEWA2014 and the old as MEWA2008 although no official version numbers have been assigned. MEWA2014 is also used in the simulations of the truncated cone experiment in Chapter 5.

4.1 Drag force testing

A simple flow-through test with a 10 x 21 Cartesian grid (50 mm cells size) was performed with a given mass flux boundary condition for gas and liquid at the bottom and a free-flow boundary at the top. No heating or gravity was taken into account. The given mass fluxes were 0.2 kg/m^2/s for liquid and 0.08 kg/m^2/s for gas. Porosity and particle diameter were 40% and 1 mm, respectively. The phase velocities are calculated from the mass fluxes q_m (kg/m^2/s)

$$v_l = \frac{q_{m,l}}{\rho_l \varepsilon \alpha} \tag{37}$$

$$v_g = \frac{q_{m,g}}{\rho_g \varepsilon \alpha} \tag{38}$$

which yields initial velocities of $v_l = 0.00104$ m/s and $v_g = 0.650$ m/s for fluid density at 1 bar saturated conditions, and with the initial volume fraction α of 0.5 for both phases. The case was simulated with the “old” and “new” code versions, MEWA2008 and MEWA2014. The results are compared by means of pressure loss and saturation (liquid volume fraction in the pore space) in steady-state. Figure 16 - Figure 21 show the pressure and saturation along the length of the modelled pipe obtained with three commonly-used drag force models: Reed, Tung and Dhir and modified Tung and Dhir (see Section 3.2).

It is seen that the Reed model predictions of pressure and saturation are almost the same in the old and new versions. This is also true for the MTD model. A larger difference is seen in the TD model. The maximum differences in the predicted liquid saturations in percentage points are as follows. Reed: 0.05, TD: 0.84, MTD: 0.03.

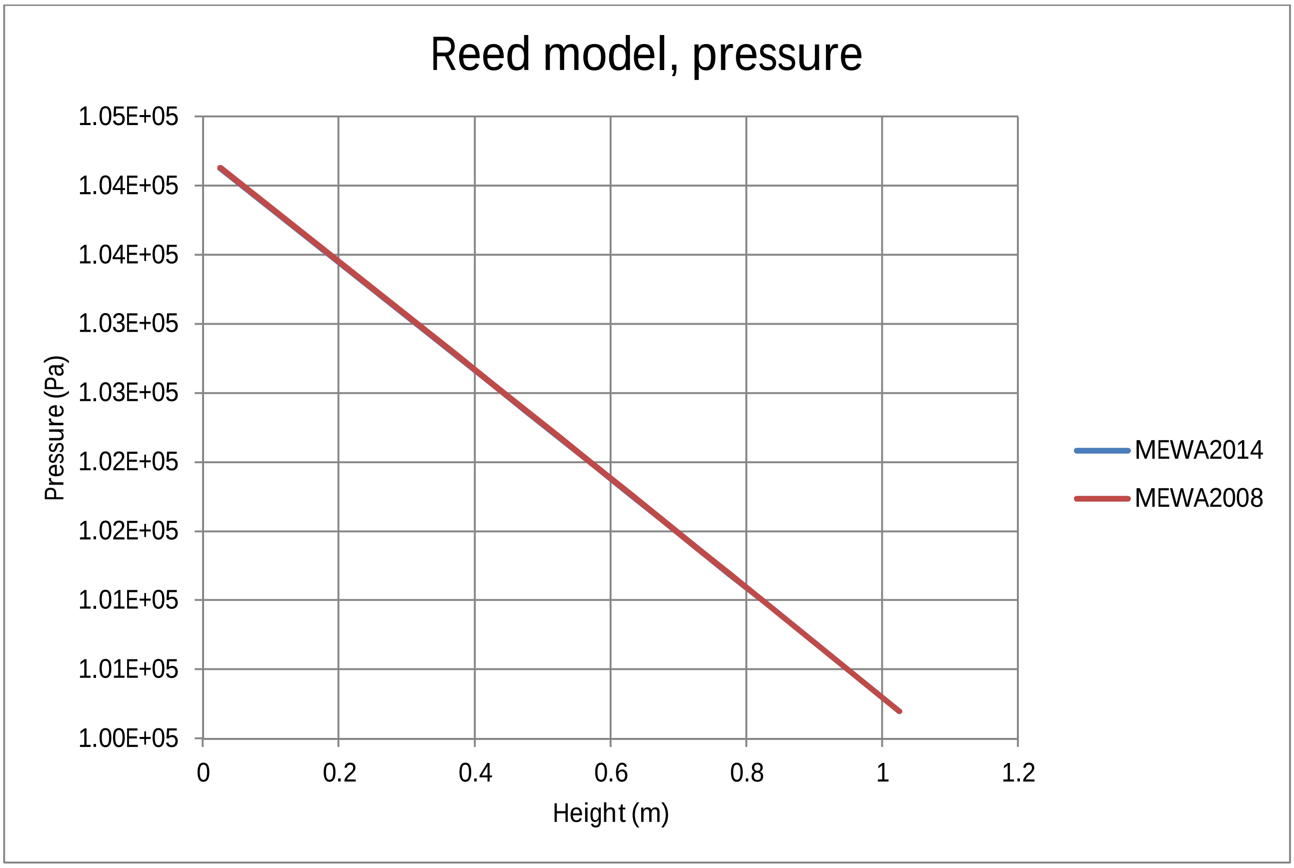

Figure 16. Pressure vs. height in a porous pipe calculated with the Reed model.

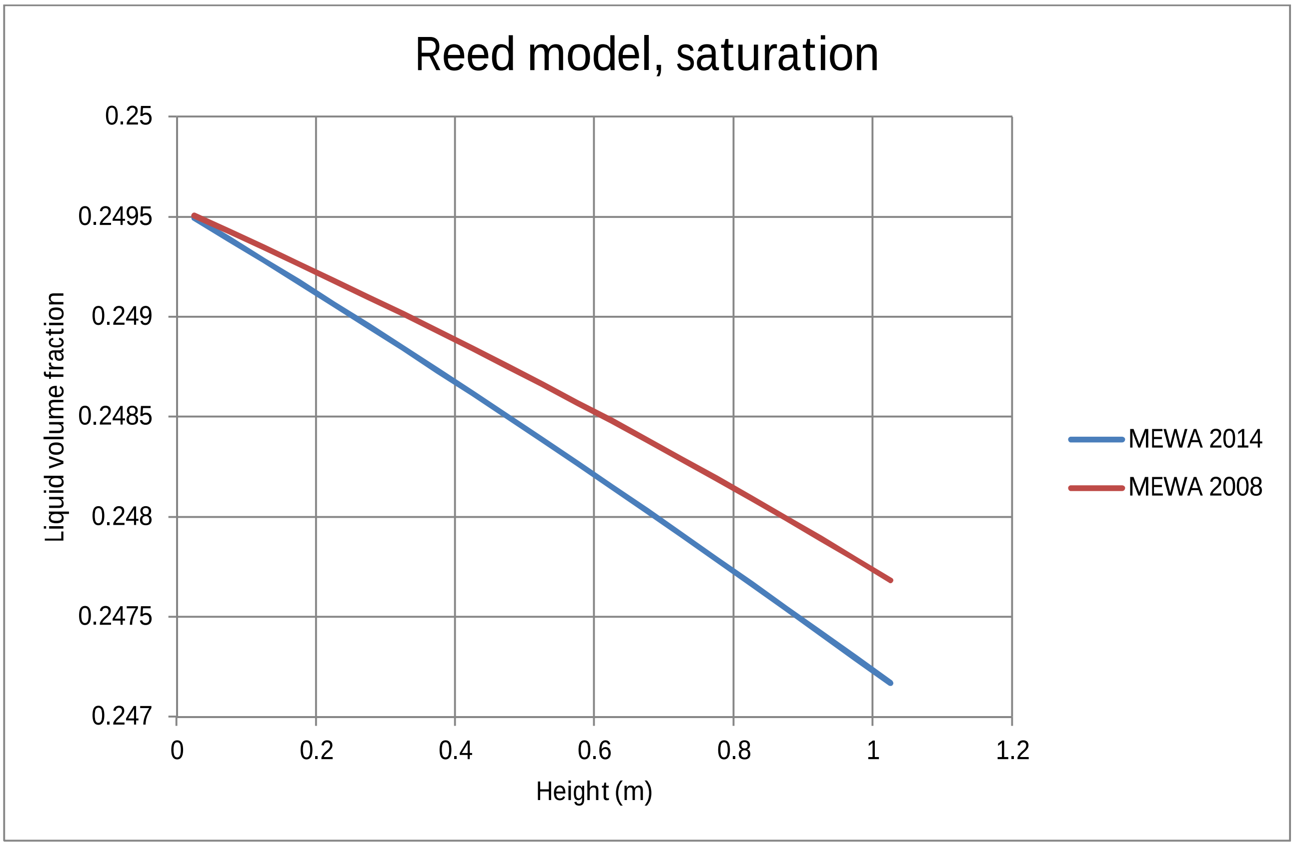

Figure 17. Saturation vs. height in a porous pipe calculated with the Reed model.

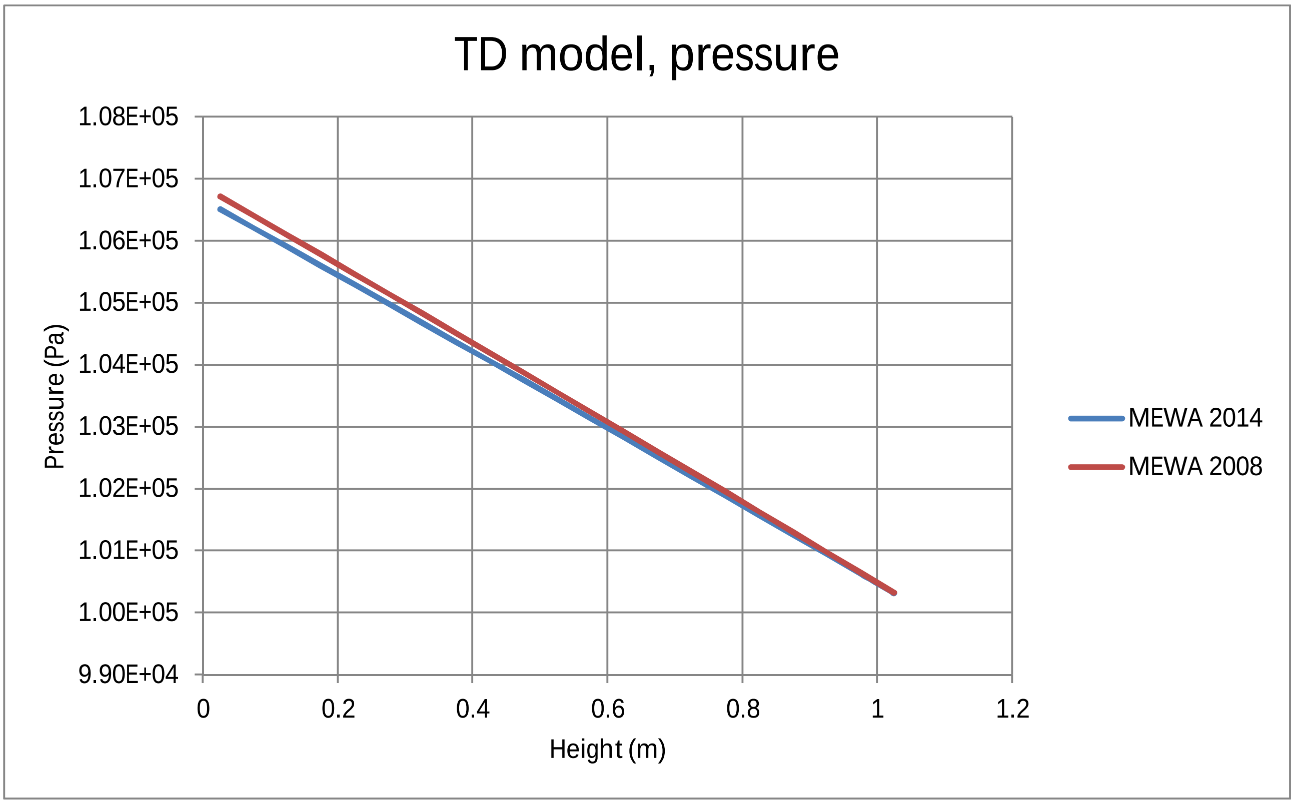

Figure 18. Pressure vs. height in a porous pipe calculated with the Tung & Dhir model.

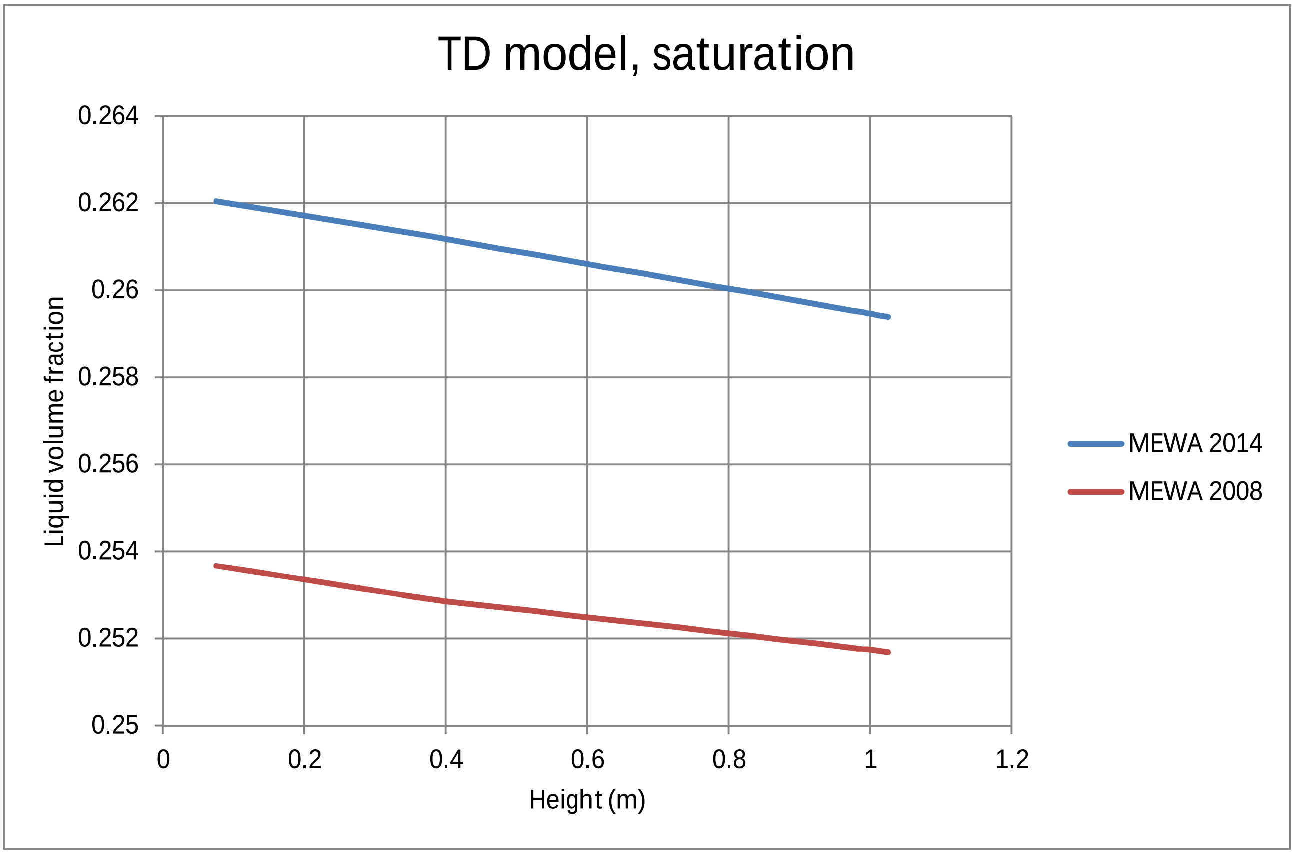

Figure 19. Saturation vs. height in a porous pipe calculated with the Tung & Dhir model.

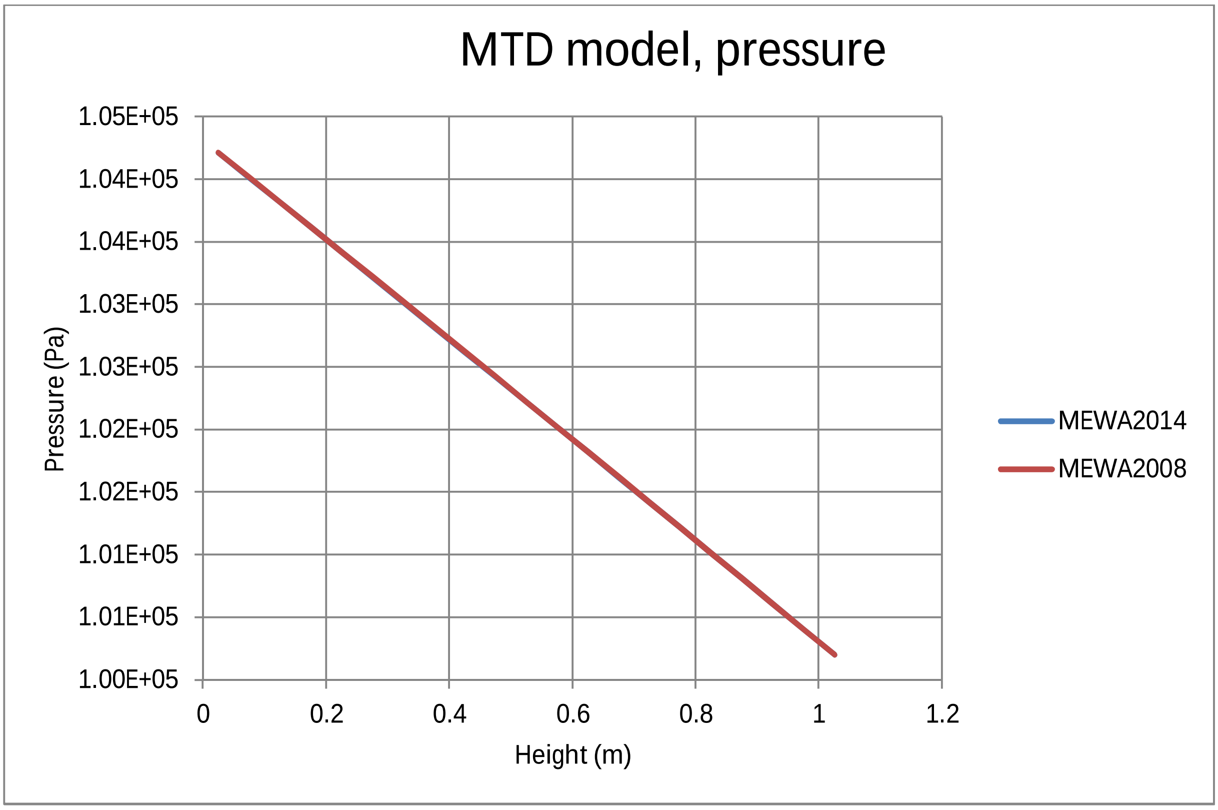

Figure 20. Pressure vs. height in a porous pipe calculated with the modified Tung & Dhir model.

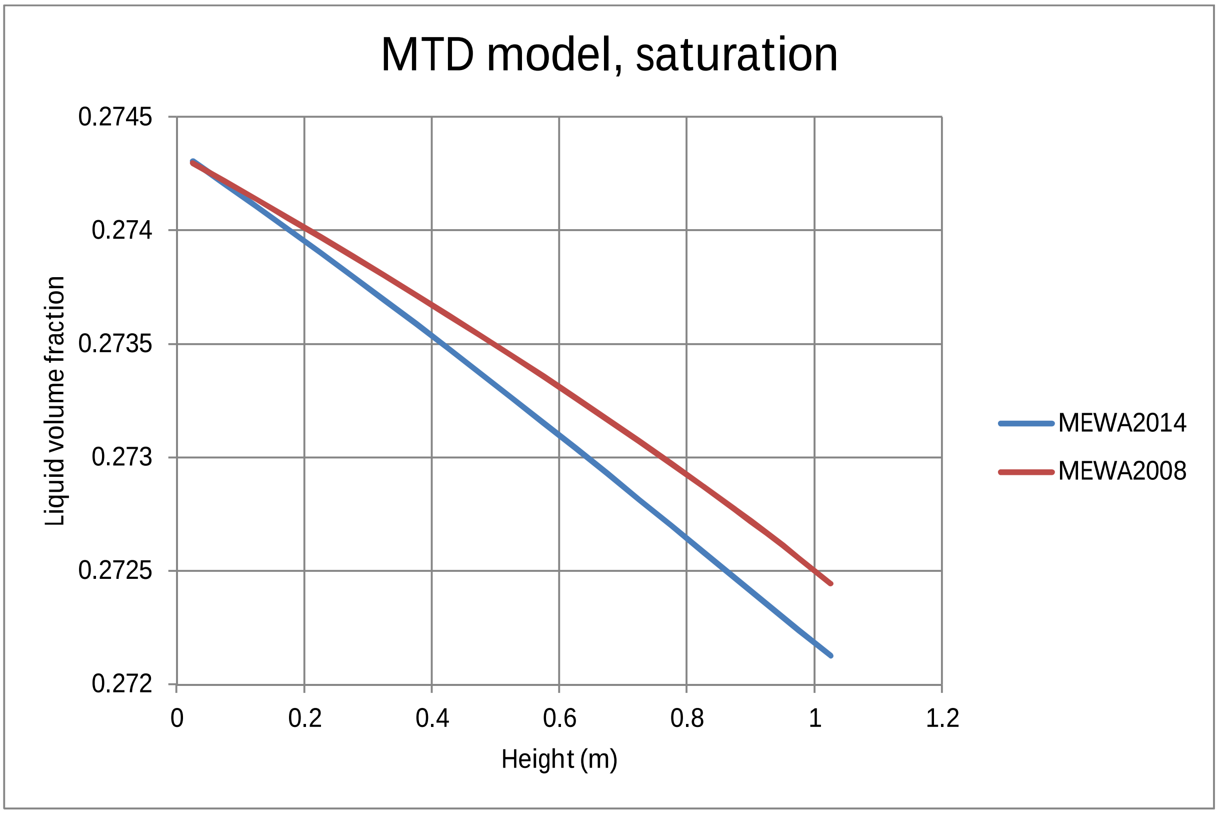

Figure 21. Saturation vs. height in a porous pipe calculated with the modified Tung & Dhir model.

4.2 Cylindrical bed

The performance of the MEWA version 2014 was tested with the cylindrical test bed of the COOLOCE experiments (homogenously heated 1D configuration). The computational grid was a 2D Cartesian grid with 62x112 cells. The results were compared to those obtained with the previous code version. The comparison of axial saturation profiles at 1.1 bar and 2.1 bar pressures in coolable steady-states are shown below.

The simulations were run with the Reed drag force model. Because the input formats are different in newer and older the code version, the input for the new version was created from scratch, following the old input as closely as possible. The bed porosity was 40% and the particle size 0.8 mm. The saturation profiles are almost identical as shown in Figure 22 and Figure 23. The absolute differences in the predicted minimum saturations between the code versions are 0.0034 percentage points for the 1.1 bar (16 kW) case and 0.022 percentage points for the 2.1 bar case.

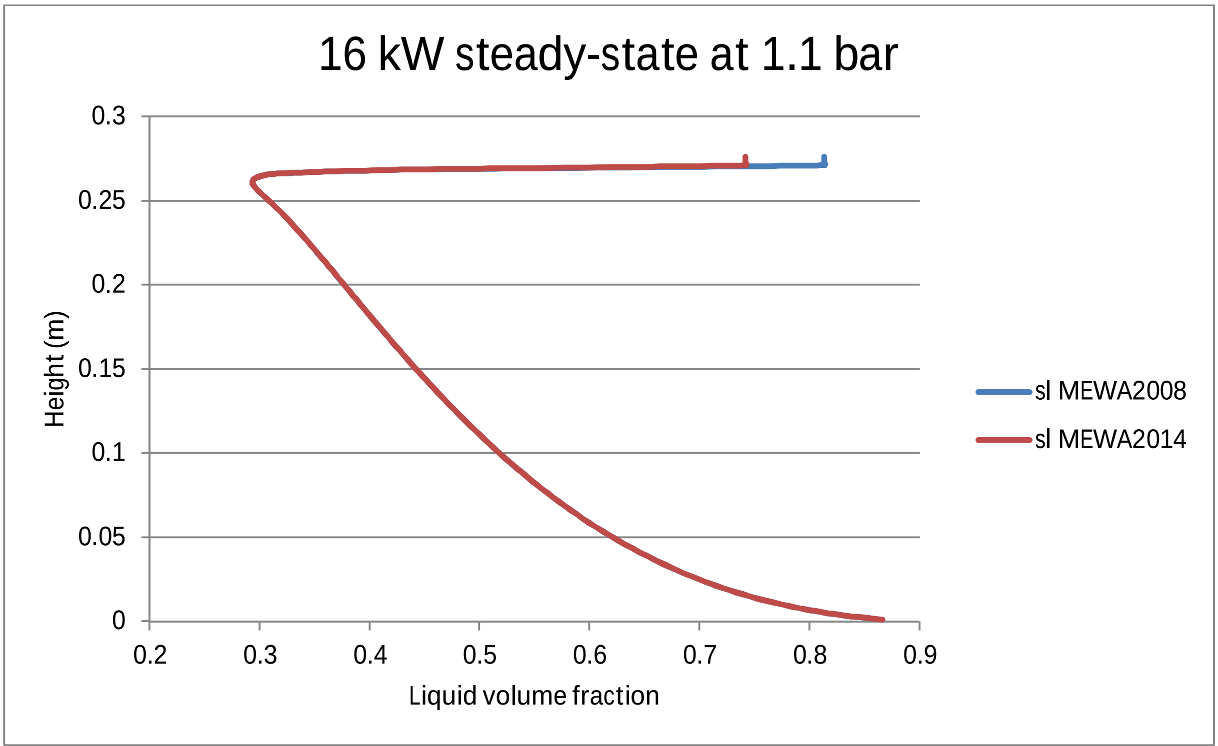

Figure 22. Axial saturation profile in the cylindrical bed calculated with the Reed model, 1.1 bar steady-state.

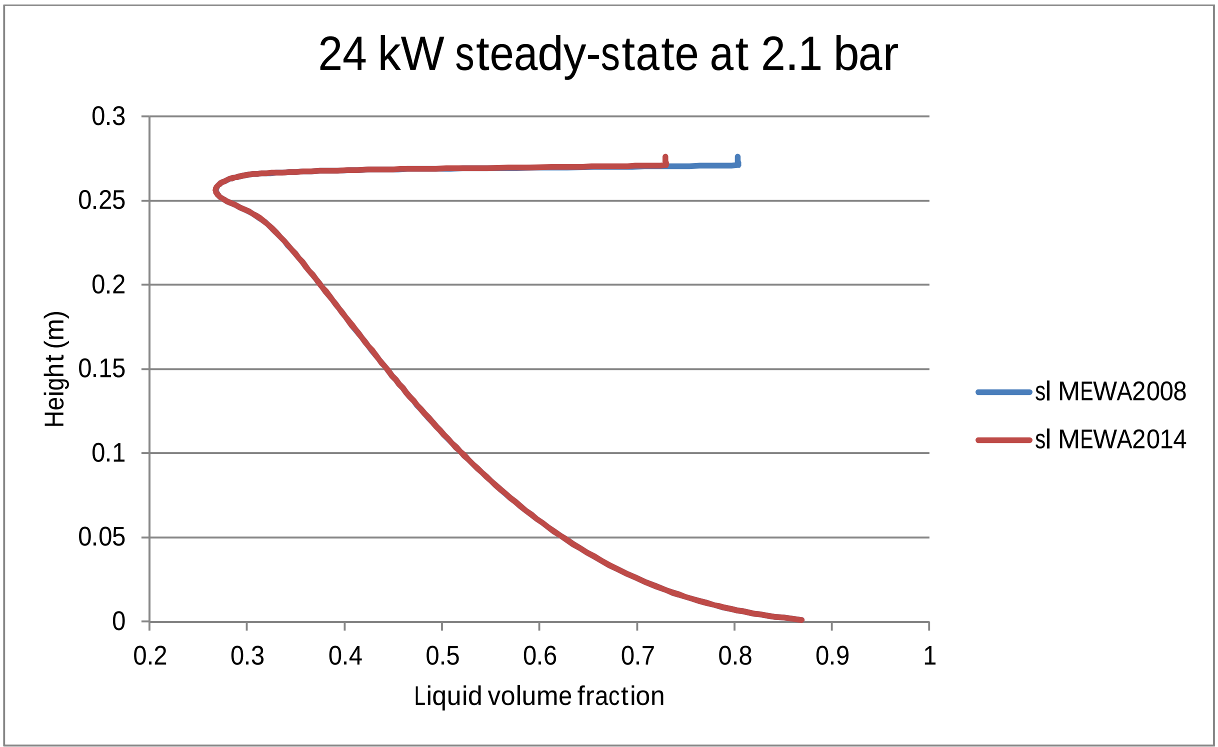

Figure 23. Axial saturation profile in the cylindrical bed calculated with the Reed model, 2.1 bar steady-state.

The dryout power and the heat flux for the 1D cylindrical test bed for 1-7 bar pressure is presented in Figure 24. With the accuracy of 1 kW, the old and new code version predict the same dryout power (and dryout heat flux).

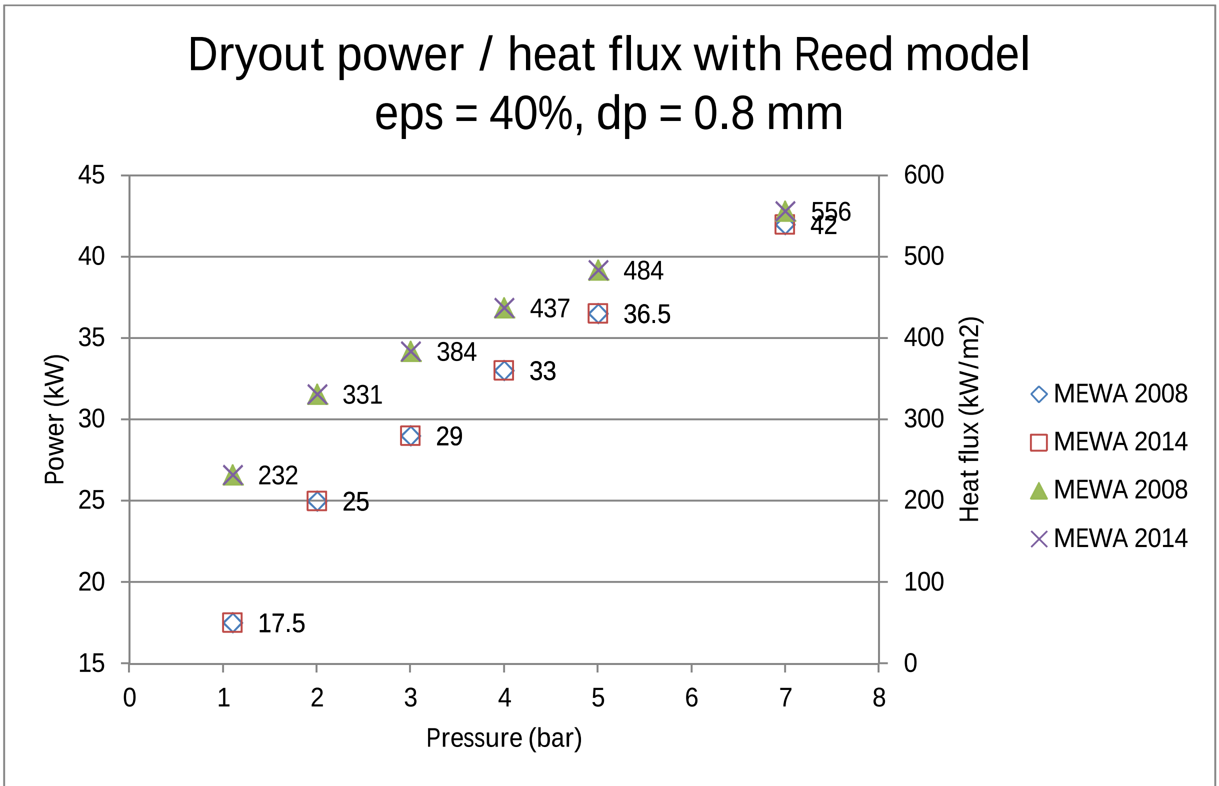

Figure 24. Dryout power and heat flux in the cylindrical bed for the pressure range of the COOLOCE experiments.

4.3 Conical bed

Next, the comparison of the simulation results in the case of the conical bed geometry is presented. The modified Tung & Dhir model was used in the simulations. The bed porosity was 39% and the particle size was 0.95 mm.

The dryout power in the case of fully conical bed is 30 kW in the new code version which is greater than the one in the previous version where void reaches 1.0 at 26.0 kW. The vertical saturation profiles, i.e. line plots at three different radial locations, are shown in Figure 25 for MEWA2008 and MEWA2014. Line plots at corresponding locations are also shown for the temperature of solid particles (Figure 26). The figures represent a quasi-steady state at 30 kW power, after dryout has been reached in the tip of the cone.

The void fraction maps for MEWA2008 and MEWA2014 in 34 kW quasi steady-state in post-dryout conditions are illustrated in Figure 27. The grid is also shown. In this case both models have reached dryout but the dry zone is somewhat larger in MEWA2008. The void fraction maps with the vectors of liquid velocity in MEWA2008 and MEWA2014 at 30 kW power are shown in Figure 28 and Figure 29.

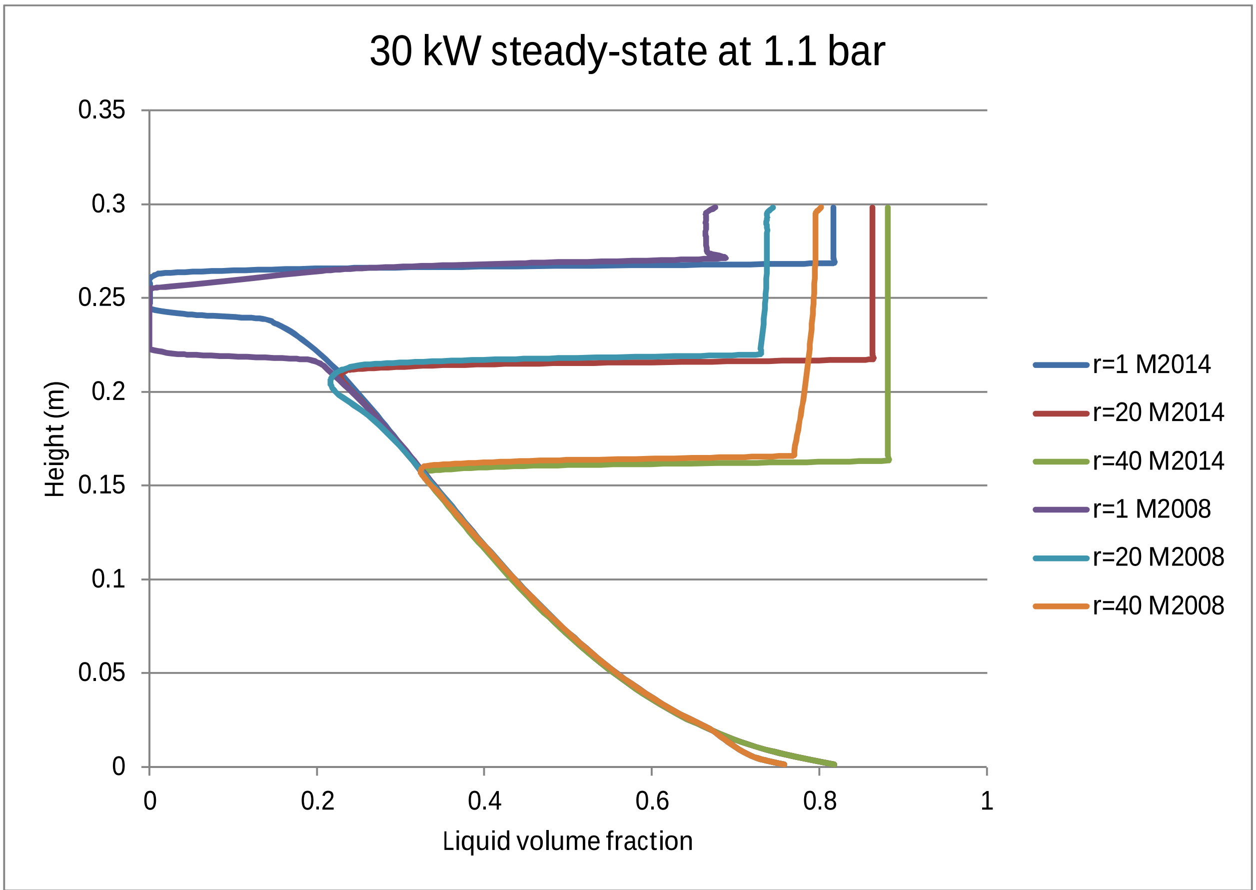

Figure 25. Axial saturation profiles in the conical bed at different radial positions.

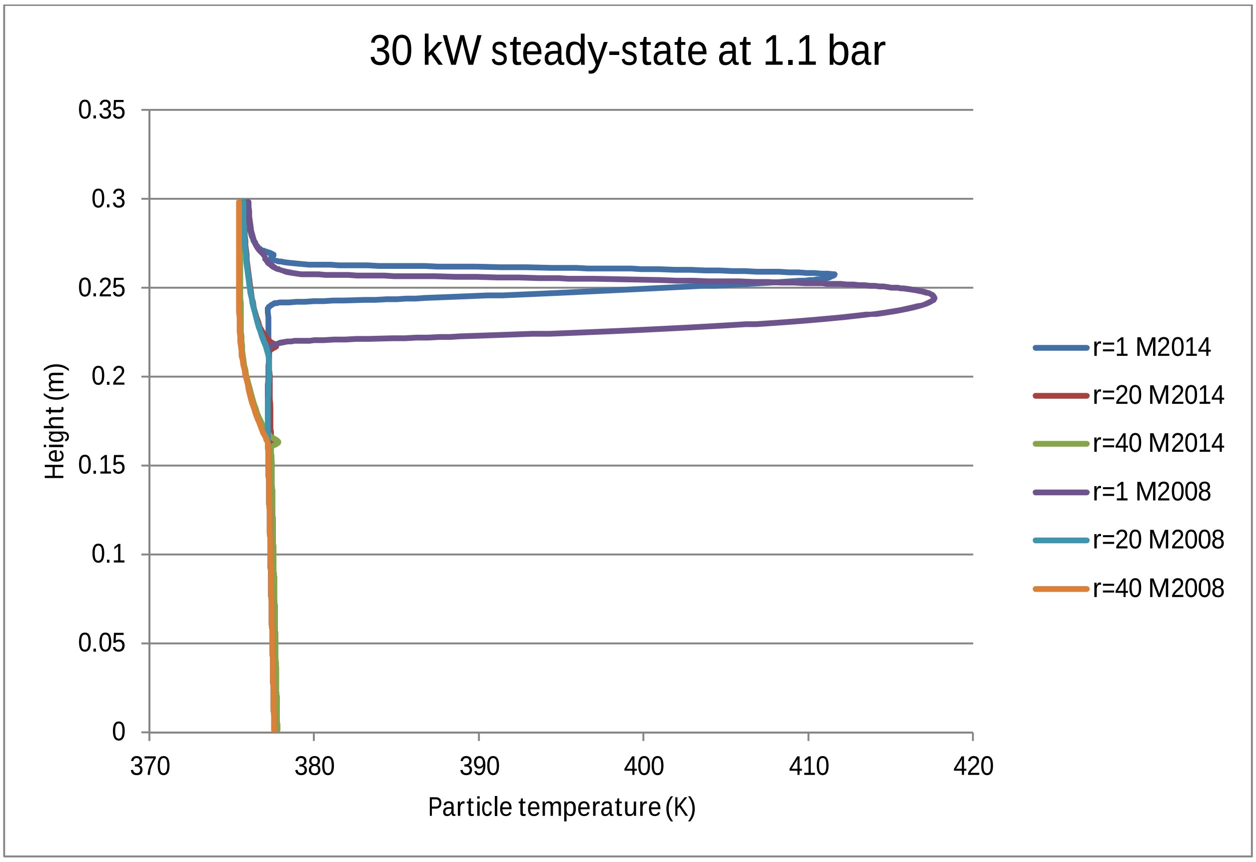

Figure 26. Axial particle temperature profiles in the conical bed at different radial positions.

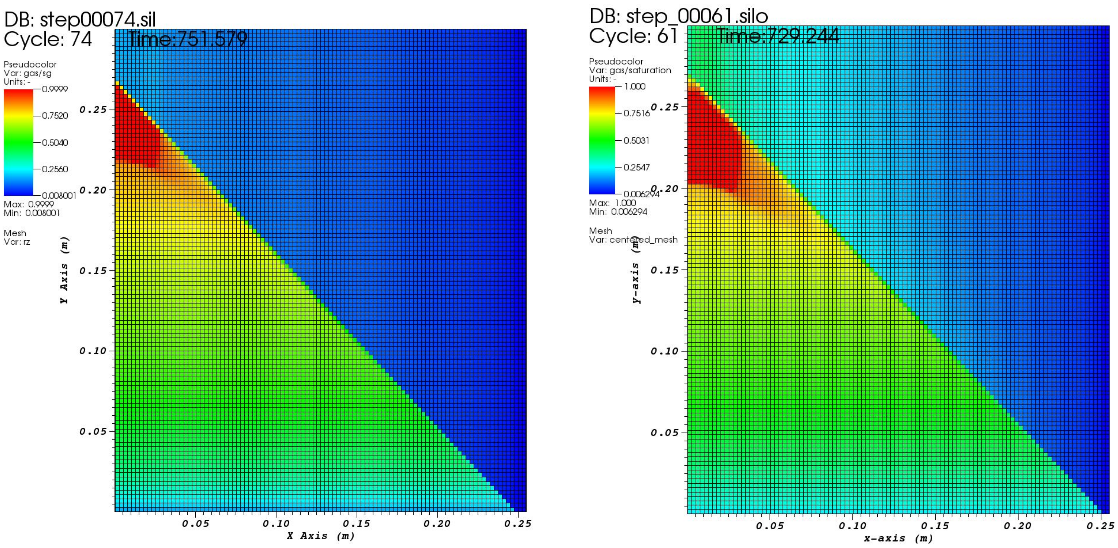

Figure 27. Void fraction distributions in quasi-steady state, 34 kW power, calculated with MEWA2014 (left) and MEWA2008 (right).

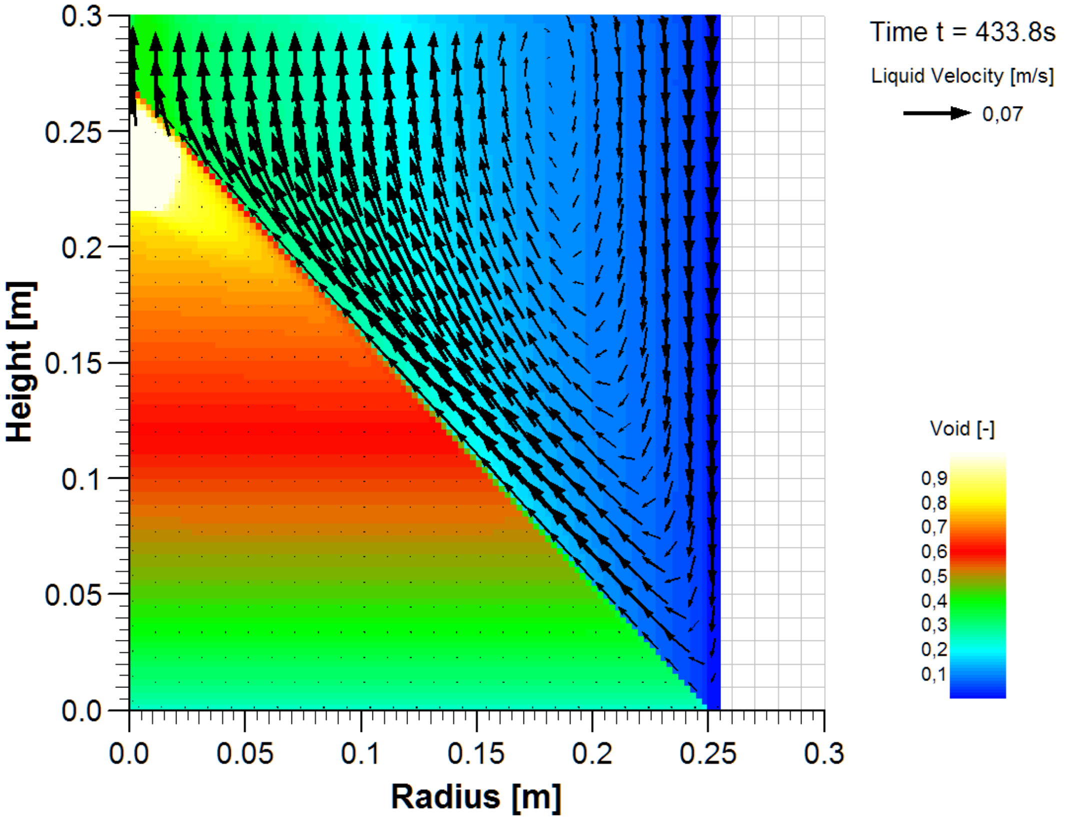

Figure 28. Void fraction distributions in quasi-steady state, 30 kW power, calculated with MEWA2008. Pool model set to ε=0.90, dp=0.01 m.

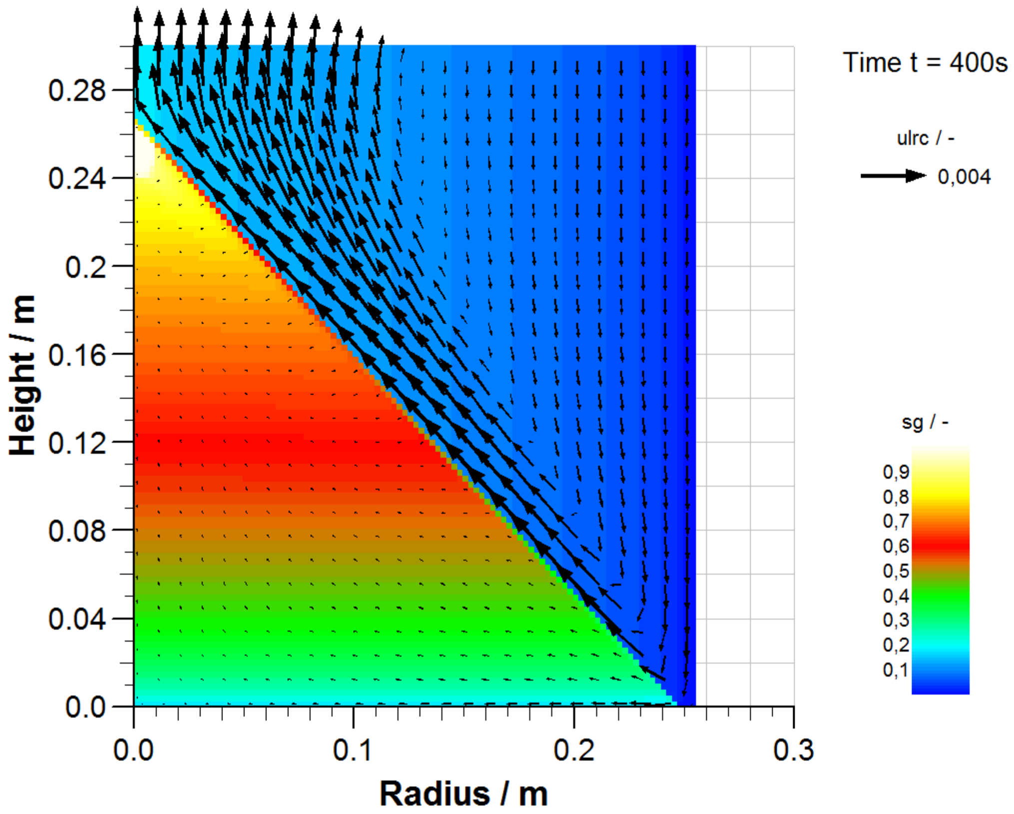

Figure 29. Void fraction distributions in quasi-steady state, 30 kW power, calculated with MEWA2014. Pool model set to ε=0.90, dp=0.01 m.

4.4 Summary of the validation calculations

The drag force tests conducted using a very simple geometry of uniform porous medium show that, compared to MEWA2008, the new code version predicts a greater saturation in the case of TD model but only a small difference is seen in the cases of the Reed and MTD models.

In the case of the cylindrical test bed modelled with the Reed model, MEWA2008 and MEWA2014 predict the same dryout power (with the accuracy of 1 kW) and the saturation profiles are almost identical. This confirms that the Reed model yields the same results in the old and new versions.

For the conical test bed, the new version predicts improved coolability compared to the old version. This is seen in the saturation maps of the conical bed simulation as well as in the particle temperature after dryout. This is regardless of the drag force test which suggests that the models in the old and new versions give very similar results. However, the drag force test was done without heating or without any variation of the boundary conditions or the flow direction. It is possible that the model behaves differently in the conical bed.

5. Truncated cone simulations

The models and simulation results of the truncated cone experiment are addressed in this Chapter. In the MEWA simulations, the main focus is on comparing the experimental and simulated dryout power with the objective of finding out how well the experimental dryout power is predicted by the models.

In the CFD simulations with Fluent, the underlying mechanisms that affect the dryout formation are investigated by examining the saturation distributions, temperatures and velocities in the debris bed and the surrounding water pool. This improves the general understanding of the flow phenomena in the debris bed-pool system and, thus, the formation of dryout is elucidated in a manner that could not be achieved only by dryout power comparisons.

In the MEWA modelling two types of models of the debris bed were applied. The models differ in the heating power distribution. First, it is assumed that the power density is constant (homogenous) in the full volume of the debris bed. In previous studies it has been shown that this approach is capable of predicting the experimental dryout power with at least reasonable accuracy for the conical and the cylindrical debris bed geometries [11]. In the alternative approach, the bed is heated only partially: the unheated layer of particles above the heaters of the test bed is also unheated in the model. This means that the power density is somewhat greater in the heated volume (for constant total power).

The Fluent simulations also apply the partially heated bed. The pool is modelled as a high porosity porous zone (MEWA pool) and, more realistically, as a free-flow zone. The Fluent model has been used for testing of the effects of the different options of the numerical solver. It has been examined whether the numerical solver options available to the user are significant in determining the dryout power.

As a default, the MTD model with interfacial drag was applied. However, some of the simulations were run with the Reed model which has the advantage of faster simulation times. The key model parameters, porosity and particle diameter, were 0.39 and 0.95 mm. Simulations and discussion concerning the sensitivity of the results to these model parameters can be found in previous works that address the modelling of the COOLOCE experiments [29, 30, 9].

5.1 MEWA simulations

Pre- and post-test simulations of the COOLOCE-13 were performed with the objective of finding out the dryout power by using stepwise power increases. This is basically the same procedure than in the experiments. The pressure levels of 1.4 bar (C-13) and 1.25 bar (C-13R) were both addressed in the simulations. The computational grid shown in Figure 30 is axisymmetric Cartesian 2D grid with high density. The cell size is 0.27 mm in axial direction and 0.25 mm in radial direction (102 x 111 cells).

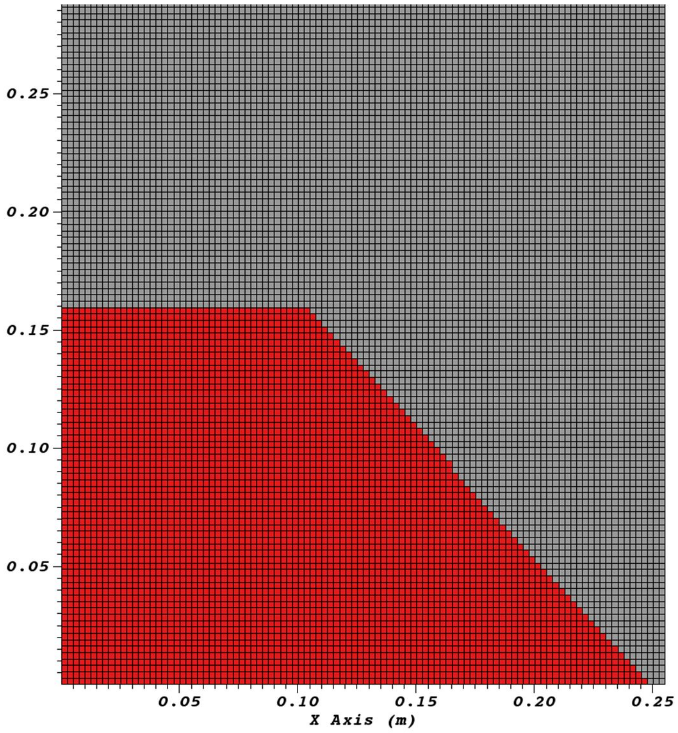

Figure 30. MEWA grid.

5.1.1 Homogenously heated bed

It was found that in the case of 1.4 bar, the minimum dryout power was 50 kW when the MTD model was applied. This is greater than the one measured in the experiments (43.5 kW) by 15%. The contours of void fraction and solid temperature in the simulation at 50 kW power are shown in Figure 31. The case was also simulated with the Reed model, of which results are shown in Figure 32. For the 50 kW power, the dry zone is larger (and coolability poorer) in the case of the Reed model which is in accordance with the expected behaviour of the models with and without explicit consideration of interfacial drag [7, 8].

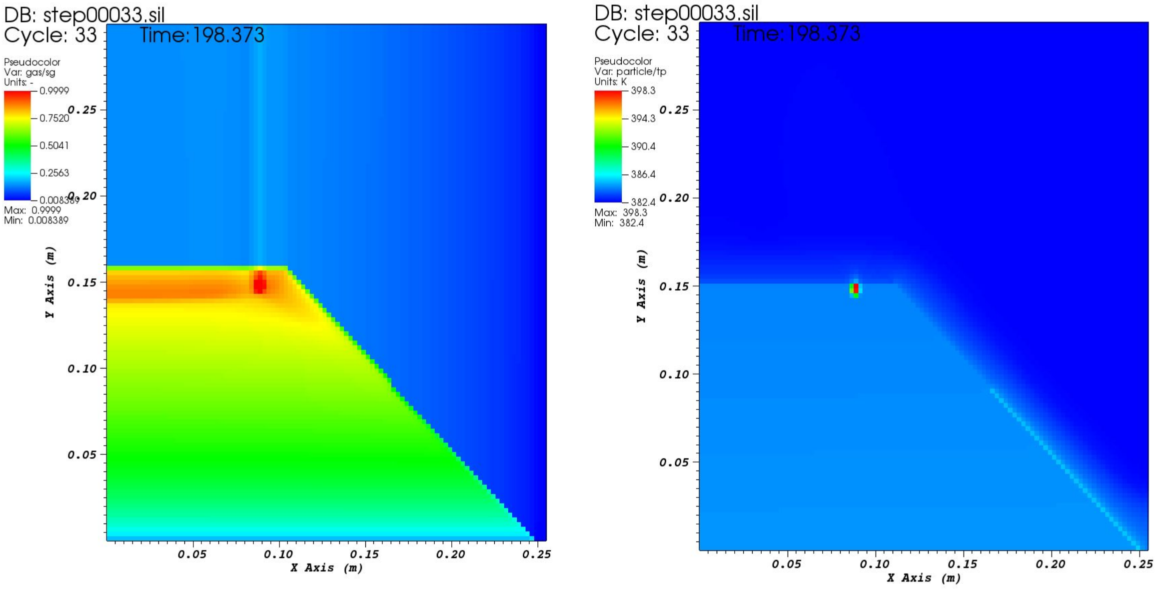

Figure 31. Void fraction distribution (left) and particle temperature (right) in dryout conditions (quasi-steady state), 50 kW power, calculated with the MTD model.

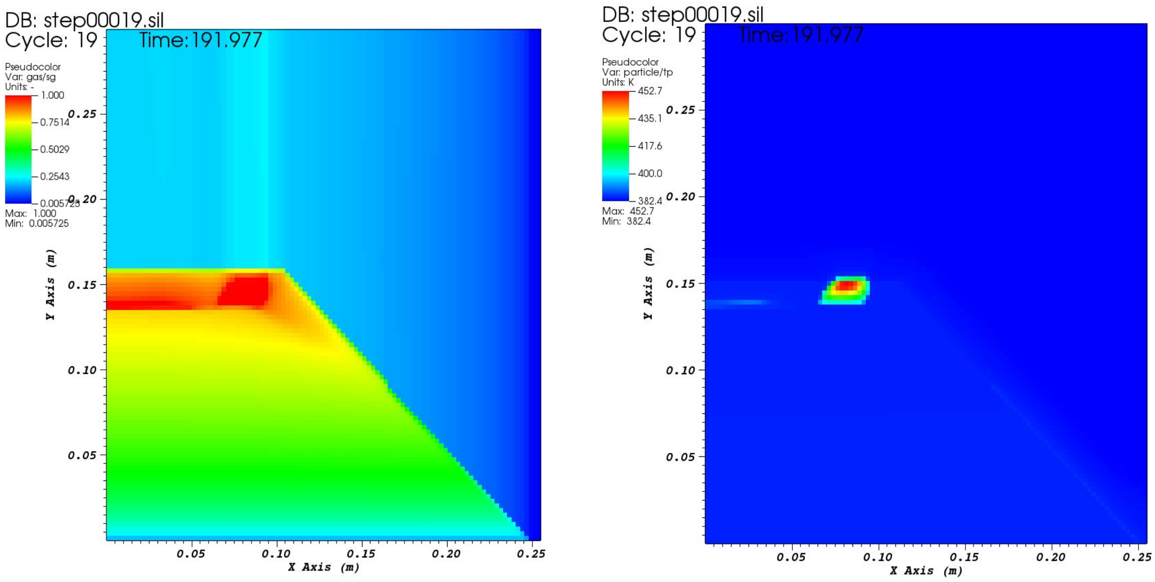

Figure 32. Void fraction distribution (left) and particle temperature (right) in dryout conditions (quasi-steady state), 50 kW power, calculated with the Reed model.

In the case of the 1.25 bar pressure, the minimum dryout power was 47 kW according to the MTD model. Compared to the experimental results this is about 20% greater. The void fraction and temperature distribution at 47 kW are shown in Figure 33. Figure 34 shows the void and temperature at the coolable conditions with 46 kW power. The maximum void is 0.94 and the temperature remains close to the saturation temperature.

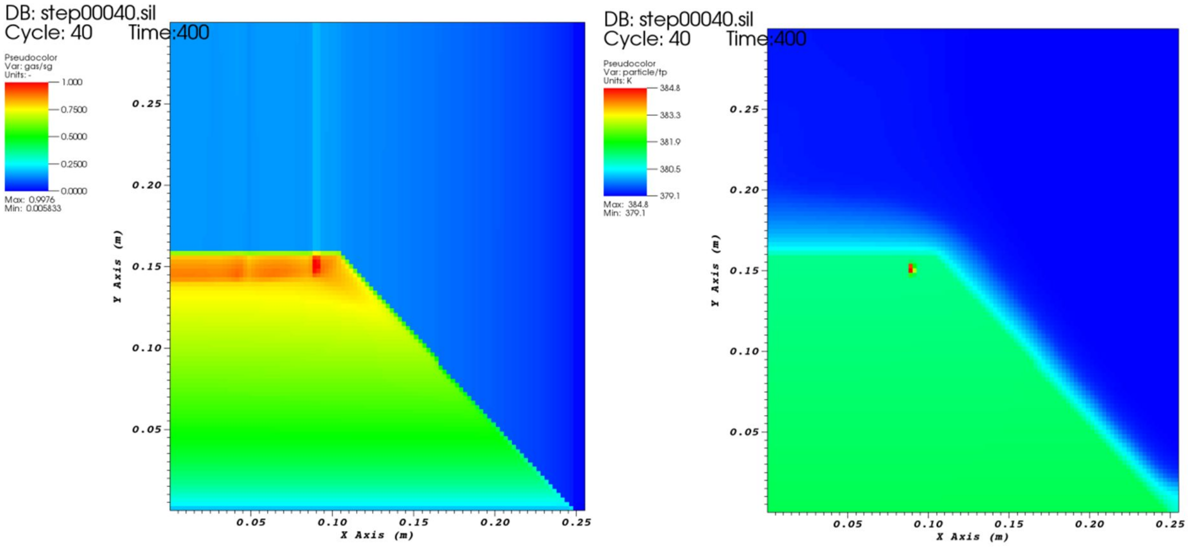

Figure 33. Void fraction (left) and particle temperature (right) distributions at the minimum dryout power of 47 kW calculated with the MTD model.

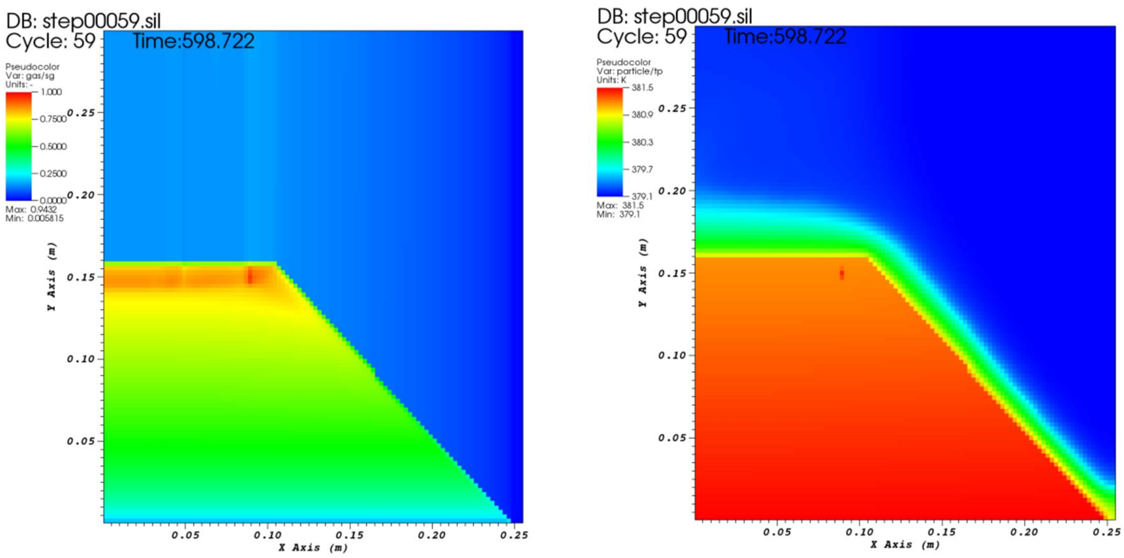

Figure 34. Void fraction (left) and particle temperature (right) distributions at the maximum coolable power of 46 kW calculated with the MTD model. In coolable steady-state, the temperature is close to saturation temperature.

The velocities of liquid and gas at the minimum dryout power are illustrated in Figure 35 and Figure 36. The gas flow is oriented almost directly upwards. Liquid flows down at the outer boundary of the domain, enters the bed through the inclined surface and is directed upwards with the gas flow near the centre of the bed. A zone of counter-current flow exists in the top of the bed in the almost dried out region (void > 0.8).

The void fraction increases to 1.0 first in the corner of the flat part of the bed where also the particle temperature starts to increase. This part is difficult to maintain coolable because the lateral and axial flooding of the liquid phase form a type of vortex which prevents the steam from leaving the bed as easily as in the centre of the bed where, at the surface, the liquid flow turns upwards in the same direction with steam flow.

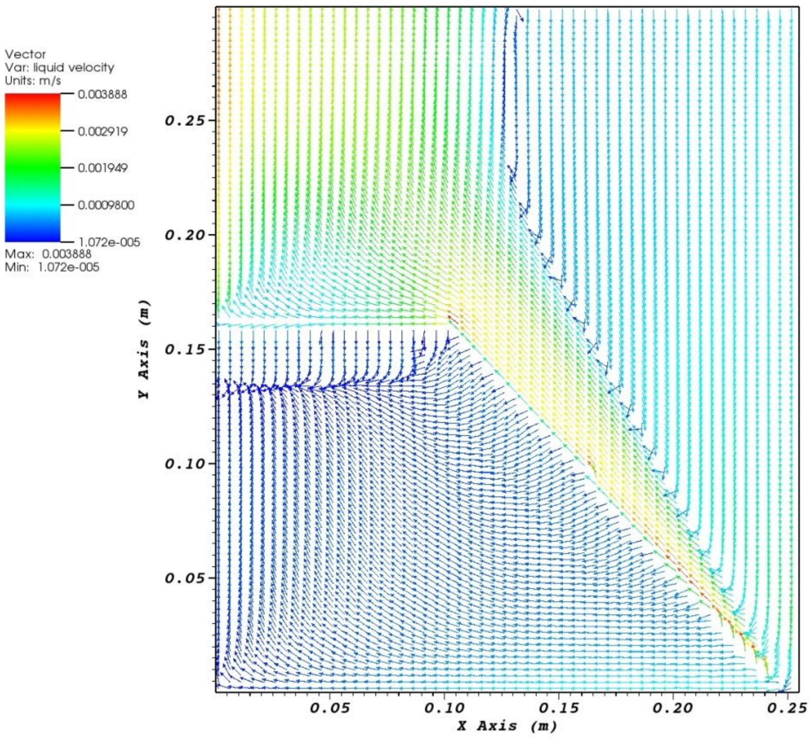

Figure 35. Vectors of liquid velocity at the minimum dryout power of 47 kW calculated with the MTD model.

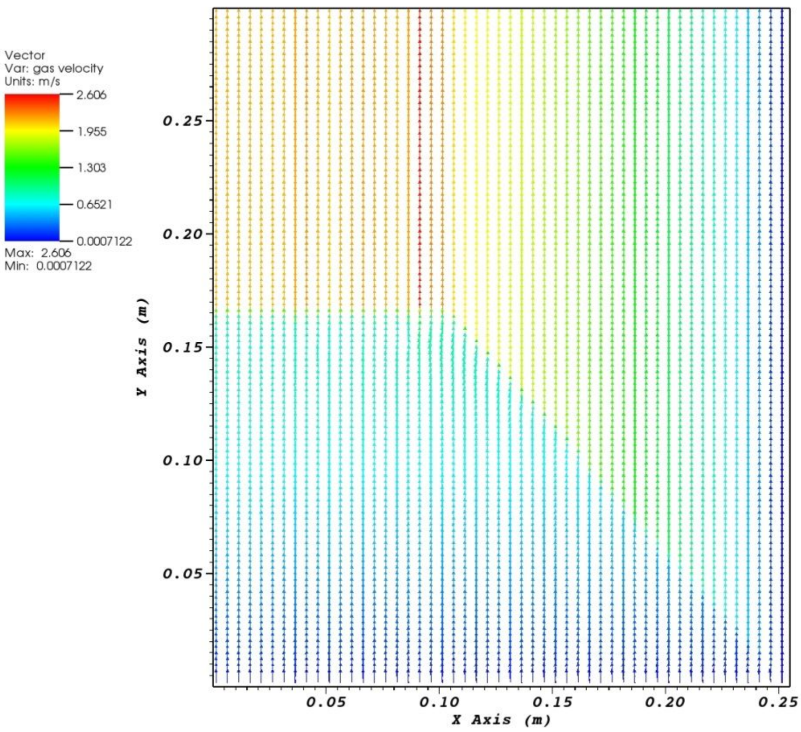

Figure 36. Vectors of gas velocity at the minimum dryout power of 47 kW calculated with the MTD model.

5.1.2 Partially heated bed

The mesh as well as the bed and its heated part are depicted in Figure 37. The total heating power is assumed to be distributed homogenously in the heated part of the bed. Figure 38 shows as a function of the radius the heating power divided by the area of the corresponding circle for the experiment and computations. For circular areas with the radius greater than 100 mm, the average heating power used in the simulations is close to the experimental values.

The MEWA simulations for the partially heated bed were performed as for the homogenously heated bed discussed above. In addition, with the Reed model, the influences of numerical parameters (maximum time step, maximum Courant number, maximum residuals) were examined. As MEWA adjusts the time step (within the given maximum time step), numerical parameters were not found to affect the simulation results as long as the maximum residuals are not too large. Similar study was not possible for the MTD model since the simulation time easily increased drastically and led to impractical long computing times.

Figure 39 - Figure 41 show the MEWA2014 results for partially heated bed assuming the Reed model. The MEWA2014 results for the MTD model are presented Figure 42 - Figure 44. Dryout takes place on the surface of the heated part of the bed and radially at about 2/3 of the radius of the horizontal top surface of the bed. The heating power of 36 kW does not lead to dryout with the MTD model (Figure 42) but with the Reed model a relatively large dry area is obtained (Figure 40). In fact, comparing Figure 39 to Figure 42 and on the other hand Figure 40 to Figure 43, we could estimate that in this case the MTD model predicts about 2 kW higher dryout power.

The dryout power in Figure 43 (38 kW) is rather close to the experimental value of 39.2 kW. The real dryout power can be considered to be within the range specified by the maximum coolable and the minimum dryout power. In the experiment this was 36.9 – 39.2 kW and 36 – 38 kW in the simulation with the MTD model.

With both the models, the gas flows vertically (Figure 41 and Figure 44). The liquid velocity vectors are similar for the Reed and MTD models especially in the bed. In the pool area, the artificial friction is smaller for the Reed model and small disturbances appear likely because of numerical inaccuracies. The magnitude of the liquid velocity is small everywhere. The difference of the vertical gas and liquid velocities is unphysically high in the pool area. The artificial friction forces slow down the liquid velocity and the MEWA2014 code possesses no interaction force between the phases, when the porosity is higher than 0.8.

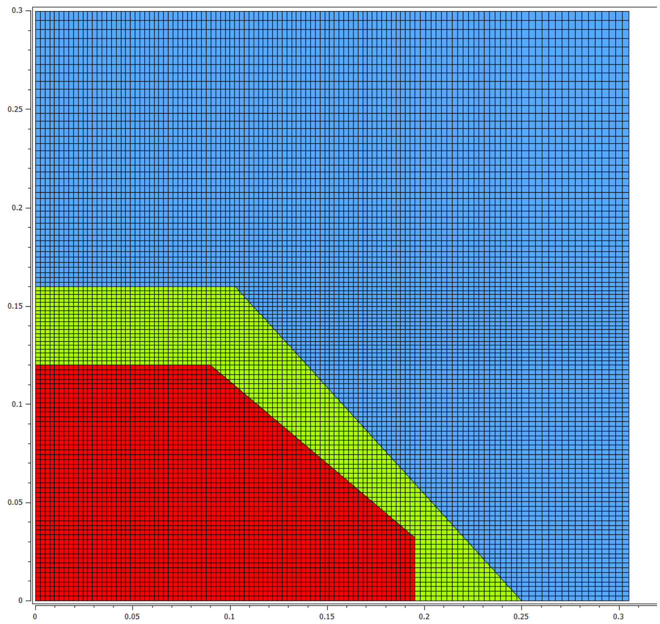

Figure 37. Mesh with representations of the particle bed (green and red area) and the heated part of the bed (red area) in the MEWA simulations for a partially heated bed.

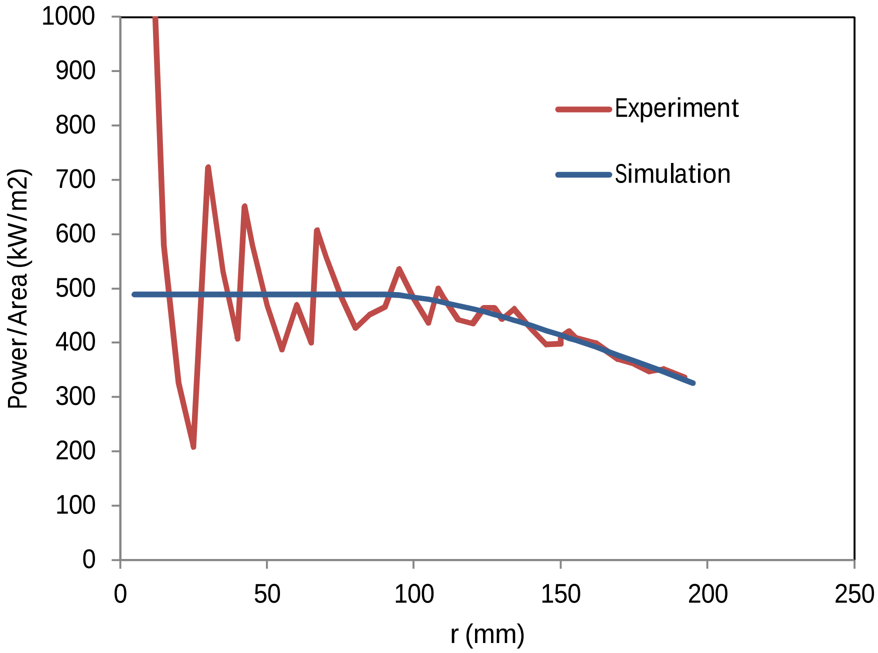

Figure 38. Heating power divided by the area as a function of the radius in the experiment and in the simulations for a partially heated bed.

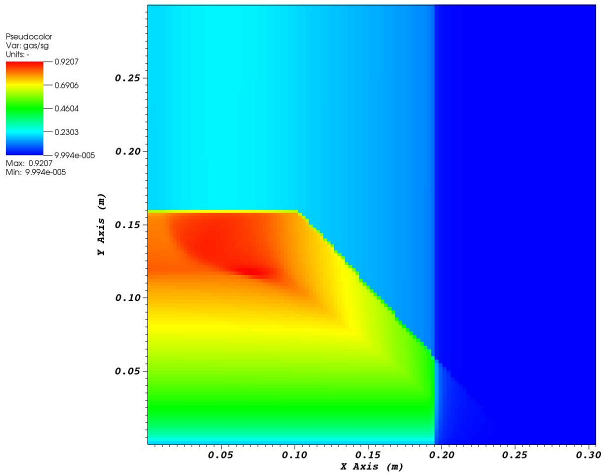

Figure 39. Void fraction distribution in steady state, 34 kW power, calculated for a partially heated bed with the Reed model.

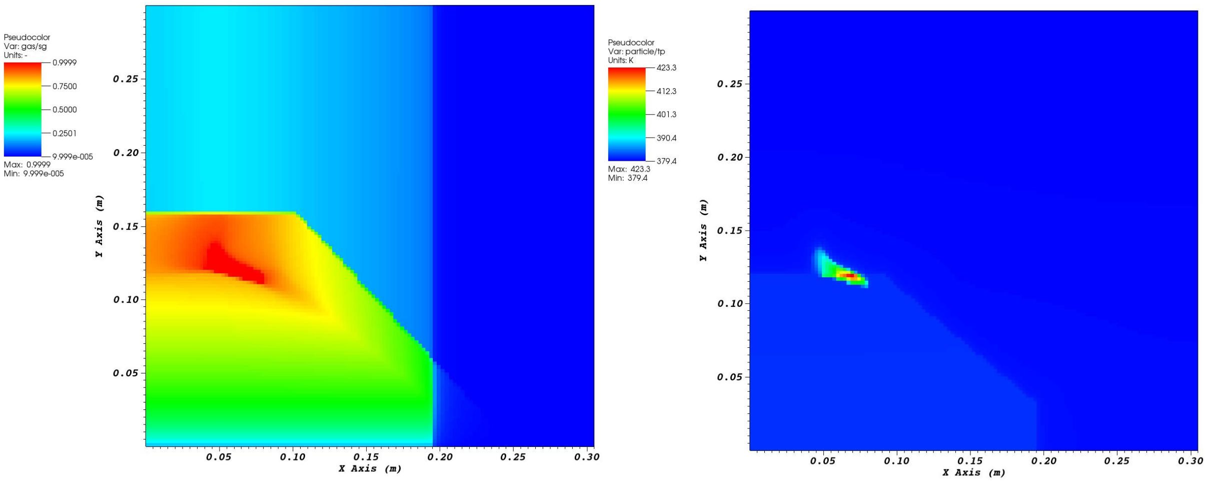

Figure 40. Void fraction distribution (left) and particle temperature (right) in dryout conditions (quasi-steady state), 36 kW power, calculated for a partially heated bed with the Reed model.

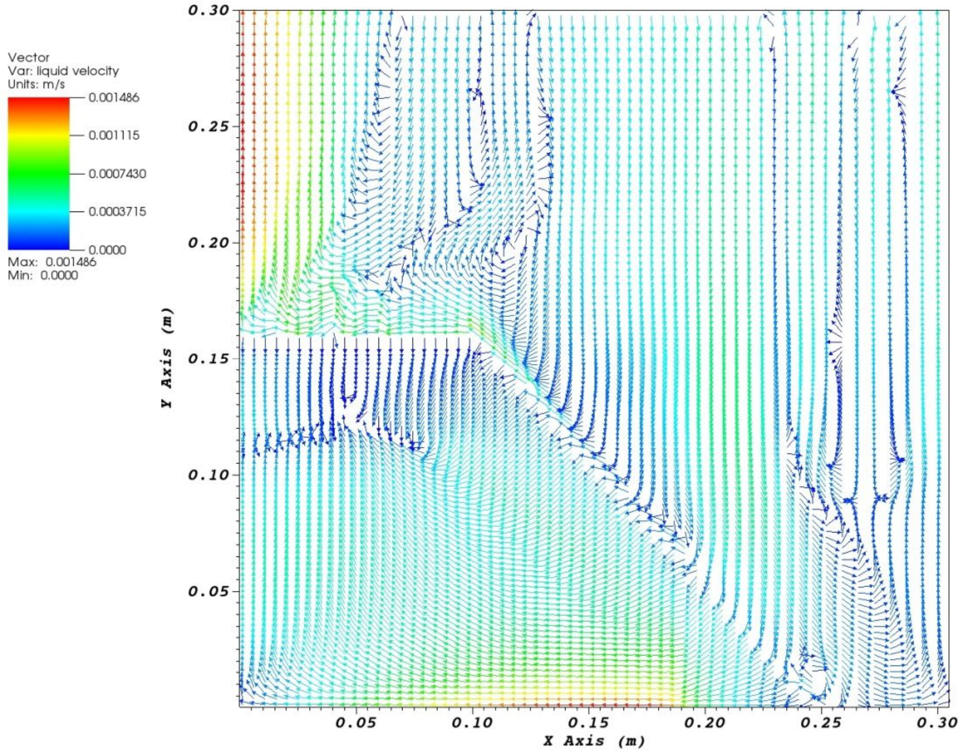

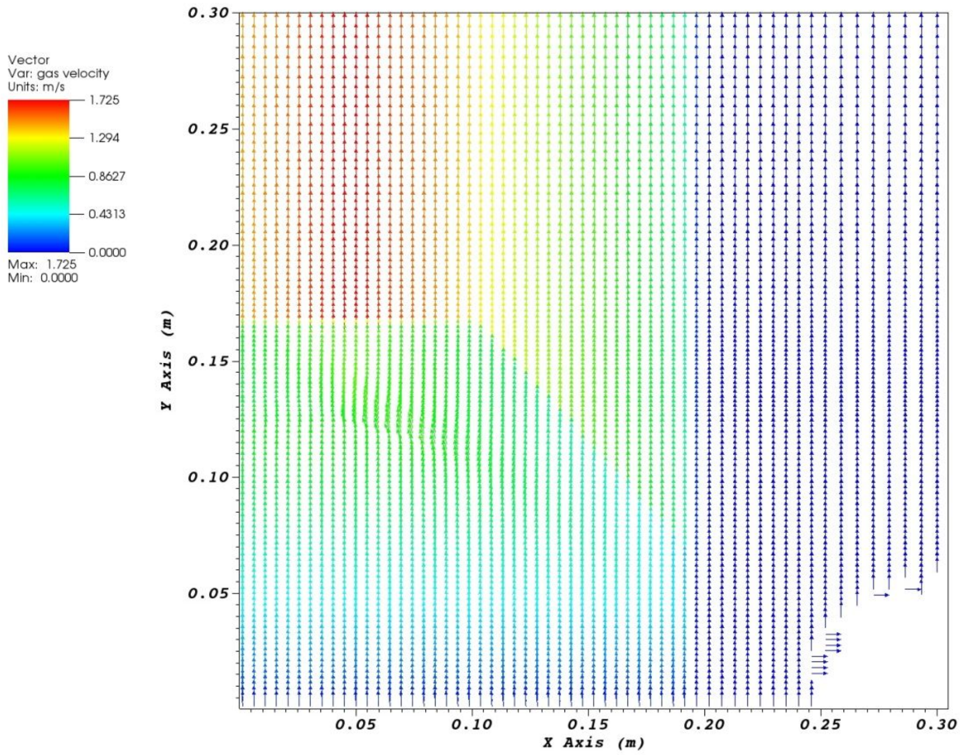

Figure 41. Pore velocity vectors for the liquid (top) and gas phase (bottom) in dryout conditions (quasi-steady state), 36 kW power, calculated for a partially heated bed with the Reed model.

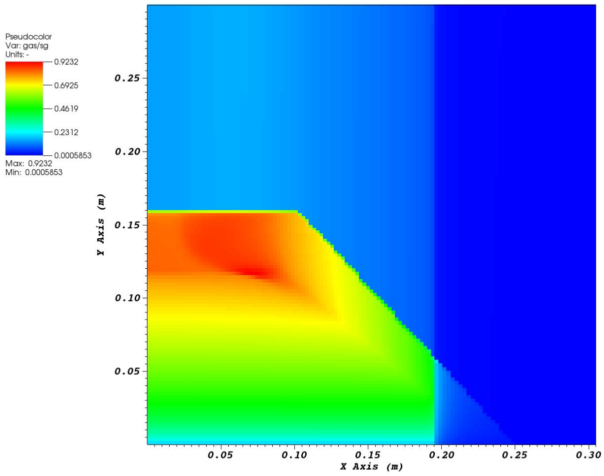

Figure 42. Void fraction distribution in coolable steady state, 36 kW power, calculated for a partially heated bed with the MTD model.

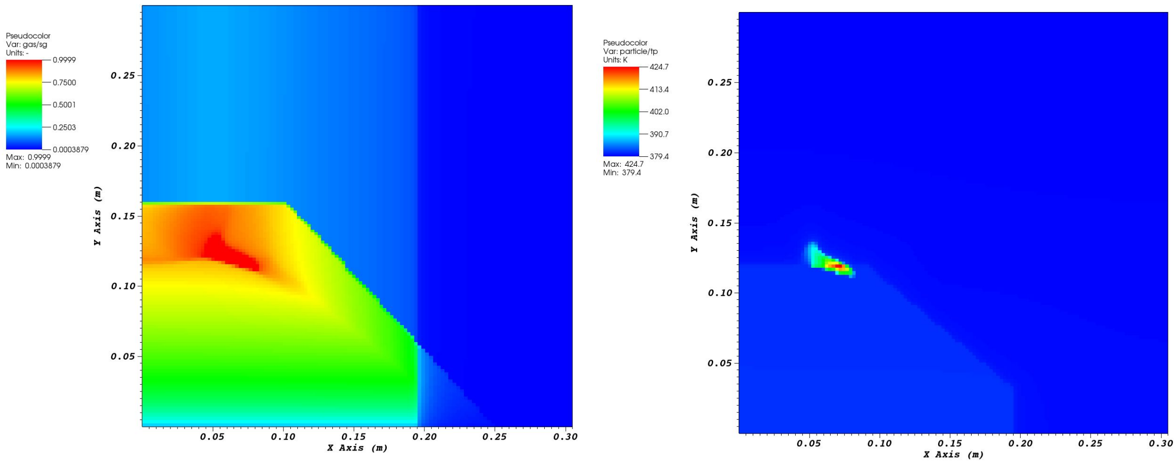

Figure 43. Void fraction distribution (left) and particle temperature (right) in dryout conditions (quasi-steady state), 38 kW power, calculated for a partially heated bed with the MTD model.

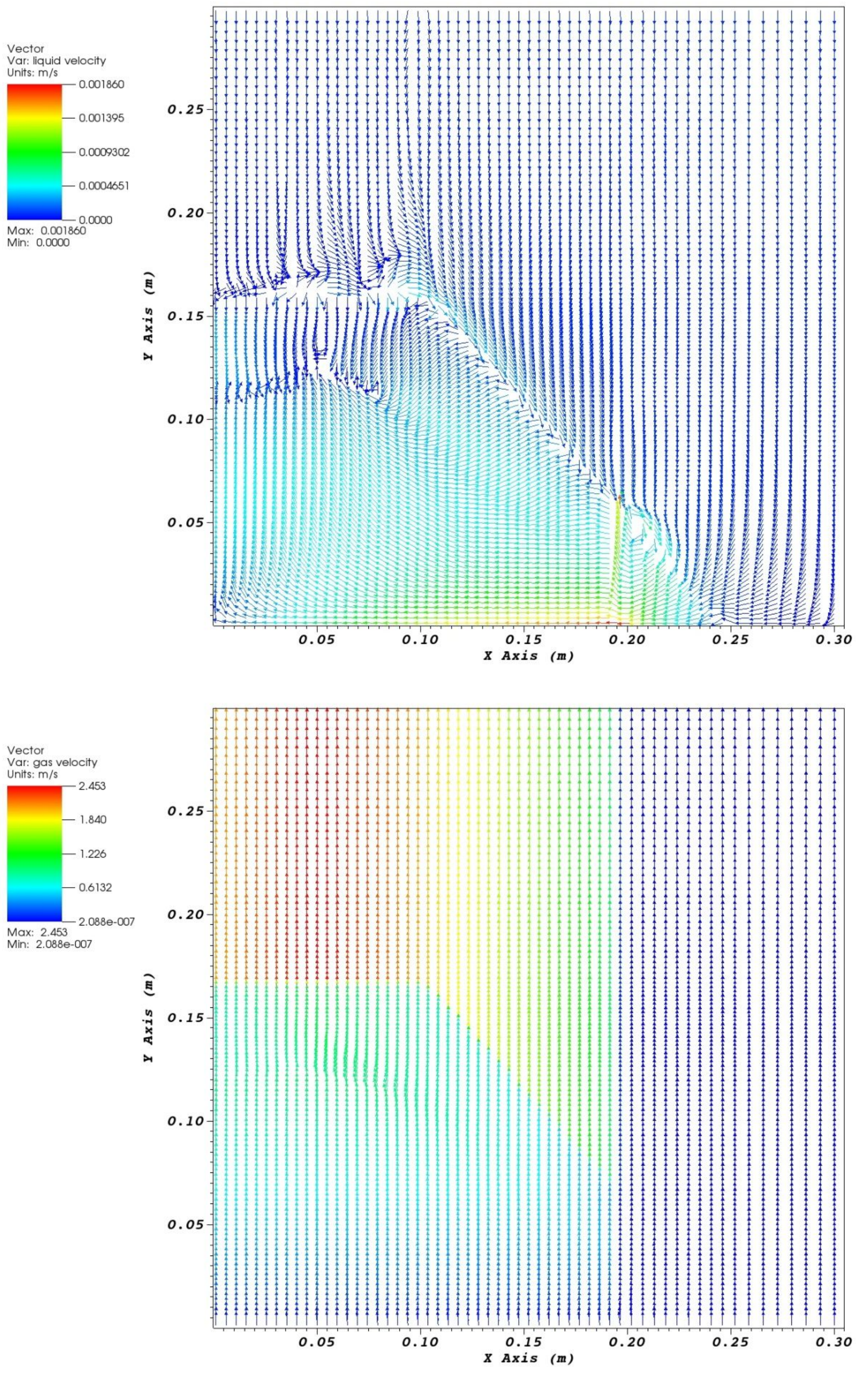

Figure 44. Pore velocity vectors for the liquid (top) and gas phase (bottom) in dryout conditions (quasi-steady state), 38 kW power, calculated for a partially heated bed with the MTD model.

5.2 CFD simulations

The computational 2D mesh used in the CFD simulations is shown in Figure 45. The mesh is fitted to the shapes of the truncated cone and the assumed heated area. The details of the experimental arrangements shown in Figure 3 were simplified and taken into account in the mesh. The cell size is about 3.5 mm.

The CFD simulations were carried out with the Fluent code (version 14). The 2nd order (unstructured) discretization schemes were used in space and time with some exceptions discussed below. In most of the CFD simulations, the pool was modelled as in the MEWA code. A simulation was performed in which the pool area was modelled as an open free-flow zone.

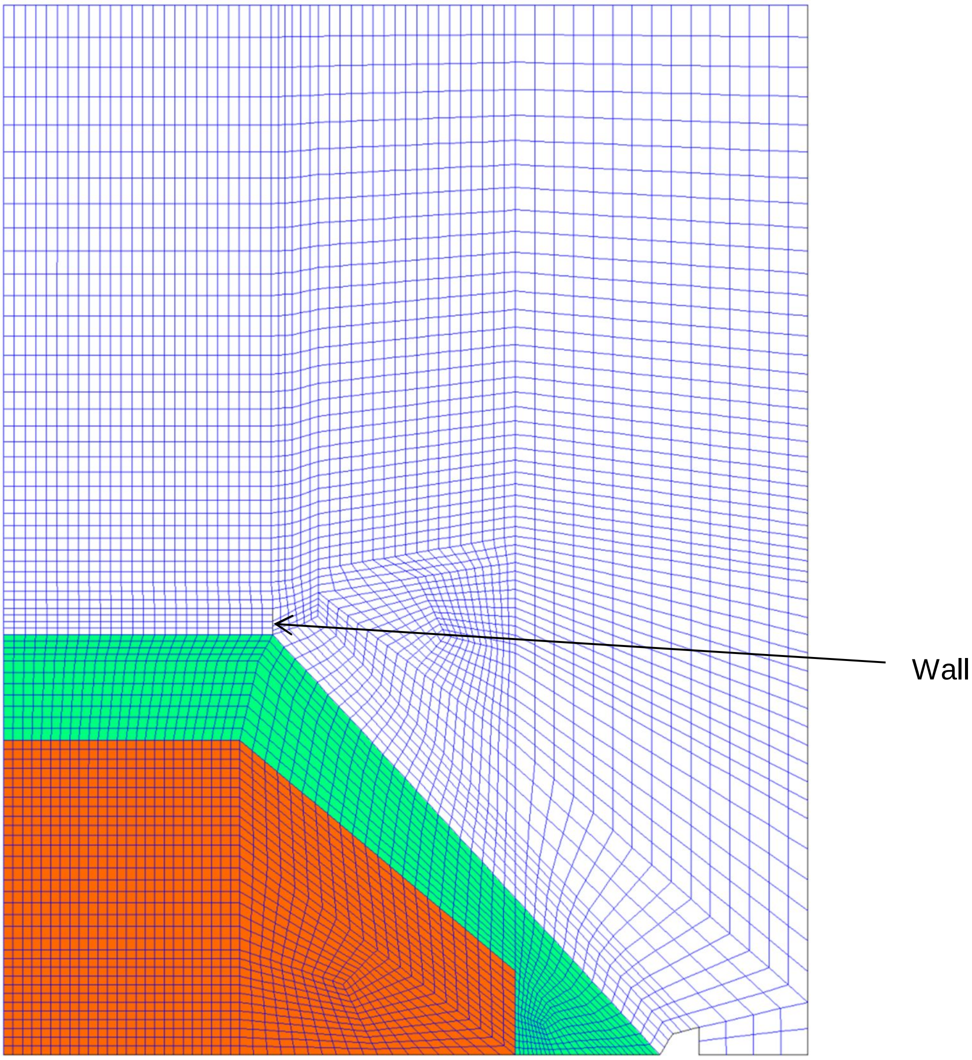

Figure 45. Computational mesh with representations of the heated part (red area) and unheated part (green area) of the bed in the CFD simulations for a partially heated bed. The 10 mm high wall above the bed represents the metallic band (cf.Figure 3).

5.2.1 Water pool as a high-porosity porous zone

In the following results, the pool outside of the truncated conical bed is modelled following closely the same method as the one in the MEWA code. In MEWA there are no separate models for the free flow in the pool. Instead, the pool is treated as a high-permeability porous medium. The drag force coefficients for the pool zone are calculated from the same models as for the debris bed zone by assuming that porosity is 90% and particle size is 0.01 m.

The CFD results depend on the time step, and time steps of 1, 10 and 100 ms were used. In multiphase CFD simulations, the Courant number should be less than 1 to ensure convergence. This would mean a time step less than 1 ms. However, the artificial friction forces in the MEWA2014 type pool stabilize computations and thus stable solutions are obtained for significantly larger time steps. However, in all other cases except in the simulations for the MTD model and 100 ms time step, results vary with time. Figure 46 and Figure 47 show the instantaneous void fraction, particle temperature and pore velocities for the Reed model and 1 ms time step in dryout conditions obtained with the 42 kW power. For the bed region the results do not vary significantly with time. On the other hand, in the pool area, the computational result is a consequence of the unrealistic MEWA pool model and should not be considered a CFD representation of a bubble flow in a free-flow pool.

Since instantaneous values are not that interesting and steady-state results are obtained with the MEWA code, time-averaged CFD results were also reproduced. Figure 49 and Figure 50 show the time-averaged void fraction, particle temperature and pore velocities for the same case as the instantaneous results are presented in Figure 46 and Figure 47. Figure 48 shows the void fraction for a corresponding case with a one step lower power (40 kW).

The time-averaged CFD results differ from the MEWA results in Figure 39 – Figure 41. First, dryout is obtained with a significantly higher power (more than 40 kW vs. less than 36 kW with MEWA). In fact, the dryout power obtained from the CFD results vary with the time step. The dryout powers deduced from the MEWA and Fluent simulations are plotted in Figure 51. As the power step was 2 kW, the dryout power could be any value between the powers with and without dryout. Figure 51 shows the most likely dryout power estimated based on the simulation results (on the basis of the dry area and particle temperature). The “error” bars represent the range of the actual computational dryout power. The CFD results of the time-averaged void fraction and particle temperature in dryout conditions (38 kW) are shown in Figure 52 for the time step of 10 ms (in Mewa simulations the time step was typically from 10 to 20 ms). The agreement with the MEWA result (Figure 40) is significantly improved.

The influence of discretization schemes in space and time were examined. In a set of test simulations, for all the other quantities except the momentum, the first order discretization scheme was used. Since Fluent employs unstructured spatial discretization methods, the first order spatial discretization should not be used for the momentum. Figure 53 shows the time-averaged void fraction and particle temperature in the dryout conditions (34 kW) for the time step of 10 ms and for the Reed model as above. Now the void fraction distribution in the pool area is reasonably similar to the MEWA result in Figure 40. Yet the heating power is 2 kW lower and a dry horizontal zone is obtained close to the bed surface. These differences are likely caused by the unstructured 1st order spatial discretization method (Fluent) which is considered less accurate than the structured 1st order spatial discretization scheme (MEWA).

To summarize the comparison of the MEWA and CFD results, we can conclude that the differences arise from different spatial discretization methods and different time steps.

The time–averaged CFD results for the MTD model are shown Figure 54 - Figure 56 with the 1 ms time step for the power step with dryout (40 kW) and for the previous power step (38 kW). The differences with the Reed model results (Figure 48- Figure 50) are not large, but the computational dryout power is estimated to be about 1 kW smaller with the MTD model.

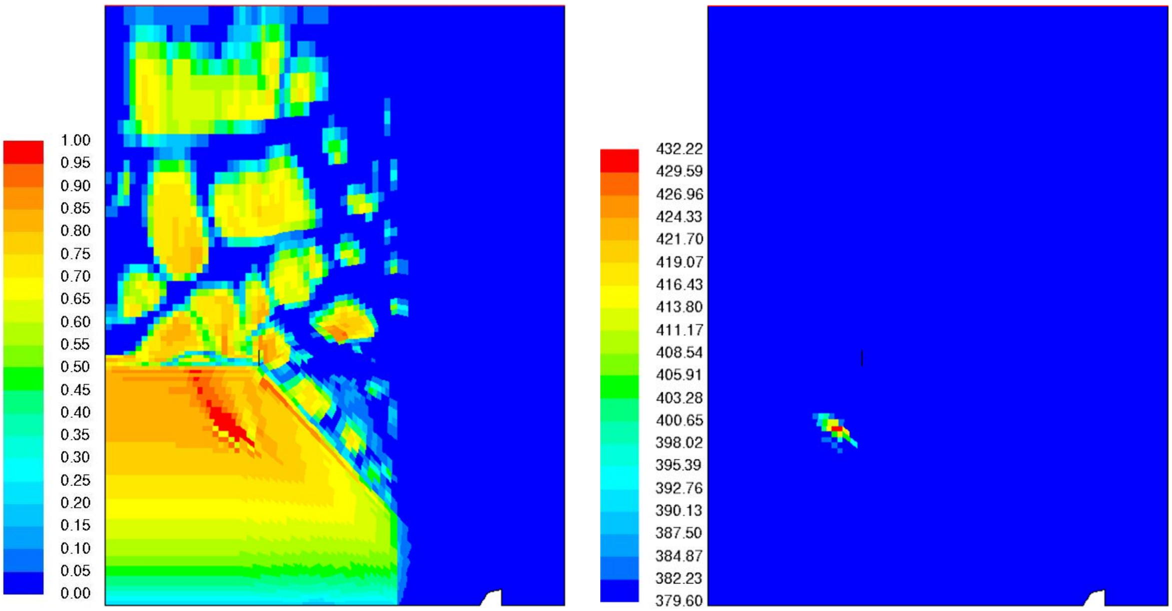

Figure 46. Instantaneous void fraction distribution (left) and particle temperature (right) for a partially heated bed in dryout conditions (quasi-steady state), 42 kW power, computed with Fluent using the 2nd order discretization and a 1 ms time step and applying the Reed model. The pool is modelled as in the MEWA2014 code.

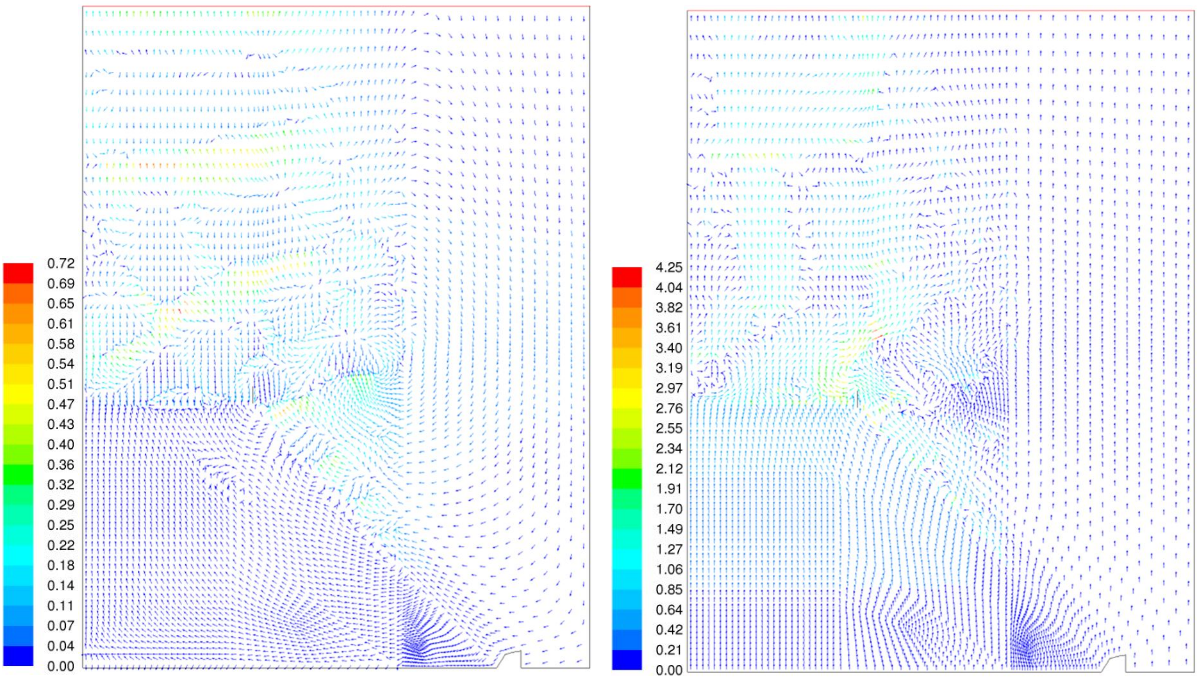

Figure 47. Instantaneous pore velocity vectors for the liquid (left) and gas phase (right) for a partially heated bed in dryout conditions, 42 kW power, computed with Fluent using the 2nd order discretization and a 1 ms time step and applying the Reed model. The pool is modelled as in the MEWA2014 code.

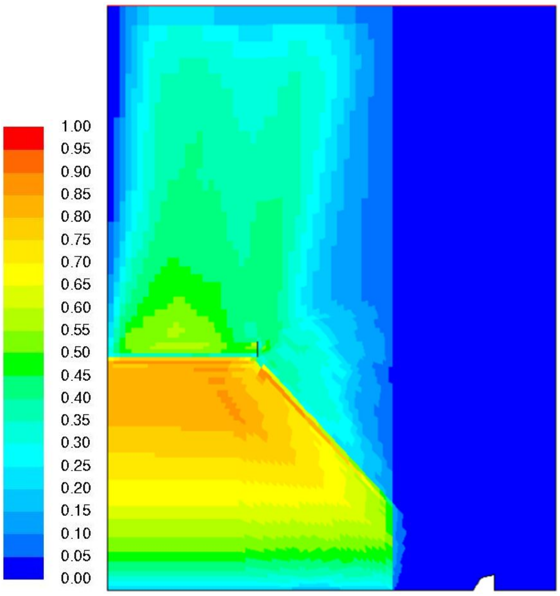

Figure 48. Time-averaged void fraction distribution for a partially heated bed in steady state, 40 kW power, computed with Fluent using the 2nd order discretization and a 1 ms time step and applying the Reed model. The pool is modelled as in the MEWA2014 code.

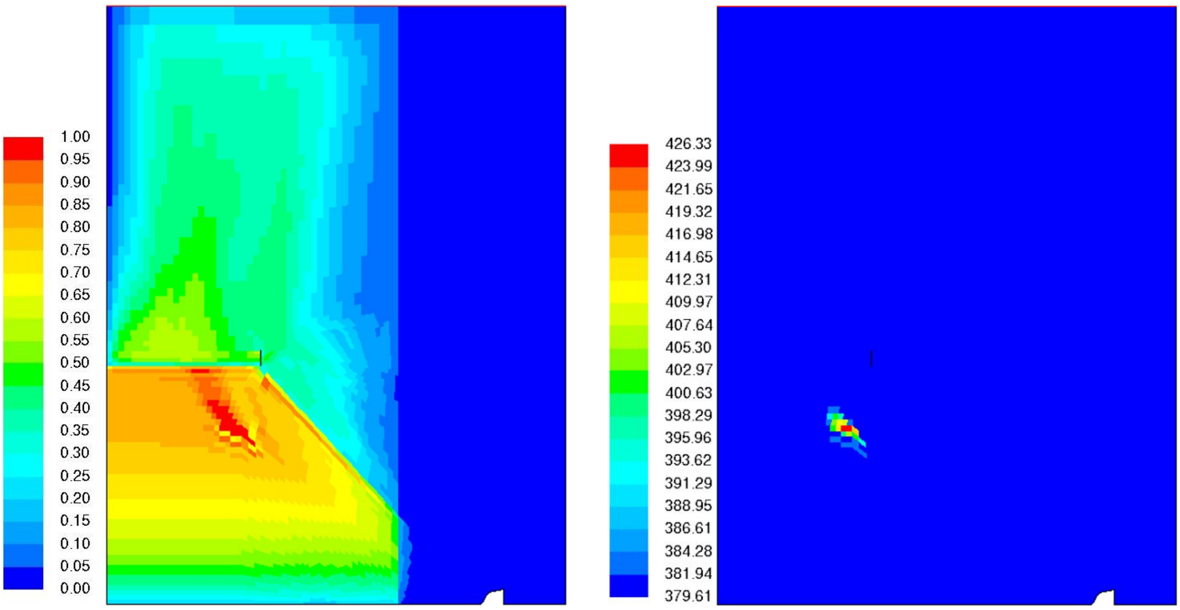

Figure 49. Time-averaged void fraction distribution (left) and particle temperature (right) for a partially heated bed in dryout conditions (quasi-steady state), 42 kW power, computed with Fluent using the 2nd order discretization and a 1 ms time step and applying the Reed model. The pool is modelled as in the MEWA2014 code.

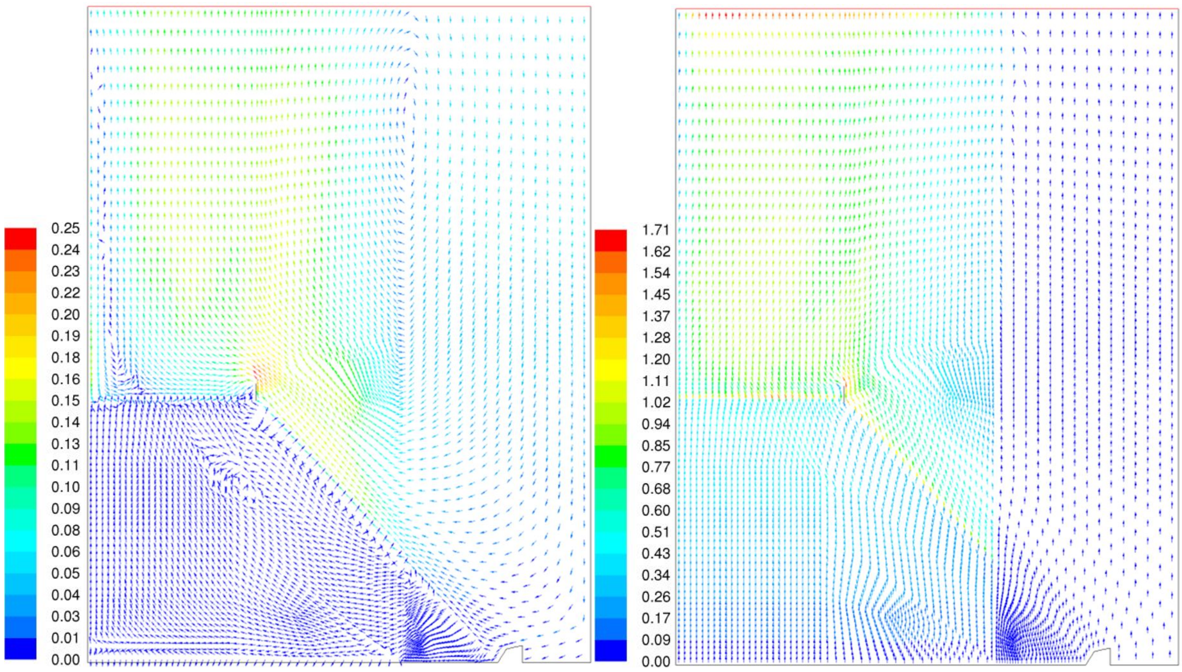

Figure 50. Time-averaged pore velocity vectors for the liquid (left) and gas phase (right) for a partially heated bed in dryout conditions, 42 kW power, computed with Fluent using the 2nd order discretization and a 1 ms time step and applying the Reed model. The pool is modelled as in the MEWA2014 code.

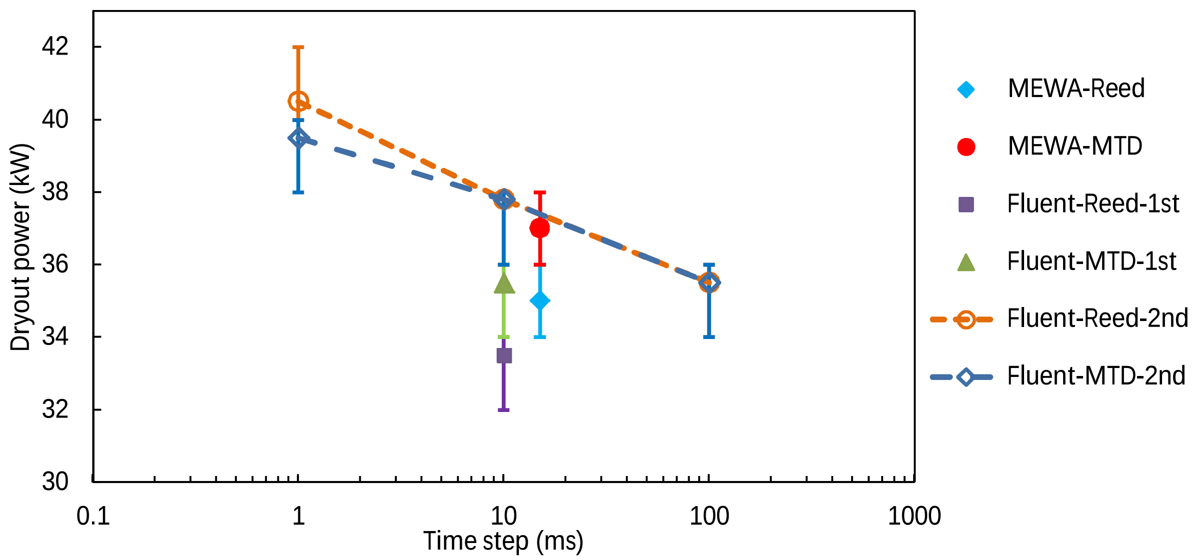

Figure 51. Dryout power for a partially heated bed as a function of the time step in the MEWA2014 and Fluent simulations for the Reed and MTD models and 1st and 2nd order discretizations. The pool is modelled as in the MEWA2014 code.

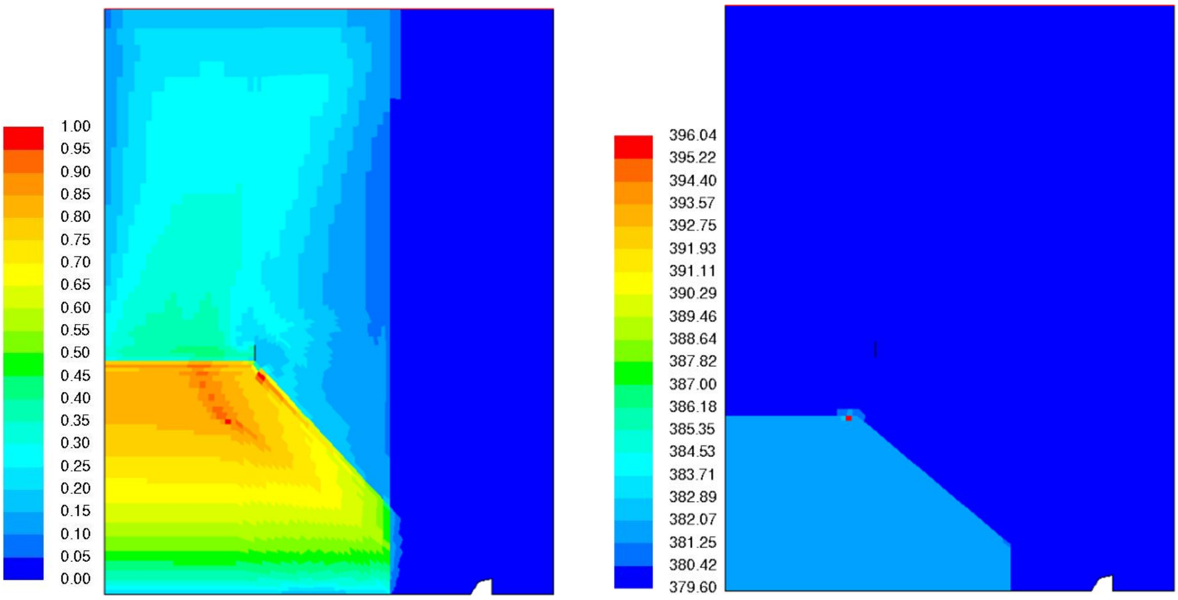

Figure 52. Time-averaged void fraction distribution (left) and particle temperature (right) for a partially heated bed in dryout conditions (quasi-steady state), 38 kW power, computed with Fluent using the 2nd order discretization and a 10 ms time step and applying the Reed model. The pool is modelled as in the MEWA2014 code.

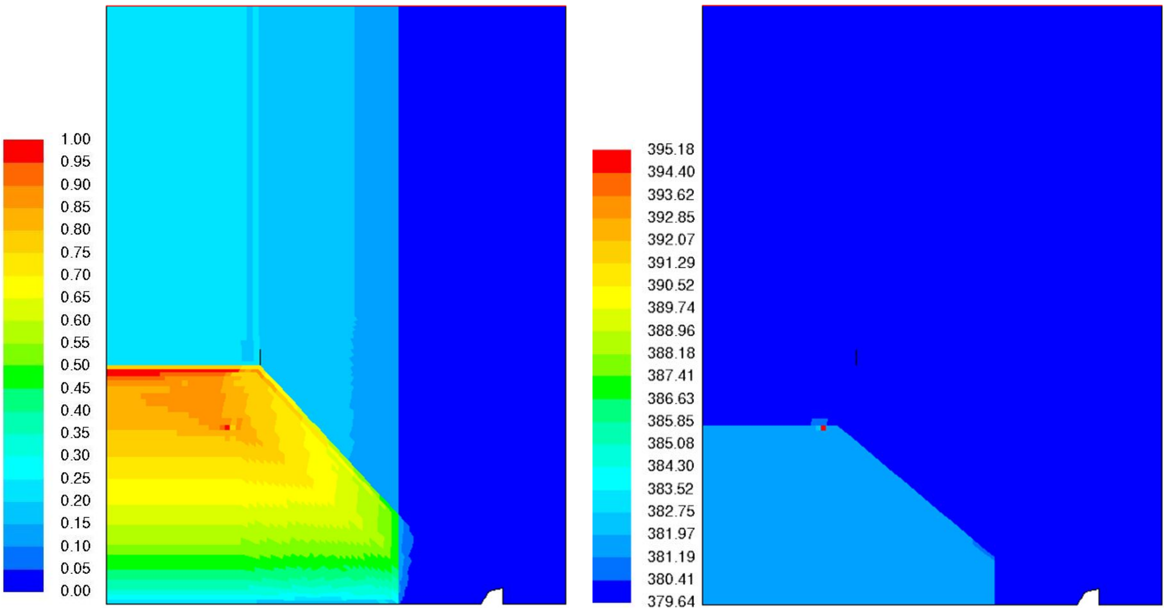

Figure 53. Time-averaged void fraction distribution (left) and particle temperature (right) for a partially heated bed in dryout conditions (quasi-steady state), 34 kW power, computed with Fluent using the 1st order discretization except the 2nd order discretization for the momentum and a 10 ms time step and applying the Reed model. The pool is modelled as in the MEWA2014 code.

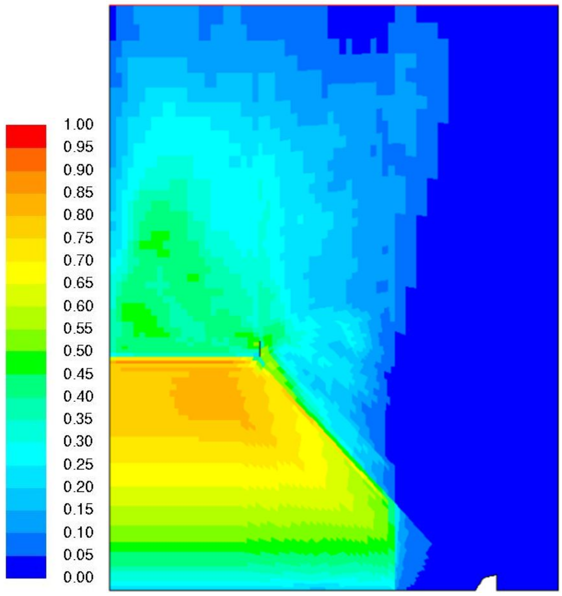

Figure 54. Time-averaged void fraction distribution for a partially heated bed in steady state, 38 kW power, computed with Fluent using the 2nd order discretization and a 1 ms time step and applying the MTD model. The pool is modelled as in the MEWA2014 code.

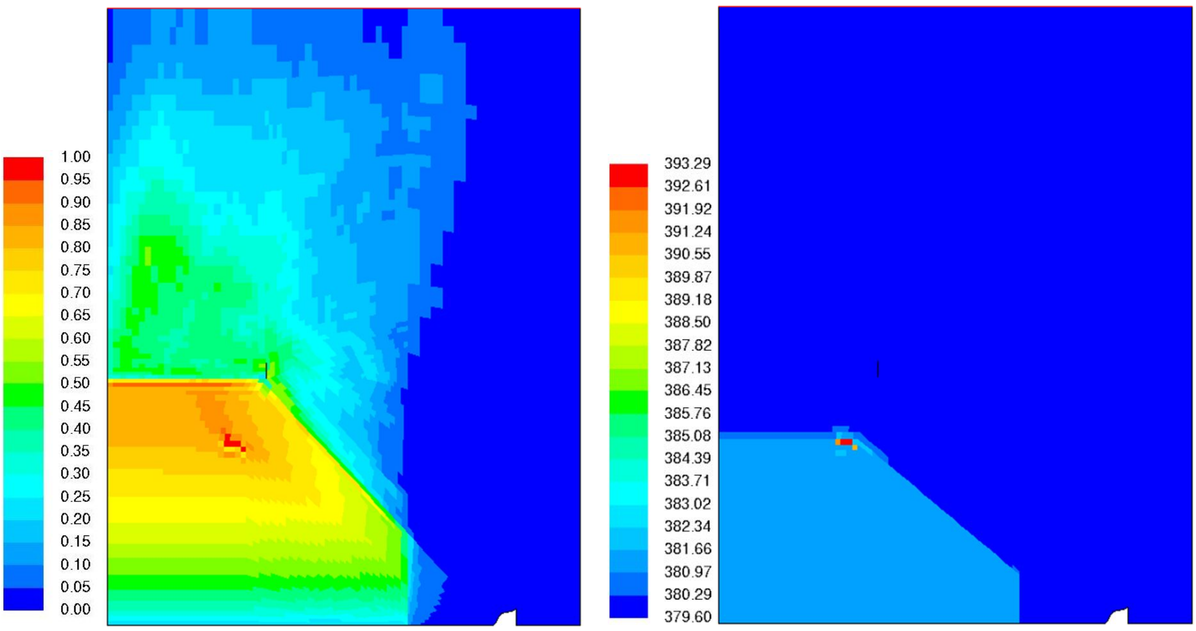

Figure 55. Time-averaged void fraction distribution (left) and particle temperature (right) for a partially heated bed in dryout conditions, 40 kW power, computed with Fluent using the 2nd order discretization and a 1 ms time step and applying the MTD model. The pool is modelled as in the MEWA2014 code.

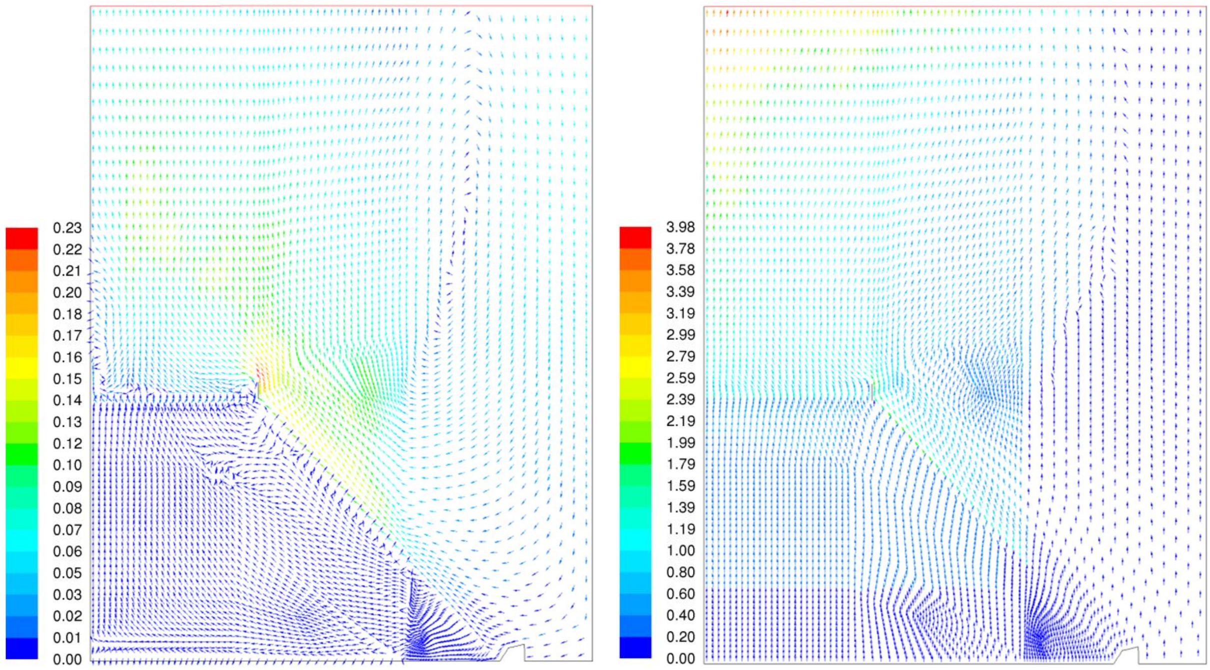

Figure 56. Time-averaged pore velocity vectors for the liquid (left) and gas phase (right) for a partially heated bed in dryout conditions, 40 kW power, computed with Fluent using the 2nd order discretization and a 1 ms time step and applying the MTD model. The pool is modelled as in the MEWA2014 code.

5.2.2 Water pool as a free-flow zone

A simulation was performed in which the open water pool outside the bed was modelled more realistically as a free-flow zone. For the pool zone, the MEWA models are replaced by the model of Schiller and Naumann [28] used for the interfacial drag force. In addition, the k-ϵ mixture turbulence model was employed for the pool area. The particle bed was modelled as a laminar zone. The 2nd order discretization schemes in space and time were applied.

The time step varies from 0.5 to 1 ms. Simulations did not converge with longer time steps. Compared to the MEWA-pool simulations, the stabilising influence of a friction in the pool area is missing and the Courant number needs to be less than 1 as in multiphase simulations in general. Moreover, in the free-flow zone, the liquid and gas velocities are larger, and consequently even the shortest time step of 1 ms applied in the corresponding MEWA-pool simulations is somewhat too long causing divergences once a while.

The computation was performed for the heating power of 40 kW with the MTD model. Figure 57 and Figure 58 show the time-averaged void fraction and velocities for the time step of 0.5 ms (the 1 ms results are qualitatively similar). Compared to the MEWA pool simulation result (Figure 55 and Figure 56), the void fraction in the water pool differs significantly. On the other hand, the pool modelling method does not affect remarkably the bed area results. However, contrary to the MEWA-pool result (Figure 55), no dryout is obtained (applies also the 1 ms simulation). In the free-flow pool simulation, the velocities close to the inclined bed surface are larger increasing the velocities also in the bed and resulting in improved cooling. More importantly, the injector phenomenon intensifies flow in the particle bed: the flow outside the bed causes a pressure minimum above the bed close to the top edge (can also be recognized from the high void fraction in Figure 57). Furthermore, the suction from the bed leads to downwards flows at the bed surface next to the axis.

Considering the evaluation of the dryout power, the water-pool modelling method seems to have some influence. The injector phenomena increases flow rates especially in the top part of the particle bed. However, the influence is comparable with the effects of the friction models and smaller than the influences of the time step and spatial discretization.

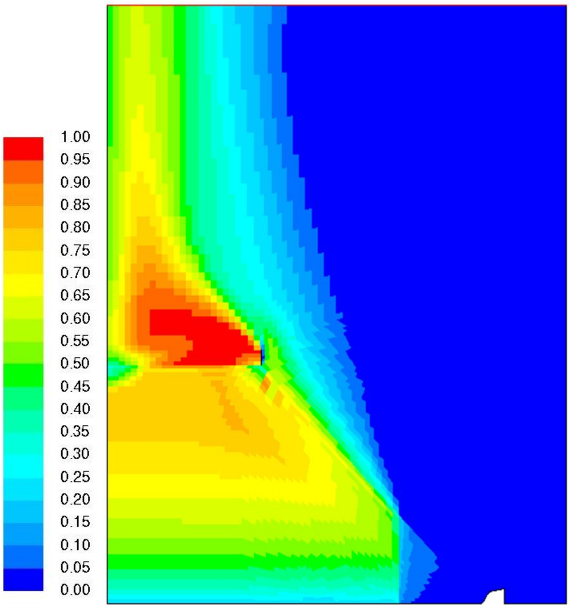

Figure 57. Time-averaged void fraction distribution for a partially heated bed in steady state, 40 kW power, computed with Fluent using the 2nd order discretization and a 0.5 ms time step and applying the MTD model. The pool is modelled realistically as a free-flow zone.

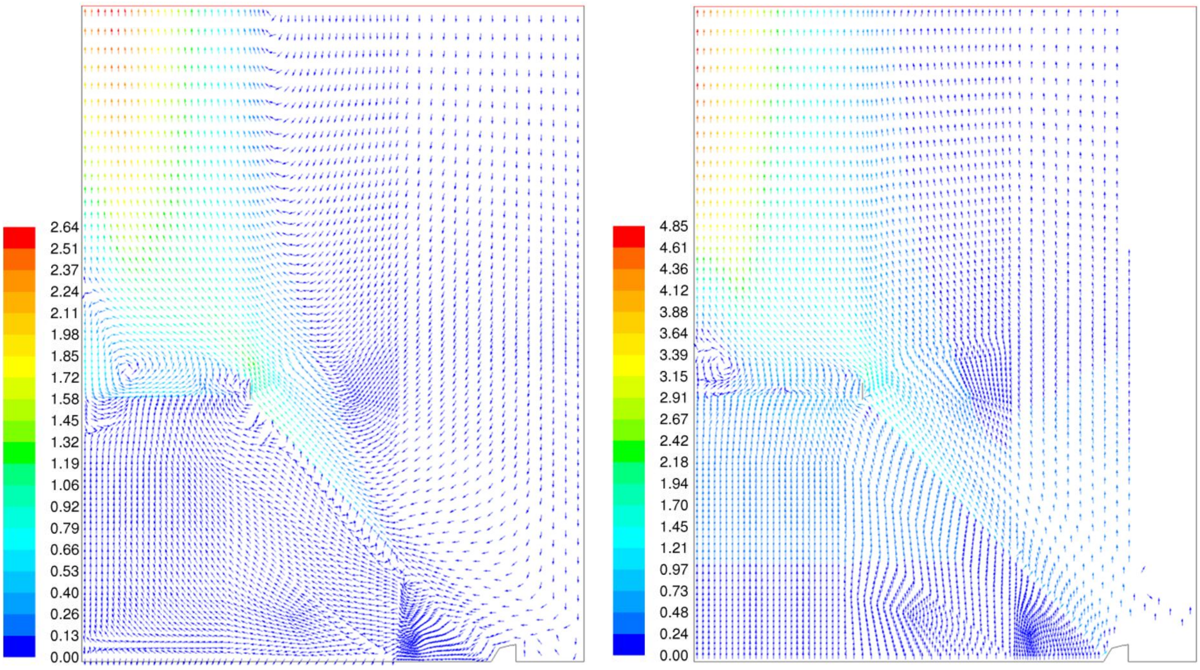

Figure 58. Time-averaged pore velocity vectors for the liquid (left) and gas phase (right) for a partially heated bed in steady state, 40 kW power, computed with Fluent using the 2nd order discretization and a 0.5 ms time step and applying the MTD model. The pool is modelled realistically as a free-flow zone.

5.3 Summary of the truncated cone simulations

The truncated cone geometry was modelled with the MEWA and Fluent codes, and two alternative approaches for the modelling of the test bed heating were tested. Dryout at slightly higher powers than in the experiments were obtained for the bed with homogenous heating in the full test bed (maximum difference 20%). For a more localized heating, which can be considered a more accurate representation of the COOLOCE test bed (without taking into account the details of the heaters, however), lower dryout power was obtained. This power is very close to the experimental power. On the other hand, there are several other factors that influence the dryout power predicted by the codes.

In the simulations, dryout is first seen in the part of the bed which is radially close to the corner of the flat and the inclined surfaces (for both full heating and partial heating). The steam is easily accumulated into this part because of the liquid vortex formed at the corner. In the experiments this was not the case: dryout was indicated by the central censors and not by the sensors below the junction of the flat and the inclined part. However, it should be kept in mind that the model does not account for the internal non-homogeneity of the test bed in detail (heaters, sensors and random packing of the particles) and it cannot be expected that the bed test bed would behave exactly as the ideal modelled bed. Moreover, in reality, and as indicated by the free-flow fool simulations, a local pressure minimum is developed above the bed close to the edge that enhances the suction of water and gas from the bed and thus improves cooling.

The friction force model has an effect on the dryout power in all the simulations as expected: The Reed model yields lower dryout power than the MTD model. According to the validation calculations with a simple flow-through test and the fully conical and cylindrical test beds, the MTD model in MEWA2014 yields somewhat greater dryout power than the MTD model implementation in MEWA2008.

The Fluent simulations show that the time step, discretization scheme and the pool model have an effect on the results. The predicted void fraction and velocity fields vary depending on these choices, especially in the pool zone. The effect of the numerical parameters and the pool model on the predicted dryout power (for which the accuracy of 1-2 kW is adequate) is small but noticeable (see Figure 51).

6. Conclusions

The coolability of a heap-shaped debris bed (truncated cone) has been investigated experimentally and analytically with the COOLOCE test facility and with 2D simulation models. The dryout power for this type of geometry was measured in the COOLOCE-13 and COOLOCE-13R test runs. Comparison of the measured dryout powers and the heat fluxes at the top boundary in the test beds with different geometries and flooding modes revealed that the coolability of the truncated cone is comparatively high, about the same as that of the fully conical bed and the fully flooded cylinder with open sidewall.

The truncated cone geometry was modelled with the MEWA and Fluent codes, and two alternative approaches for the modelling of the test bed heating were tested. Dryout at slightly higher powers than in the experiments were obtained for the bed with homogenous heating in the full test bed. For a more localized heating, lower dryout power was obtained. This power is very close to the experimental power. On the other hand, there are several other factors that influence the dryout power predicted by the codes.

Using the Fluent model, a study on the effect of the numerical solver options was done. The Fluent simulations show that the time step, discretization scheme and the pool model have an effect on the results. The predicted void fraction and velocity fields vary depending on these choices, especially in the pool zone. The effect of the numerical parameters and the pool model on the predicted dryout power (for which the accuracy of 1-2 kW is adequate) is small but noticeable.

During this work, a new version of the MEWA code was taken into use. Prior to the application of the code to the modelling of the truncated cone experiment, the new version was tested with a simple flow-though test and with the models of the cylindrical and fully conical test beds. It was found that the modified Tung and Dhir model in the version of 2014 yields somewhat greater dryout power than the corresponding model in the previous version in use at VTT. Otherwise, the results obtained with the new and old code versions are very similar.

References

1. Takasuo, E., Holmström, S., Kinnunen, T., Pankakoski, P.H. 2012. The COOLOCE experiments investigating the dryout power in debris beds of heap-like and cylindrical geometries. Nuclear Engineering and Design, 250, pp. 687-700.

2. Takasuo, E., Kinnunen, T., Pankakoski, P.H., Holmström, S. 2011 The COOLOCE particle bed coolability experiments with a conical geometry: Test series 6-7. Research Report VTT-R-07097-11. 26 p.

3. Takasuo, E., Kinnunen, T., Holmström, S. 2012. COOLOCE particle bed coolability experiments with a cylindrical test bed: Test series 8-9. Research report VTT-R-07224-12. 44 p.

4. Takasuo, E., Kinnunen, T., Holmström, S, Lehtikuusi, T. 2013. COOLOCE coolability experiments with a cylindrical debris bed and lateral flooding: COOLOCE-10. Research Report VTT-R-0463-13. 16 p.

5. Takasuo, E., Kinnunen, T., Holmström, S, Lehtikuusi, T. 2013. COOLOCE debris bed coolability experiments with an agglomerate simulant: Test series 11. Research Report VTT-R-03316-13. 22 p.

6. Takasuo, E., Kinnunen, T., Lehtikuusi, T. 2013. COOLOCE-12 debris bed coolability experiment: Cone on a cylindrical base. Research Report VTT-R-07967-13. 18 p.

7. Bürger, M., Buck, M., Schmidt, W., Widmann, W. 2006. Validation and application of the WABE code: Investigations of constitutive laws and 2D effects on debris coolability. Nuclear Engineering and Design 236 (2006), pp. 2164-2188.

8. Rahman, S. 2013. Coolability of Corium Debris under Severe Accident Conditions in Light Water Reactors. Doctoral thesis, Insitut für Kernenergetik und Energiesysteme, Universität Stuttgart, IKE 2-155. ISSN-0173-6892.

9. Takasuo, E., Taivassalo, V., Hovi, V. A study on the coolability of debris bed geometry variations using 2D and 3D models. Research Report VTT-R-00676-14. Espoo, 2014.

10. Takasuo, E., Hovi, V., Ilvonen, M., Holmström, S. Modeling of Dryout in Core Debris Beds of Conical and Cylindrical Geometries. 2012. 20th International Conference on Nuclear Engineering collocated with the ASME 2012 Power Conference. July 30 – August 3, 2012, Anaheim, California, USA. ICONE20-POWER2012-54159.

11. Takasuo, E., Holmström, S., Kinnunen, T., Pankakoski, P.H., Hovi, V., Ilvonen, M., Rahman, S., Bürger, M., Buck, M., Pohlner, G. Experimental and Computational Studies of the Coolability of Heap-like and Cylindrical Debris Beds. 5th European Review Meeting on Severe Accident Research (ERMSAR-2012), Cologne, Germany, March 21-23, 2012.

12. Ergun, S. 1952. Fluid flow through packed columns. Chemical Engineering Progress 48, pp. 89-94.

13. Takasuo, E., Hovi, V., Ilvonen, M. Applications and Development of the PORFLO 3D Code in Nuclear Power Plant Thermal Hydraulics. 20th International Conference on Nuclear Engineering , Anaheim, California, USA, July 30 – August 3, 2012 (ICONE20-54161).

14. Fluent. 2011. ANSYS FLUENT Theory Guide, Release 14.0, Southpointe, ANSYS, Inc.

15. Fluent. 2011. ANSYS FLUENT User's Guide, Release 14.0, Southpointe, ANSYS, Inc.

16. Imura, S., Takegoshi, E. 1974. Effect of Gas Pressure on the Effective Thermal Conductivity of Pack Beds. Heat Transfer Japanese Research, Vol. 3, No. 4, 13 p.

17. Vortmeyer, D. 1978. Radiation in Packed Solids. 6th International Heat Transfer Conference, Toronto, Canada, 1978.

18. Lipinski, R.J., 1982. A Model for Boiling and Dryout in Particle Beds. US Nuclear Regulatory Committee, NUREG/CR-2646, SAND82-0765.

19. Reed, A.W. 1982. The effect of channeling on the dryout of heated particulate beds immersed in a liquid pool. Doctoral Thesis, Department of Mechanical Engineering, Massachusetts Institute of Technology, 1982.

20. Lipinski, R.J. 1984. A coolability model for postaccident nuclear reactor debris. Nuclear Technology, 65, pp. 53-66

21. Hu, K., Theofanous, T.G. 1991. On the measurement and mechanism of dryout in volumetrically heated coarse particle beds. International Journal of Multiphase Flow, 17 (No. 4).

22. Schulenberg, T., Müller, U. 1986. A refined model for the coolability of core debris with flow entry from the bottom. Proceedings of the Sixth Information Exchange Meeting on Debris Coolability. EPRI NP-4455. Los Angeles, March 1986.

23. Tung, V.X. and Dhir, V.K., 1988. A Hydrodynamic Model for Two-Phase Flow through Porous Media. International Journal of Multiphase Flow, 14, No. 1, pp. 47-65.

24. Schmidt, W. 2004. Influence of Multidimensionality and Interfacial Friction on the Coolability of Fragmented Corium. Doctoral Thesis. Institut für Kernenergetik und Energisysteme. IKE 2-149. ISSN-0173-6892.

25. Rohsenow, W. 1952. A method of correlating heat transfer data for surface boiling of liquids. Trans. ASME, 74, pp. 969–976.

26. Lienhard, J.H. 2012. A Heat Transfer Textbook, 4th edition. Phlogiston Press, Cambridge, Massachusetts, USA.

27. Ranz, W.E., Marshall, W. R. 1952. Evaporation from drops. Chemical Engineering Progress, 48, pp. 141-146.

28. Schiller, L., Naumann, Z.Z. 1935. A drag coefficient correlation. Ver. Deutsch. Ing., 77, pp. 318-325.

29. Takasuo, E. 2013. Debris coolability simulations with different particle materials and comparisons to COOLOCE experiments. Research Report VTT-R-00257-13. 17 p.

30. Chikhi, N., Coindreau, O., Li, L.X. , Ma, W.M., Taivassalo, V., Takasuo, E., Leininger, S., Kulenovic, R., Laurien, E. 2013. Evaluation of an Effective Diameter to Study Quenching and Dry-out of Complex Debris Bed. 6th European Review Meeting on Severe Accident Research (ERMSAR-2013), Avignon, France, October 2-4, 2013.

Appendix A. COOLOCE-13 heater and thermocouple arrangement

Heater map

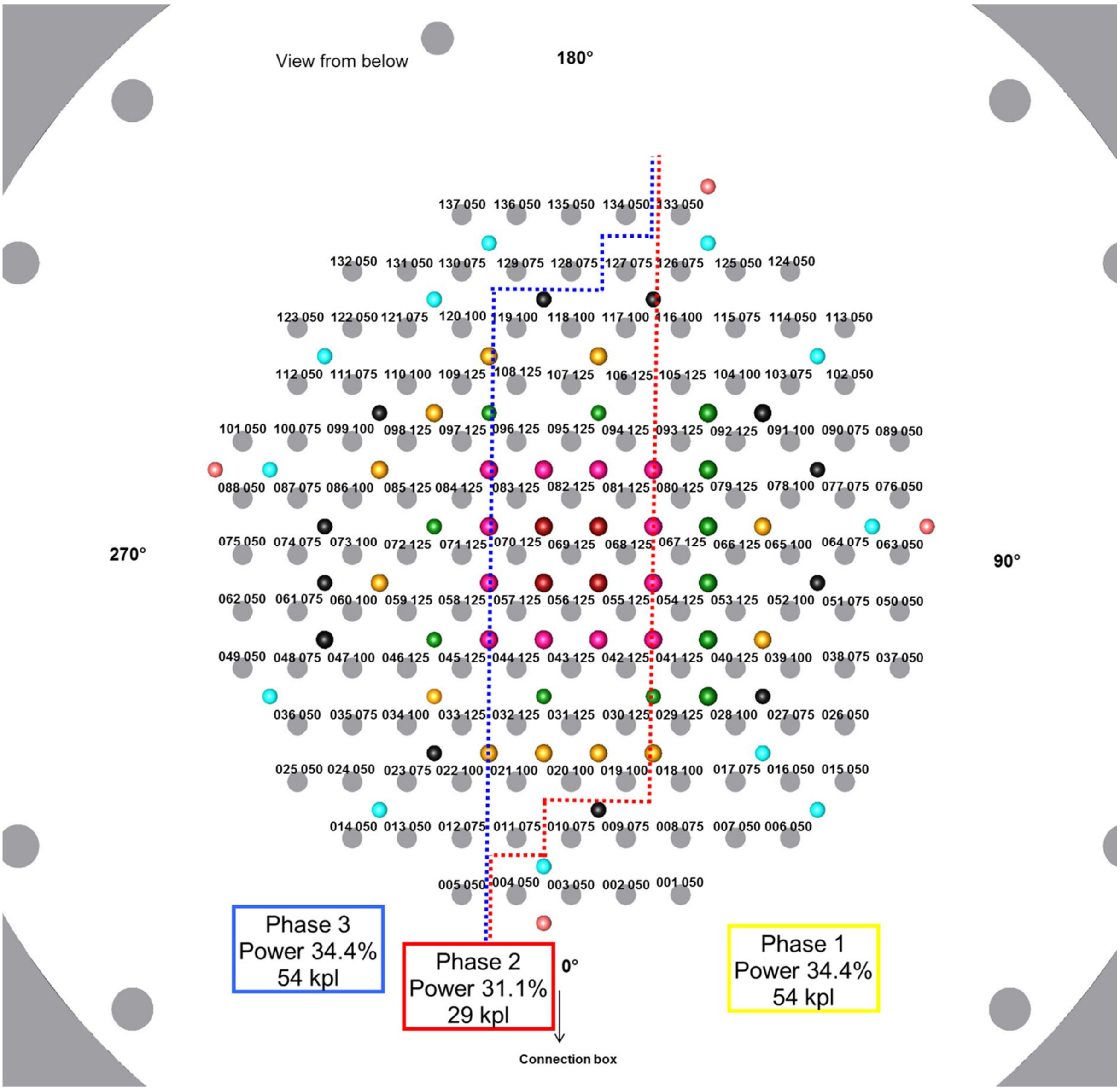

Temperature sensor map

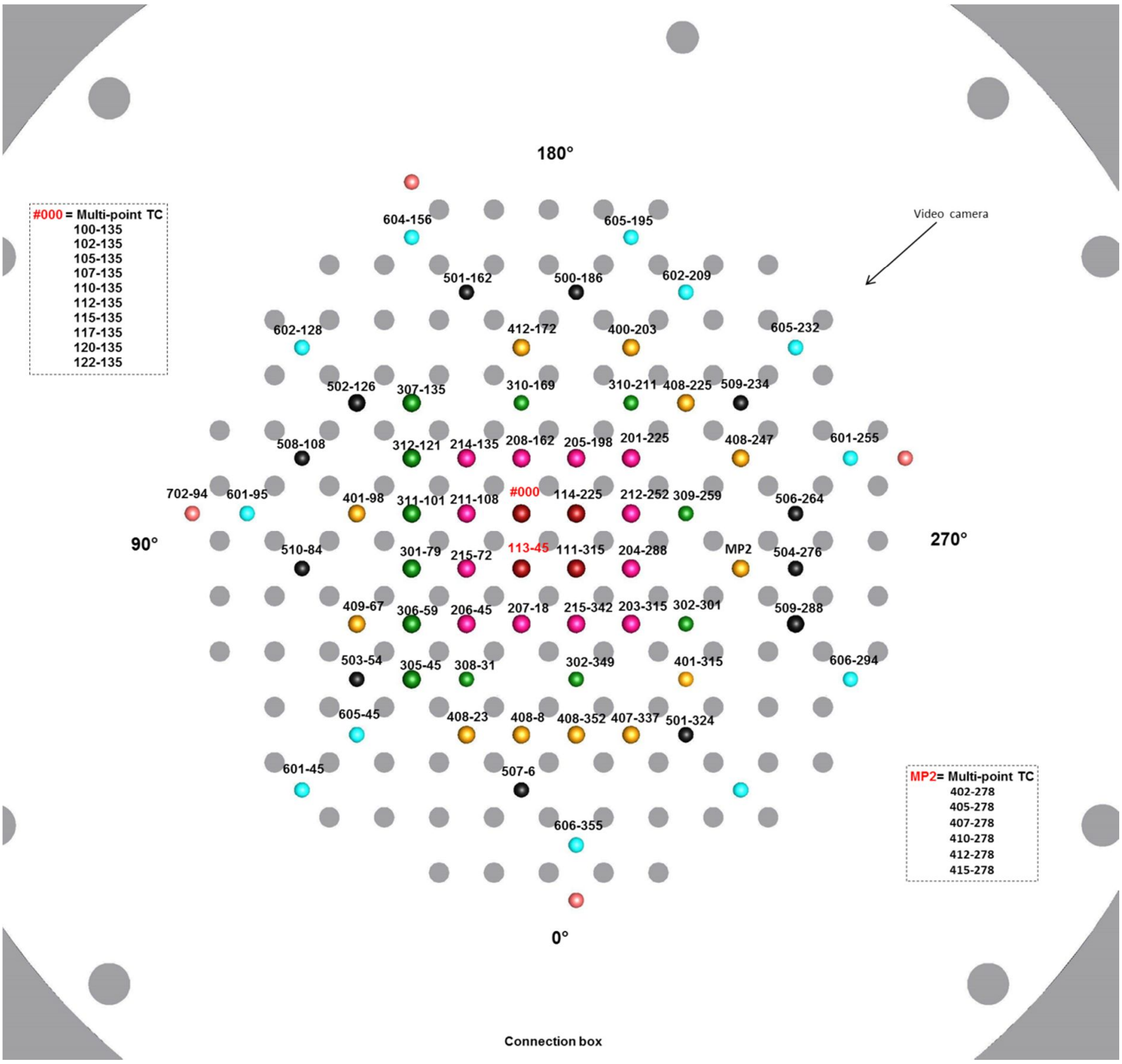

Example of how to read the map:

201-225
1 – number of the ring to which the thermocouple belongs to (1 indicates the central sensors, 6 the outermost)
11 – height of the thermocouple from the bottom in cm
225 – angle between the thermocouple location and 0°

Bibliographic Data Sheet **NKS-343**

Title	Coolability analyses of heap-shaped debris bed
Author(s)	Eveliina Takasuo, Veikko Taivassalo, Tuomo Kinnunen, Taru Lehtikuusi
Affiliation(s)	VTT Technical Research Centre of Finland
ISBN	978-87-7893-425-3
Date	July 2015
Project	NKS-R / DECOSE
No. of pages	55
No. of tables	0
No. of illustrations	58
No. of references	30
Abstract max. 2000 characters	This report describes the experimental and analytical debris bed coolability studies conducted during 2014 at VTT. The main focus is on the coolability of a heap-shaped debris bed (truncated cone) which has been examined by dryout power measurements with the COOLOCE facility and by two-phase flow simulations. The work is divided to three parts. In the first part, the coolability experiments with the truncated cone, COOLOCE-13 and -13R, are described. The second part presents the testing and validation calculations of the new 2014 version of the MEWA 2D code applied to assess debris coolability. The third part consists of the modelling of the truncated cone experiment by using the new MEWA version and the CFD code Fluent. The experimental results suggest that the heap-like shape of the debris bed is favourable to coolability. The dryout heat flux is comparable to that of the fully conical bed and the other test beds with multi-dimensional flooding. The dryout power predicted by MEWA is within 20% of the experimental results. The effects of the numerical solution options have been examined in the Fluent simulations.
Key words	severe accident, debris bed, coolability, multi-dimensional flooding, numerical simulation, CFD

Available on request from the NKS Secretariat, P.O.Box 49, DK-4000 Roskilde, Denmark.
Phone (+45) 4677 4045, fax (+45) 4677 4046, e-mail nks@nks.org, www.nks.org